MAGMATIC PROCESSES AT MID-OCEAN RIDGES: EVIDENCE FOR HIGH-PRESSURE CRYSTALLIZATION AND CRUSTAL ASSIMILATION

A DISSERTATION SUBMITTED TO THE GRADUATE DIVISION OF THE
UNIVERSITY OF HAWAI‘I IN PARTIAL FULFILLMENT OF THE
REQUIREMENTS FOR THE DEGREE OF

DOCTOR OF PHILOSOPHY

IN

GEOLOGY AND GEOPHYSICS

DECEMBER 2009

By
Deborah E. Eason

Dissertation Committee:

John Sinton, Chairperson
Robert Dunn
Julia Hammer
Garrett Ito
David Muenow

We certify that we have read this dissertation and that, in our opinion, it is satisfactory in scope and quality as a dissertation for the degree of Doctor of Philosophy in Geology and Geophysics.

DISSERTATION COMMITTEE

____
Chairperson

____

____

____

____

ACKNOWLEDGEMENTS

It is a pleasure to acknowledge some of the colleagues and friends who have contributed to this dissertation. First and foremost on this list is my advisor John Sinton, who has served in multiple capacities as mentor, colleague, and friend. This work would not have been possible without his patient guidance and infectious enthusiasm. I consider myself incredibly fortunate to have had this opportunity to learn from him and work alongside him.

I would also like to thank my committee members Robert Dunn, Julia Hammer, Garrett Ito and David Muenow for their guidance throughout this process. They have each contributed invaluable and unique insight to the scientific problems herein. Thank you for your patient teaching and good humor throughout this process. In addition to my committee, others in the Geology & Geophysics community have provided a wealth of intellectual guidance and assistance over the years. I would like to acknowledge most especially JoAnn Sinton, Eric Hellebrand, Kent Ross, and Chuck Fraley for their vital assistance with sample preparation and laboratory analyses.

The field portion of this work would not have been possible without the assistance of JoAnn Sinton and Melissa Rotella – thank you for your companionship and expert rock-carrying skills, a burden you shouldered with good humor. A very special thanks also goes to Karl Grönvold for his expert transportation services, field assistance and scientific insight, as well as to all those in Iceland who've supported our work there and welcomed us into their homes – kærar þakkir!

To the magma chamber denizens, past and present, and most especially my officemates, Nancy Adams, Eric Bergmanis, Carrie Brugger, Nicole Lautze, Melissa Rotella, and Wendy Stovall: thank you for always being there. You've fielded many a random question, suffered the occasional venting session, and provided much-needed distractions and entertainment over the years. You have served as colleagues, friends and therapists, and all the while you've kept me smiling.

I have many friends to thank for my current levels of sanity at the end of this particular road. A special thanks goes to Vivian Chau, Jennifer Chu, Mishty Deb, William Koeppen, Wes Price, Anna Smolentzov and Kyle Woerner for their seemingly infinite patience and moral support. I greatly value their friendship and deeply appreciate their belief in me. I am also grateful to my Honolulu dance ohana – I have been incredibly fortunate to find such a supportive group of good people and I thank them for their friendship, respect, and for providing me with a very necessary creative outlet.

Finally, many thanks are due to my family for their unwavering support. A special thank you to my parents, who have always allowed me the freedom to find my own path. I am deeply indebted to them for their trust, support and encouragement. I also have been fortunate enough to encounter many fabulous teachers along the way, whose kind mentoring gave me the courage to pursue anything and everything – my sincere gratitude to them for their inspiration, enthusiasm and patient guidance. A particularly heartfelt thank you goes to my high school physics teacher and advisor David Koch, who played a significant role in my decision to pursue a career in science.

Financial support of these research projects has been provided by the National Science Foundation. Thank you to all those who have read and contributed to versions of this document in part or in whole. Any remaining mistakes or misconceptions are entirely my own.

ABSTRACT

This dissertation examines magmatic processes along two mid-ocean ridge segments: the Galápagos Spreading Center (GSC) and the Western Volcanic Zone (WVZ) in Iceland. Observations from these study areas illustrate the importance of variable mantle melting, melt transport and storage conditions, and the potential role of crustal assimilation processes in creating geochemical variability in mid-ocean ridge basalts (MORB).

Some MORB from the GSC exhibit higher Al contents (>16.0 wt. % Al_2O_3 at >8.5 wt. % MgO) than expected for normal MORB evolution. Thermodynamic modeling of glass and mineral chemistry shows that high-pressure (0.3-0.4 GPa) crystallization can account for the unusually high Al and low Si contents of these glasses. These samples are similar to moderately rare high-Al MORB from other slow and intermediate spreading ridges and close to fracture zones elsewhere, suggesting that crystal fractionation in the upper mantle is an important process at these settings.

In Iceland's WVZ, two eruptive units – one lava shield (Lambahraun) and one fissure eruption (Thjófahraun) – were erupted ~4000 yrs B.P. with eruptive centers separated by only ~25 km. Thjófahraun, which erupted ~1 km^3 of pāhoehoe and ‘a‘ā lava from a 9-km long fissure, exhibits geochemical variations consistent with evolution by low-pressure fractionation and eruption from a shallow magma chamber. In contrast, Lambahraun erupted >7 km^3 of low effusion-rate pāhoehoe, shows evidence of plagioclase accumulation in select samples, and exhibits enrichments in CaO and highly incompatible trace elements that increase with increasing magmatic differentiation.

Geochemical modeling of Lambahraun's major and trace element variations indicates the observed correlations between incompatible element concentration, increasing differentiation and time during the eruption can be related by concurrent wallrock assimilation and crystallization during melt migration (MAFC) through the crust.

We explore the conditions under which this melt-wallrock interaction plays a role in the formation of MORB using a 2-d numerical model of heat exchange between a magma conduit and its surrounding wallrock. Erupted crystal fractions and anatectic melt proportions are dependent on conduit geometry and magma ascent rate, with long-lived, low-effusion eruptions resulting in sufficient wallrock partial melting to produce observable geochemical effects in erupted basalts.

TABLE OF CONTENTS

Chapter 1: Introduction

Chapter 2: Origin of high-Al N-MORB by fractional crystallization in the upper mantle beneath the Galápagos Spreading Center

Chapter 3: Lava shields and fissure eruptions of the Western Volcanic Zone, Iceland: evidence for magma chambers and crustal interaction

Chapter 4: Thermal model of fractional crystallization and crustal assimilation during magma migration

Chapter 5: Conclusions

LIST OF TABLES

LIST OF FIGURES

Figure **Page**

CHAPTER 1

INTRODUCTION

1.1 Overview

Mid-ocean ridges exhibit geochemical variations at a variety of scales, from long wavelength variations spanning many kilometers of the ridge axis, to changes in melting or differentiation processes within a single eruption. Such variations are useful for investigating the underlying magmatic processes involved. This dissertation examines magmatic processes at two different mid-ocean ridge segments: a ~300-km section of the intermediate-spreading Galápagos Spreading Center, and the slow-spreading Western Volcanic Zone, an approximately 170-km long subaerial portion of the Mid-Atlantic Ridge in Iceland. These two field areas provide very different sampling conditions and therefore very different data coverage, presenting opportunities to study a range of processes including source melting and differentiation conditions, variations in eruptive style, and melt modification processes.

Chapter 2 of the dissertation examines chemical variations along a portion of the Galápagos Spreading Center (GSC). Some mid-ocean ridge basalt (MORB) glass samples from this region have very high Al contents (> 16.0 wt. % Al_2O_3 at > 8.5 wt. % MgO), similar to high-Al MORB from other slow and intermediate spreading ridges and close to fracture zones elsewhere. In order to understand the origin of these high-Al glasses, I use a forward modeling approach to explore the relative contributions of source, melting and differentiation processes. Thermodynamic modeling of the sample chemistry using the MELTS and pMELTS algorithms (Ghiorso and Sack, 1995; Ghiorso et al., 2002) shows that high-pressure (0.3-0.4 GPa) crystallization can account for the unusually high Al and low Si contents of these glasses. Because samples with these characteristics are mainly restricted to ridges with fairly slow spreading rates or near the ends of ridge segments elsewhere, this study has important implications for processes at these settings. I conclude that high-pressure fractionation is either restricted to low magma supply settings, or alternatively, that the chemical signature of high-pressure fractionation will only be preserved in locations that lack a well-developed magma chamber.

Chapter 3 explores the relationship between magmatic processes and eruptive style using two case studies from the Western Volcanic Zone of Iceland. In this chapter, I examine two units, Lambahraun and Thjófahraun, which erupted very close to one another both spatially and temporally but exhibit very different eruption styles and chemistry. The goal of this project was to understand differences in eruptive style and chemical variability in these two units and determine what inferences can be made about their underlying magmatic processes. This study particularly highlights differences in magma transport and storage processes, with one unit displaying CaO and trace element enrichments interpreted to be a consequence of crustal interaction during magma ascent. Although crustal interaction has long been argued as a potential complicating factor in mid-ocean ridge evolution, most of the primary data for this process has come from studies of oceanic gabbros. Only rarely has this process been invoked to explain chemical variations in erupted lavas. The recognition of crustal interaction in some large volume, long duration Icelandic eruptions has implications for the nature of magma pathways and storage areas that feed fissure eruptions and lava shields in Iceland, and possibly elsewhere.

The findings from Chapter 3 led to further exploration of crustal assimilation using a numerical modeling approach described in Chapter 4. In this study, I use a simple thermal model in order to examine the first-order effects of magma migration through mafic crust and the thermal consequences of heat exchange between magma and its surrounding wallrock. The results from this preliminary study indicate that ascending magma is likely to cause partial melting of the surrounding wallrock during long-lived eruptions with sustained magma supply. This crustal interaction has important geochemical consequences for the erupted lavas, with implications for the common practice of using MORB compositions to make inferences about mantle melting and source composition.

1.2 Background and setting

1.2.1 Galápagos Spreading Center

Chapter 2 examines chemical variations along a portion of the Galápagos Spreading Center (GSC). The roughly east-west trending GSC separates the Cocos and Nazca plates in the eastern equatorial Pacific, and is influenced by the Galápagos hotspot near 90.5ºW. The Galápagos Plume Ridge Interaction Multidisciplinary Experiment (G-PRIME) resulted in a collection geochemical and geophysical data along an ~ 800 km-long portion of the ridge, including detailed bathymetric mapping, seismic refraction, reflection, magnetics, and an extensive rock sample suite that has been analyzed for glass and whole-rock compositions as well as selected trace and isotope analyses (Canales et al., 2002; Detrick et al., 2002; Sinton et al., 2003; Cushman et al., 2004). While G-PRIME was designed to explore the plume-ridge interaction and its opportunities for insight into various magmatic processes, the sample suite yielded some unusual MORB compositions even in the "normal" portion of the mid-ocean ridge west of 95.5°W, outside the hotspot's sphere of influence.

Normal (N-)MORB, defined as having K/Ti ratios < 0.09 (Cushman et al., 2004), dominate this region of the spreading center. Some N-MORB glass samples from this region have very high Al contents (> 16.0 wt. % Al_2O_3 at > 8.5 wt. % MgO), similar to high-Al N-MORB from other slow and intermediate spreading ridges and close to fracture zones elsewhere. GSC high-Al N-MORB are dominated mineralogically by uniform plagioclase compositions (An 80-82) with only 1-2% olivine (Fo 85-87), and have glass compositions with higher Al_2O_3 and lower SiO_2 than is predicted by normal MORB fractionation trends.

1.2.2 Western Volcanic Zone, Iceland

One of the major outstanding problems of mid-ocean ridge research is understanding processes on the scale of individual volcanic eruptions. We would like to be able to evaluate melting and differentiation processes, eruptive style, magma supply and crustal storage characteristics, and whether there are any systematic relationships between these properties. In order to address this, one needs to know physical characteristics of individual units such as flow morphology, eruptive vent characteristics, erupted volume estimates, as well as have sufficient sampling to quantify any chemical heterogeneity that is present. This detailed level of mapping is extremely difficult to accomplish on the seafloor, and consequently studies at the scale of individual submarine eruption units are rare (Perfit and Chadwick, 1998; Embley et al., 2000; Sinton et al., 2002; Bergmanis et al., 2007).

The Western Volcanic Zone (WVZ) of Iceland is an ideal location for an investigation of this scale. A significant (~ 170-km long) portion of the Mid-Atlantic Ridge has been mapped on the scale of individual eruptions (Sinton et al., 2005). All post-glacial (since ~ 12 ka) units have been sampled and analyzed for major and trace elements, and age constraints have been determined for all eruptions from ^{14}C-dating and tephrochronology. Lava flow fields produced during single eruptive episodes range from ~0.1 to >15 km^3 and encompass a wide range in lava morphology and styles of eruptive activity. The spatial and temporal constraints along with the eruptive variability along this portion of the ridge make this an ideal location to investigate a variety of volcanic processes, including spatial and temporal variations in eruption style, melting and differentiation processes, and source heterogeneity.

Volcanic eruptions in Iceland and elsewhere occur from either fissures or central vents (lava shields), providing opportunities to compare these two eruptive styles and examine their respective geologic evolutions. The volume and chemical heterogeneity of an eruption have important implications for magma supply and the nature of crustal storage. The volume of magma available for an eruption is dependent on both the amount stored in crustal reservoirs and the rate of new mantle-derived magma being supplied to the eruption. Eruptions dominated by magma recharge can be expected to exhibit a number of characteristics that differ from eruptions that tap a single, large reservoir. The rate of such an eruption may be partly constrained by the magma supply rate, while an eruption driven by overpressure from a single volume of resident magma in a shallow chamber can have a much higher eruption rate. Eruptions of this latter kind can provide important constraints on reservoir size, magma residence time and ascent rates.

Sinton et al. (2005) proposed that fissure eruptions tap extant, well-mixed crustal magma chambers, whereas the chemical variations in lava shields are inconsistent with large, well-mixed magma reservoirs and seem to require mantle recharge during the course of several decade-long eruptions. Two specific WVZ eruptions – a lava shield (Lambahraun) and a fissure eruption (Thjófahraun) – were selected for a more detailed petrologic study of the erupted products of these different eruptive styles.

1.2.2.1 Lambahraun and Thjófahraun

Lambahraun and Thjófahraun erupted approximately 4,000 years ago with source vents located within ~ 25 km of one another along the ridge. Thjófahraun erupted ~ 1km^3 of pāhoehoe and ‘a‘ā lava from a highly effusive fissure system approximately 9-km long (Sinton et al., 2005). Whole-rock analyses of samples from this unit span a narrow range of MgO and limited geochemical variability, consistent with a melt that has resided in a well-mixed crustal magma reservoir. While Thjófahraun exhibits little internal chemical variability, field observations and mineralogical variations have allowed us to distinguish ~ 19 different subunits, many of which can be correlated with specific vent locations. Relative age relations between subunits allow us to trace this eruption’s chemical and mineralogical variability through time. In contrast, Lambahraun is a large lava shield with an estimated > 7 km^3 of erupted lava. This unit is dominated by relatively low effusion rate pāhoehoe lava, suggesting an eruption period of several decades and a magma supply fed by continuous recharge from the mantle. Greater geochemical variability in this lava shield indicate a more complicated magmatic evolution than is observed for Thjófahraun.

1.2.3 Crustal interaction

Although the potential geochemical importance of melt-wallrock interaction was recognized nearly a century ago by Bowen through simple phase equilibria treatments of the problem (1922a, 1922b, 1928), the extent to which crustal assimilation plays a role in the formation of MORB is still unknown. The geochemical signature of this process may be obscure in the erupted basalts at mid-ocean ridges, where the host rock is largely similar in composition to the primary magmas and the resulting trace element enrichments may even resemble source melting variations. The majority of MORB petrologic studies assume magmas reach the surface without reacting with the surrounding crust and therefore mantle source compositions and melting parameters can be derived from the erupted lava compositions. However, a growing collection of literature indicates melt-wallrock interaction may be an important contributor to the geochemical evolution of MORB. Evidence for such interactions comes primarily from lower crustal rocks. Coexisting minerals in oceanic gabbros often show evidence of chemical and textural disequilibrium (e.g., Elthon, 1987; Meyer et al., 1989; Elthon et al, 1992; Natland and Dick, 1996; Bédard et al., 2000; Coogan et al., 2000; Dick et al., 2002). In Iceland, crustal interaction has been called on to explain trace element and isotopic enrichments in some erupted lavas (Muehlenbachs et al., 1974; Óskarsson et al., 1982; Condomines et al., 1983; Hémond et al., 1988; Nicholson et al., 1991; Maclennan, 2008; Halldórsson et al., 2008), including the study presented in Chapter 3 of this dissertation.

Because of its role in unraveling melting and differentiation histories, it is important to further constrain the extent to which MORB melts interact with the crust during their ascent from the mantle to the surface. Modern investigations into this problem have focused primarily on wallrock assimilation in the context of magma chambers (Allègre and Minster, 1978; Taylor et al., 1979; Taylor, 1980; Grove and Kinzler, 1986; Aitcheson and Forrest 1994; Reiners et al., 1995; Marsh, 1995, 1998; Edwards and Russell, 1998; Spera and Bohrson, 2001), or in the lower crust, where evidence suggests melt migration occurs as reactive porous flow through a crystal mush (e.g., Keleman, 1990; Coogan et al., 2000; Lissenberg and Dick, 2008). Another part of the system in which this might occur is during magma ascent through moderate to shallow crustal levels, as suggested by the research on Lambahraun lava shield detailed in Chapter 3. As this problem is relatively unexplored, we build on the results from that chapter and develop a simple thermal model exploring the conditions under which crustal interaction might play an important role on the geochemical evolution of MORB.

1.3 Dissertation structure

Chapter 2 describes forward modeling of the glass and mineral chemistry of GSC high-Al N-MORB using the MELTS and pMELTS algorithms (Ghiorso and Sack, 1995; Ghiorso et al., 2002) with constraints from local crustal thickness measurements. These petrological models indicate that high-Al, low-Si MORB can be produced by high-pressure crystallization in the upper mantle using the same source as normal (low-Al) GSC N-MORB. Although high-Al glasses can by obtained by very low extents of partial melting of this mantle source, we find that such melting models result in significant misfits in other major element oxides, particularly SiO_2. Models involving significant olivine and clinopyroxene crystallization at pressures of 0.3-0.4 GPa can account for the observed major and trace element composition of these unusual MORB samples. This work was published in *Earth and Planetary Science Letters* in November 2006 (vol. 252).

Chapter 3 explores the geologic and magmatic evolution of Lambahraun lava shield and the Thjófahraun fissure eruption in the WVZ using a combination of integrated field observations, whole-rock and mineral geochemical analyses, and petrologic modeling. Results from this study indicate Thjófahraun lava compositions are consistent with evolution by crystal fractionation in a shallow magma chamber, while Lambahraun's geochemical variability sheds light on more complex crustal processes. Some Lambahraun samples have high Al_2O_3 and low TiO_2 and FeO, the result of up to 15 % plagioclase accumulation. In addition, all samples from Lambahraun exhibit increasing CaO with decreasing MgO and overall incompatible-element enrichments greater than predicted by crystal fractionation alone. Geochemical modeling indicates the observed correlations among incompatible element concentration, increasing differentiation and time during the eruption can be related by concurrent wallrock assimilation and crystallization during melt migration through the crust. We refer to this process as migrating assimilation and fractional crystallization (MAFC). This chapter was published in September 2009 in *Journal of Volcanology and Geothermal Research* (vol. 186).

Chapter 4 builds on the results of Chapter 3 and examines the thermal conditions that lead to wallrock partial melting during magma ascent through the crust. In this chapter, I develop a 2-dimensional numerical model in order to explore the first-order effects of magma migration through mafic crust, and determine the feasibility of this process leading to the geochemical variations observed at large volume lava shields in the WVZ of Iceland. The results from this preliminary study indicate that ascending magma is likely to cause significant amounts (3-10% of total erupted magma budget) of low-degree partial melting of the surrounding wallrock during long-lived, low-effusion rate eruptions.

Chapter 5 summarizes the conclusions from these studies and outlines areas where additional work is needed to more fully elucidate some of the questions posed by this research, providing future directions for further investigation.

CHAPTER 2

ORIGIN OF HIGH-AL N-MORB BY FRACTIONAL CRYSTALLIZATION IN THE UPPER MANTLE BENEATH THE GALÁPAGOS SPREADING CENTER

2.1 Abstract

The Galápagos Spreading Center (GSC) includes lavas with chemical compositions ranging from N-MORB to transitional and more enriched MORB. N-MORB dominate the region west of 95.5ºW, far from the influence of the Galápagos hotspot. However, some N-MORB glass samples from the GSC have very high Al contents (> 16.0 wt. % Al_2O_3 at > 8.5 wt. % MgO), similar to high-Al N-MORB from other slow and intermediate spreading ridges and close to fracture zones elsewhere. GSC high-Al N-MORB are dominated mineralogically by uniform plagioclase compositions (An 80-82) with only 1-2% olivine (Fo 85-87), and have glass compositions with higher Al_2O_3 and lower SiO_2 than is predicted by normal MORB fractionation trends. Forward modeling using the MELTS and pMELTS algorithms constrained by crustal thickness measurements indicates that high-Al, low-Si MORB can be produced by high-pressure crystallization in the upper mantle using the same source as normal (low-Al) GSC N-MORB. Although high-Al glasses can be obtained by very low extents of partial melting of this mantle source, such melting models result in significant misfits in other major element oxides, especially SiO_2. Models involving significant evolution with up to 20% olivine and clinopyroxene crystallization at pressures of 0.3-0.4 GPa can account for the complete major and selected trace element compositions of these unusual MORB

samples. We suggest that high-pressure fractionation is enhanced by conductive cooling of the upper mantle in this area of the GSC, consistent with other recent models correlating mantle crystallization with slow spreading mid-ocean ridges and fracture zones.

2.2 Introduction

The nearly east-west trending GSC separates the Cocos and Nazca plates in the eastern equatorial Pacific (Fig. 2.1). Samples from this study were collected during the Galápagos Plume Ridge Interaction Multidisciplinary Experiment (G-PRIME), which included detailed bathymetric mapping, and the collection of seismic refraction, reflection, and magnetics data and rock samples along an ~800 km-long portion of the ridge extending from 90.5°W, just north of the Galápagos Archipelago and the inferred location of the Galápagos mantle plume, to 98°W, the region of the GSC considered to be a "normal" mid-ocean ridge (Detrick et al., 2002). Full spreading rates along this portion of the ridge vary from 46 mm/yr at 98°W to 56 mm/yr at 91°W near the Galápagos hotspot (DeMets et al., 1994).

The G-PRIME sample suite includes chemical compositions varying from normal (N-) to transitional (T-) and more enriched (E-) mid-ocean ridge basalts (MORB) (Detrick et al., 2002; Cushman et al., 2004). N-MORB dominate the area west of the propagating rift at 95.5°W, which appears to be the limit of geochemical influence of the Galápagos hotspot. Samples west of the propagating rift show little or no evidence of plume enrichment, while samples to the east show increasing incompatible element and

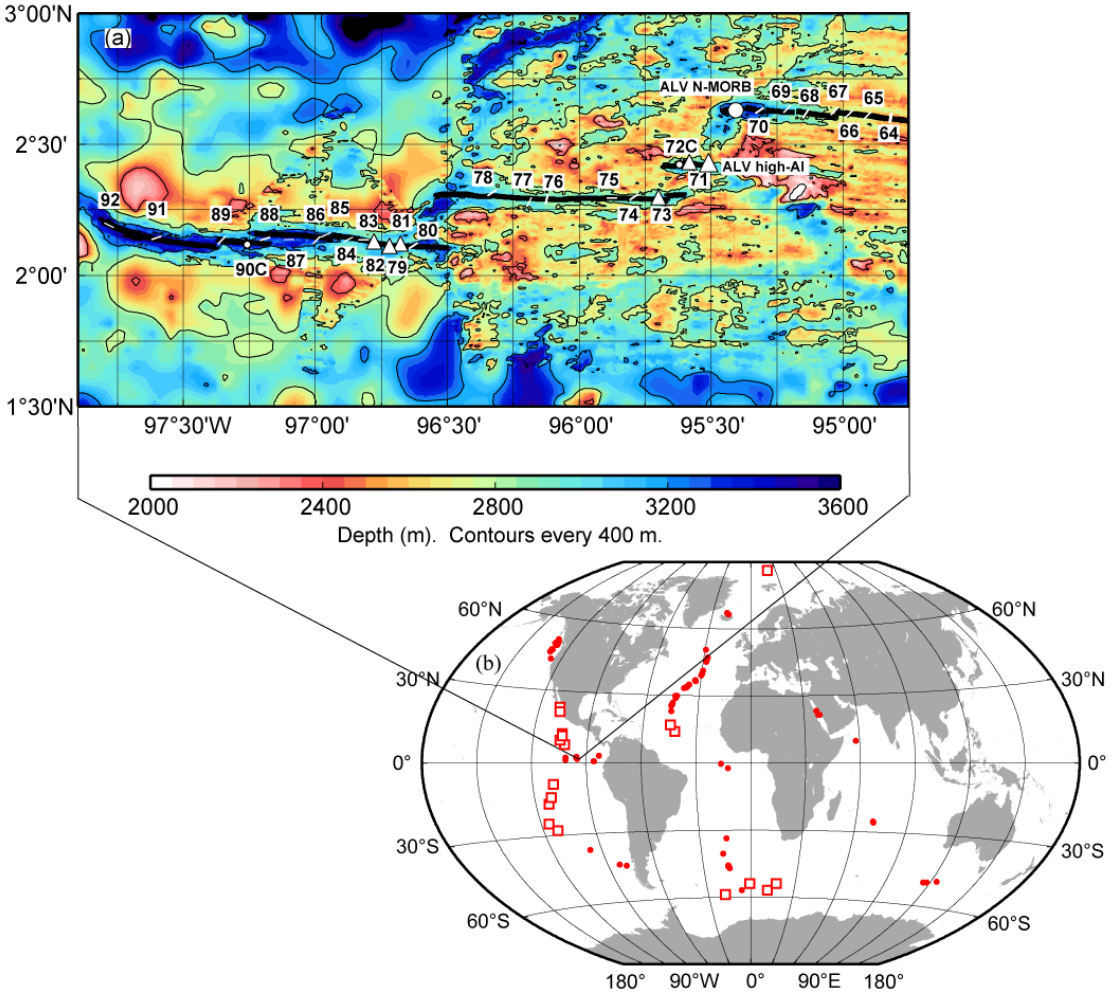

Figure 2.1 (a) Sample locations along part of the western Galápagos Spreading Center. Station numbers are those for the G-PRIME expedition (Detrick et al., 2002; Cushman et al., 2004). ALVIN (ALV) samples from Hey et al. (1992). High-Al sample locations are shown as triangles. Thick black line denotes the GSC axis from Sinton et al. (2003). (b) Global distribution of samples in PetDB (Lehnert et al., 2000) with $Al_2O_3 > 16.0$ wt. %, $MgO > 8.5$ wt. %. Open squares denote fracture zone samples.

isotopic enrichment approaching the plume (~91.7°W) (Fisk et al., 1982; Schilling et al., 1982; Verma et al., 1982, 1983; Cushman et al., 2004).

Galápagos N-MORB are characterized by moderate to high MgO values (ranging from 6.9 wt. % MgO to nearly 10 wt. % MgO) and low concentrations of elements that are incompatible during mantle melting (≤ 0.08 wt.% K_2O, 1.67-2.56 wt.% Na_2O, 0.77-1.68 wt.% TiO_2, 0.05-0.12 wt.% P_2O_5), with K/Ti ratios < 0.09. GSC N-MORB also have low water contents (no greater than 0.22 wt. % H_2O, with an average of 0.16 wt. % H_2O). Cushman et al. (2004) argued that average Galápagos N-MORB could be produced from a mean fraction of partial melting ($\overline{F}$) ~0.06 of a source with ~34±1 ppm K, 133±3 ppm H_2O, 2250±50 ppm Na_2O, and 1050±25 ppm Ti.

Some of the N-MORB glass samples from the GSC have unusually high Al_2O_3 contents (> 16.0 wt. %) at MgO > 8.5 wt. %. These samples have higher aluminum and lower silica than predicted by normal MORB fractionation trends while maintaining very low potassium and sodium values. According to MELTS models of their glass compositions (Ghiorso and Sack, 1995), they are saturated with plagioclase at low pressures even at MgO > 9.0 wt. %, consistent with experimental data reported for other high-Al MORB (e.g., Sisson and Grove, 1993; Panjasawatwong et al., 1995). High-MgO basalts with unusually high aluminum content also have been reported for various mid-ocean ridges (see Fig. 2.1), although their origin is not fully understood (e.g., Sobolev et al., 1989; Nielsen et al., 1995; Meurer et al., 2001). These high-Al MORB are distinct from the high-Al basalts and andesites often associated with arcs, which tend to be more evolved with higher K and H_2O contents. Such high-Al, low-Si basalts appear to be restricted to ridges with slow spreading rates or close to fracture zones and ridge terminations. Along the GSC, high-Al samples are located close to ridge segment ends or associated with failing rifts (Fig. 2.1).

The extensive dataset available from G-PRIME makes the Galápagos an ideal location to examine the melting and fractionation processes that give rise to high-Al MORB compositions. Glass data for the sample suite were reported in Cushman et al. (2004), and whole-rock XRF data are reported for Galápagos N-MORB in Table 2.1. Estimates of GSC crustal thickness from multichannel seismic reflection data (Canales et al., 2002; Detrick et al., 2002) put a limit on melt productivity, giving us an important modeling constraint.

To supplement the glass and whole rock analyses, we collected mineral compositions, zoning profiles, and modes in five high-Al GSC samples. Using this combination of petrographic and chemical data, we are able to model the feasibility of various melting and fractionation paths using the MELTS and pMELTS algorithms (Ghiorso and Sack, 1995; Asimow and Ghiorso, 1998; Ghiorso et al., 2002; Smith and Asimow, 2005) by comparing the phase compositions and abundances resulting from each evolution path with the chemistry of the rocks themselves. We first establish a working model that produces the array of normal GSC N-MORB under reasonable ridge melting and crystallization conditions, then use the determined source composition to model the evolution of the high-Al samples. By varying the pressure and extent of partial melting of the GSC source as well as the pressure and extent of subsequent fractional crystallization of these hypothetical parental magmas, we can constrain 1) possible source depths that the high-Al magmas could be generated, 2) the range of partial melting that allow these high-Al compositions, and 3) the range of depths where these magmas may have evolved. This forward modeling approach allows us to eliminate impossible processes and constrain ridge melting and evolution to a restricted range of conditions.

2.3 Data and Methods

Whole rock x-ray fluorescence (XRF) data were measured on the University of Hawaii Siemens 303 AS XRF spectrometer using a Rh-target, end-window x-ray tube. Whole rocks were crushed in an alumina swing mill, and powders were analyzed for major elements on fused disks following methods similar to those of Norrish and Hutton (1977). Trace elements were analyzed on pressed powder pellets. Peak intensities for the trace elements were corrected for backgrounds, line interferences and matrix absorption using methods similar to Chappell (1992). Corrected intensities were calibrated against a wide range of natural rock standards. Accuracy and precision data for this system are reported in Sinton et al. (2005).

Glass and mineral compositions were collected using the University of Hawaii Cameca SX-50 five-spectrometer electron microprobe. Major and minor element analyses for GSC glasses are reported in Cushman et al. (2004). Mineral analyses reported here are averages of three spots collected from individual crystals in selected high-Al MORB. Plagioclase was analyzed for Si, Al, Fe, Mg, Ca, Na and K using an accelerating voltage of 15 kV, 20 nA beam current, and 10 μm beam diameter. Peak counting times were 30 seconds for Si, Mg, Al, and Na and 60 seconds for Fe, Ca, and K. Background counting times were 30 seconds for Fe, Ca, and K; 15 seconds for Si, Mg, and Al; and 20 seconds for Na. Na was analyzed first in each acquisition to minimize

Table 2.1 Whole-rock XRF analyses for GSC N-MORB, incl. G-PRIME (EW), Alvin (AL) and Atlantis (A) samples (63). Oxide abundances given in wt. %, trace elements in ppm. Depth given as mbsl.

Sample	**EW43-1**	**EW63-1**	**EW63-2**	**EW71-1**	**EW71-4**	**EW77-2**	**EW79-1**
Long	-93.257	-94.747	-94.747	-95.602	-95.602	-96.191	-96.725
Lat	2.414	2.954	2.954	2.425	2.425	2.281	2.100
Depth	2243	2655	2655	2768	2768	2851	3136
SiO_2	49.72	49.68	48.88	48.64	48.76	49.63	48.22
TiO_2	0.92	1.16	1.27	1.01	1.01	1.17	0.97
Al_2O_3	14.82	15.41	15.64	15.80	15.70	15.60	17.29
Fe_2O_3*	10.37	11.11	12.12	10.34	10.52	10.61	10.41
MnO	0.16	0.17	0.18	0.17	0.17	0.17	0.15
MgO	8.66	8.12	8.05	9.77	9.87	8.17	8.98
CaO	13.28	12.48	11.84	12.17	12.24	12.67	11.94
Na_2O	1.52	1.80	2.09	2.13	1.75	1.92	2.23
K_2O	0.04	0.05	0.09	0.06	0.04	0.04	0.04
P_2O_5	0.07	0.08	0.09	0.07	0.07	0.08	0.07
Sum	99.56	100.04	100.24	100.15	100.13	100.05	100.30
Sc	48	44	45	46	46	46	35
V	307	336	286	271	266	323	216
Cr	338	343	295	520	533	387	326
Co	48	45	48	52	52	45	48
Ni	98	113	115	211	228	111	169
Cu							
Zn	72	83	88	66	67	78	73
Rb	1.5	1.8	2.3	1.4	1.5	1.2	1.1
Sr	63	71	100	95	95	85	110
Y	21	28	28	24	25	27	21
Zr	43	63	73	59	59	65	53
Nb	2.0	2.4	3.8	1.8	1.9	1.9	1.9

Table 2.1 (Continued) Whole-rock XRF analyses for GSC N-MORB

Sample	**EW80-2**	**EW81-3**	**EW82-8**	**EW83-5**	**EW84-2**	**EW87-1**	**EW88-1**
Long	-96.630	-96.697	-96.775	-96.818	-96.877	-97.100	-97.192
Lat	2.115	2.120	2.122	2.138	2.139	2.139	2.142
Depth	3071	3062	3025	2957	3042	3272	3229
SiO_2	49.41	48.38	47.77	49.50	49.86	49.89	50.02
TiO_2	1.10	0.89	1.00	1.25	1.21	1.11	1.15
Al_2O_3	16.04	17.10	17.70	15.73	15.05	15.79	15.42
Fe_2O_3*	10.06	9.20	9.99	10.74	10.91	10.12	10.42
MnO	0.16	0.15	0.15	0.17	0.17	0.16	0.16
MgO	8.76	9.69	9.28	8.71	8.42	8.62	8.38
CaO	12.67	12.48	12.17	12.14	12.12	12.66	12.55
Na_2O	2.08	2.04	2.09	1.91	1.72	1.87	2.10
K_2O	0.02	0.02	0.02	0.04	0.04	0.03	0.05
P_2O_5	0.06	0.05	0.05	0.08	0.09	0.07	0.09
Sum	100.35	99.98	100.22	100.25	99.59	100.31	100.33
Sc	43	39	42	44	44	44	41
V	263	221	195	300	308	280	292
Cr	443	468	325	405	388	458	464
Co	46	50	49	47	48	44	45
Ni	137	203	201	154	124	140	129
Cu							
Zn	71	62	63	80	82	73	74
Rb	0.9	1.2	0.6	1.4	1.4	1.1	1.2
Sr	91	92	113	84	83	80	76
Y	26	22	23	30	31	27	28
Zr	62	50	61	70	74	62	64
Nb	1.1	1.7	0.9	1.9	3.0	1.6	2.0

Table 2.1 (Continued) Whole-rock XRF analyses for GSC N-MORB

Sample	**EW91-6**	**EW92-1**	**AL-1545-4**	**AL-1545-6**	**AL-1549-3**	**AL-1549-4**	**AL-1549-5**
Long	-97.604	-97.782	-95.37	-95.38	-95.38	-95.38	-95.38
Lat	2.145	2.193	2.63	2.63	2.63	2.63	2.63
Depth	3440	3360	3229	3145	3176	3172	3181
SiO_2	49.71	49.77	49.66	49.60	49.63	49.73	49.48
TiO_2	1.05	1.40	0.99	0.99	0.98	0.95	0.92
Al_2O_3	15.42	15.13	15.87	15.92	15.86	15.10	14.93
Fe_2O_3*	10.37	11.04	10.70	10.81	10.66	10.57	10.51
MnO	0.16	0.17	0.16	0.16	0.16	0.16	0.16
MgO	9.05	8.42	9.00	8.98	9.08	8.92	9.07
CaO	12.35	11.69	12.54	12.58	12.57	12.59	12.51
Na_2O	1.81	1.95	1.50	1.51	1.55	1.81	1.80
K_2O	0.04	0.07	0.04	0.04	0.04	0.05	0.04
P_2O_5	0.06	0.12	0.10	0.11	0.10	0.05	0.05
Sum	100.02	99.74	100.56	100.70	100.63	99.93	99.47
Sc	43	44	42	44	42	44	43
V	285	338	286	289	288	284	291
Cr	453	355	496	501	497	502	493
Co	47	47	47	48	46	46	44
Ni	160	135	161	163	167	175	165
Cu			83	85	85	89	85
Zn	75	83	76	76	77	80	77
Rb	1.5	1.3	1.3	1.2	1.1	1.6	1.0
Sr	75	87	70	70	70	76	70
Y	26	33	25	24	24	26	24
Zr	60	87	55	55	55	59	55
Nb	1.7	2.4	2.0	1.9	2.1	2.1	2.1

Table 2.1 (Continued) Whole-rock XRF analyses for GSC N-MORB

Sample	AL-1550-2	AL-1551-3	AL-1552-8	AL-1554-1	A3-A	A3-B	A13-2
Long	-95.54	-95.48	-95.53	-95.48	-95.53	-95.53	-95.62
Lat	2.36	2.41	2.38	2.42	2.37	2.37	2.31
Depth	2270	3063	2274	2912	2575	2575	3060
SiO_2	49.98	49.02	48.77	48.56	50.19	49.48	49.95
TiO_2	0.84	1.07	1.00	1.03	1.06	0.95	1.15
Al_2O_3	15.77	15.97	15.61	15.50	15.45	16.42	15.64
Fe_2O_3*	9.37	9.81	10.82	10.28	10.26	9.28	10.45
MnO	0.15	0.15	0.16	0.15	0.16	0.14	0.16
MgO	9.11	9.10	9.45	9.99	8.61	8.79	8.01
CaO	12.89	12.21	11.96	11.72	12.35	12.61	12.31
Na_2O	1.95	2.44	1.97	2.16	1.77	1.73	1.75
K_2O	0.05	0.06	0.03	0.04	0.06	0.04	0.06
P_2O_5	0.04	0.05	0.05	0.05	0.09	0.07	0.09
Sum	100.15	99.88	99.82	99.48	99.99	99.51	99.55
Sc	40	41	42	40	44	42	43
V	239	248	264	256	297	239	314
Cr	621	490	498	519	445	530	388
Co	42	46	48	47	46	43	44
Ni	163	175	197	227	140	161	122
Cu	79	81	79	81			
Zn	64	67	74	70	73	66	76
Rb	1.0	0.9	1.2	1.1	1.8	1.3	1.8
Sr	83	118	75	91	85	87	81
Y	21	24	27	25	25	22	26
Zr	47	68	57	64	59	51	62
Nb	2.0	1.7	1.8	2.2	2.4	1.9	2.6

* Total Fe as Fe_2O_3.

Negative loss on ignition at 900ºC for all samples. Ba, Pb, Th, U are below detection limits, averaging 10, 2, 1.3, and 1.5 ppm respectively.

loss due to volatilization. Samples were calibrated against mineral standards Lake County plagioclase (Si and Al), San Carlos olivine (Fe and Mg), Amelia albite (Na), anorthite (Ca) and orthoclase (K). A PAP-ZAF matrix correction was applied to all analyses.

Olivine was analyzed for Si, Mg, Fe, Ca, Mn and Ni using an accelerating voltage of 20 kV, 30 nA beam current, and 10 μm beam diameter. Peak counting times were 60 seconds for Mg and Si; 80 seconds for Ca and Ni; 50 seconds for Fe; and 40 seconds for Mn. Background counting times were 30 seconds for Mg and Si; 40 seconds for Ca and Ni; 25 seconds for Fe; and 20 seconds for Mn. Samples were calibrated against San Carlos olivine (Mg), Springwater olivine (Fe), Verma garnet (Mn), diopside (Si and Ca) and Ni-metal (Ni) standards. A PAP-ZAF matrix correction was applied to all analyses.

It should be noted that the whole-rock Na content is consistently lower than the glass Na for the same rock, possibly indicating partial volatilization of Na during fusion as part of the XRF sample preparation for major elements. This does not affect the results presented in subsequent sections, as all modeling is done using glass Na content rather than whole-rock data.

Thin sections were examined for textural indications of disequilibrium and 1000-point counts were collected on selected high-Al samples to determine mineral modes (see supplementary material). Mineral grains < 0.05 mm in size appear to have crystallized post-eruption, and are considered “groundmass” for counting purposes, so that our mode reflects the phenocryst assemblage rather than evolution after eruption.

Forward modeling of the samples’ geochemical evolution was done primarily using Adiabat_1ph (Smith and Asimow, 2005), the latest release of the MELTS and pMELTS algorithms for thermodynamic modeling of phase equilibria in magmatic systems (Ghiorso and Sack, 1995; Ghiorso et al., 2002). Also included in this release is pHMELTS, which models the effects of water storage in nominally anhydrous minerals using trace element partitioning to distribute H_2O between the system and a separate hidden reservoir (Asimow et al., 2004).

2.4 Mineralogy

The high-Al MORB samples range from nearly aphyric to ~18% phenocrysts (Table 2.2). Phenocryst assemblages are dominated by sub- to euhedral plagioclase, comprising up to 90% of the mineral mode, or up to 15% of the total rock mode. Plagioclase phenocrysts are tabular to elongate, up to 2 mm in width. These rocks also contain a small amount of olivine (1-2%) as sub- to euhedral grains, <1 mm across. Mineral compositions are fairly uniform across the sample suite, with plagioclase compositions averaging ~An 80-82 and olivine compositions of Fo 85-87 (Table 2.3). Profiles across plagioclase grains indicate a small degree of zoning, which can be both normal and reverse within a given sample. There is no textural evidence of disequilibrium, such as strong zoning or resorption, that might indicate a process such as plagioclase assimilation. Some plagioclase grains contain melt inclusions, but they are too devitrified to yield good glass compositions. While most plagioclase phenocrysts are euhedral, a few are fractured and less well-formed, although there does not appear to be a compositional distinction between the two types. The groundmass in these samples ranges from glassy to cryptocrystalline with abundant microspherulites. EW 82-8 contains small clinopyroxene grains up to 0.05 mm across associated with radial plagioclase glomerocrysts in the groundmass, but there are no phenocrysts of clinopyroxene in any of the high-Al samples.

Table 2.2 High-Al rock modes based on 1000-point counts.

	Relative Phase Abundance (%)				
sample	**olivine**	**plagioclase**	**groundmass**	**vesicles**	**total**
EW 71-4	0.9	0.6	97.4	1.1	100.0
EW 73-1	1.5	3.3	94.5	0.7	100.0
EW 79-1	1.6	15.5	81.3	1.6	100.0
EW 81-3	1.3	5.4	92.7	0.6	100.0
EW 82-8	0.9	8.7	89.6	0.8	100.0

2.5 Galápagos N-MORB

We use a two-stage forward model to determine a reasonable GSC mantle source composition appropriate to our rock chemistry. In the first stage, we model melting processes using pHMELTS, constrained by a target crustal thickness of $Z_c \sim$ 5.6-6.0 km (Canales et al., 2002; Detrick et al., 2002). Melting runs simulate adiabatic decompression, setting entropy, S, (or potential temperature, T_0) to control the depth at which the solidus is reached and melting begins. Melting is treated as continuous, where a small fraction (0.005) of melt is retained at each extraction step. Model melting continues to the base of the crust, where the fractional melts are then aggregated. We assume passive mantle upwelling, integrating for a 2-D (triangular) melting regime to

Table 2.3 Representative mineral analyses of high-Al samples.

Representative Analyses of Plagioclase

Sample	**EW 73-1**	**EW 79-1**			**EW 81-3**	**EW 82-8**		
Anal.		1	2	3		1	2	3
SiO_2	48.2	47.4	48.3	47.7	47.4	47.9	47.7	49.0
Al_2O_3	33.8	33.9	33.8	34.0	34.2	33.6	34.0	33.1
FeO*	0.39	0.41	0.41	0.40	0.30	0.35	0.37	0.38
MgO	0.24	0.21	0.23	0.22	0.22	0.24	0.23	0.25
CaO	16.4	16.6	16.3	16.7	16.8	16.6	16.8	15.8
Na_2O	2.05	1.88	2.06	1.85	1.82	1.99	1.84	2.42
Total**	101.1	100.4	101.1	100.9	100.7	100.7	100.9	101.0
Cations on the basis of 8 oxygens								
Si	2.183	2.164	2.189	2.168	2.160	2.181	2.169	2.219
Al	1.806	1.827	1.802	1.822	1.834	1.805	1.820	1.768
Fe	0.013	0.014	0.014	0.014	0.010	0.012	0.013	0.013
Mg	0.016	0.014	0.015	0.015	0.015	0.017	0.016	0.017
Ca	0.798	0.812	0.792	0.813	0.818	0.808	0.816	0.767
Na	0.180	0.166	0.181	0.163	0.161	0.176	0.162	0.213
Total	4.997	4.998	4.994	4.995	4.998	4.999	4.995	4.996
An †	81.6	83.0	81.4	83.3	83.6	82.1	83.4	78.3

Representative Analyses of Olivine

Sample	**EW 73-1**		**EW 79-1**		**EW 81-3**		**EW 82-8**	
Anal.	1	2	1	2	1	2	1	2
SiO_2	39.8	39.5	39.5	39.5	38.2	38.2	38.4	38.4
FeO*	12.8	13.1	13.5	12.9	13.0	13.9	13.7	13.0
MnO	0.19	0.21	0.22	0.19	0.18	0.19	0.21	0.19
MgO	46.7	46.5	46.4	46.4	45.6	44.7	44.8	45.8
CaO	0.29	0.32	0.31	0.31	0.30	0.31	0.30	0.29
NiO	0.26	0.21	0.19	0.21	0.21	0.22	0.20	0.21
Total	100.0	99.9	100.0	99.6	97.5	97.5	97.6	97.9
Cations on the basis of 4 oxygens								
Si	0.990	0.988	0.987	0.990	0.981	0.979	0.981	0.982
Fe	0.267	0.274	0.281	0.270	0.278	0.299	0.296	0.277
Mn	0.004	0.005	0.005	0.004	0.004	0.004	0.005	0.004
Mg	1.735	1.732	1.729	1.734	1.743	1.707	1.712	1.743
Ca	0.008	0.009	0.008	0.008	0.008	0.009	0.008	0.008
Ni	0.005	0.004	0.004	0.004	0.004	0.004	0.004	0.004
Total	3.010	3.012	3.013	3.010	3.019	3.001	3.006	3.018
Fo ‡	86.7	86.3	86.0	86.5	86.2	85.1	85.3	86.3

* Total Fe as FeO.

** K2O for all plagioclase analyses is below detection limit: d.l. = 0.017 wt. %

† An = Ca/(Ca+Na+K)

‡ Fo = Mg*100/(Mg+Fe)

form our aggregate melts (Asimow et al., 2001). In stage two of the model, these aggregate melts are cooled at 1.0 kb, appropriate to crustal depths. We model crystallization using the MELTS calibration, which is more accurate at low pressure. Crystallization runs are isobaric and fractional, with an oxygen fugacity setting of FMQ - 2. Major element compositional modeling includes SiO_2, TiO_2, Al_2O_3, FeO*, MgO, CaO, and Na_2O. K_2O and P_2O_5 content have an unrealistically strong effect on the solidus depth when treated as major elements in pMELTS calculations, so we model them here as trace elements. We have also included additional trace elements (Cr, V, Sc and Sr) using partition coefficients from McKenzie and O'Nions (1991, 1995). Here we report results from both anhydrous melting (pMELTS) runs and wet (pHMELTS) source modeling.

Sources tested include the depleted mantle compositions of McKenzie and O'Nions (1991) and Workman and Hart (2005) (henceforth MO and WH, respectively). However, neither of these sources is sufficiently high in SiO_2 or low in K_2O and CaO to reproduce Galápagos N-MORB trends (see Fig. 2.2) with the melting conditions specified above. F and T_0 could not be adjusted sufficiently to match these oxide values in the melt without adversely affecting other major element oxide contents and sacrificing constraints on crustal production. Both the anhydrous and hydrous model GSC sources are lower in K, Ti, Ca and P than MO and WH, and significantly higher in SiO_2 (Table 2.4). When melted to a maximum melt fraction (F_{max}) ~0.19, the dry source produces a crust 5.9 km thick, which is within the observed range (5.6-6.0 km). Our dry model mantle has an entropy of 264.0 J/K, equivalent to a potential temperature of ~1430ºC. Melting begins at an initial pressure (P_0) of 2.47 GPa. Our wet (60 ppm H_2O) mantle has

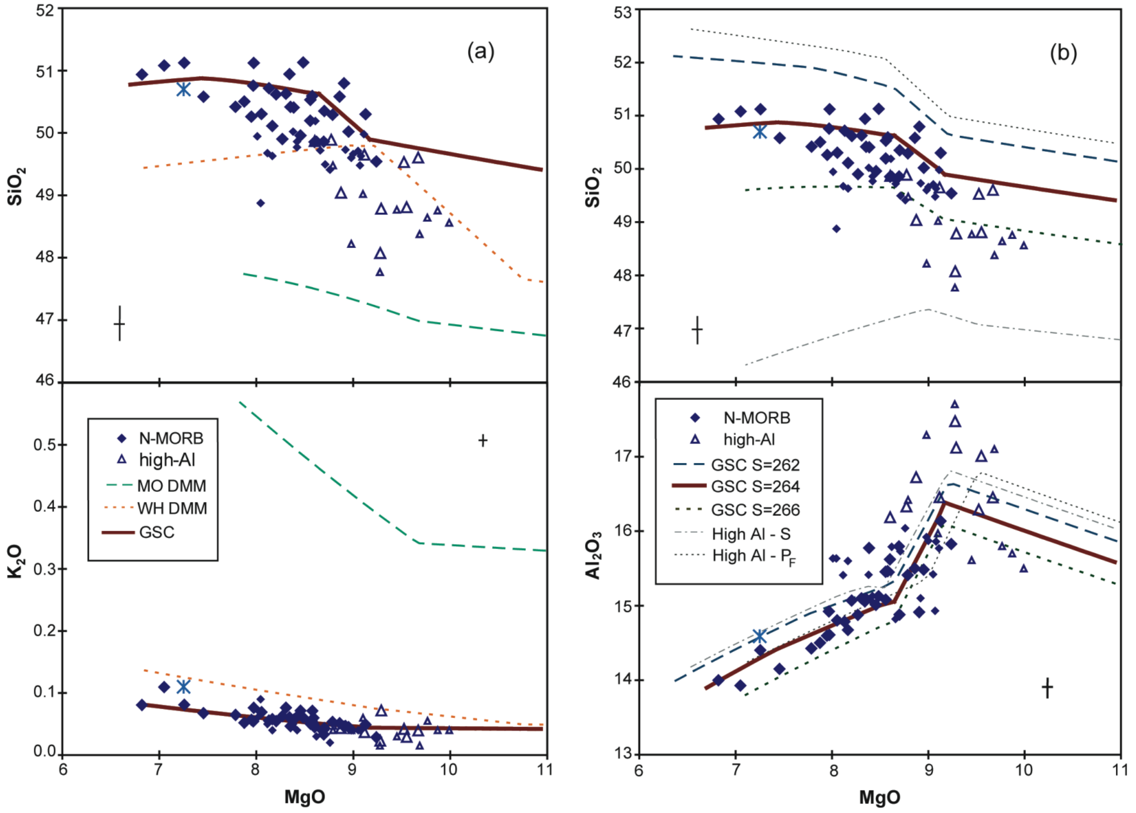

Figure 2.2 Galápagos N-MORB (solid symbols) and high-Al (open symbols) sample data – glass (large symbols) and whole-rock XRF (small symbols). (a) Model comparison of 4 sources (MO = McKenzie and O'Nions (1991); WH = Workman and Hart (2005); GSC = modeled N-MORB dry and wet sources – shown as single line due to close overlap), each partially melted to produce a 5.8-5.9-km thick crust. Aggregate melts are fractionated at P_F =1 kb. (b) Effects of entropy on the model (S in units of J/K), based on dry melting runs. S and P_F lines on Al_2O_3 plot represent attempts to reach high Al liquid content with low degrees of partial melting (from low S or high P_F, respectively). Asterisk denotes the average of 118 whole-rock N-MORB analyses from the southern EPR, 13°-23°S (Sinton et al., 1991; see text for discussion). High-Al

samples chosen using criteria of glass $Al_2O_3 > 16.0$ wt. %, $MgO > 8.5$ wt. %, $SiO_2 < 50.0$ wt. %. Error bars represent ±1σ standard deviation of glass and whole-rock analyses (larger uncertainty of two analytical techniques shown).

Table 2.4 Modeled GSC source and primary magma compositions, with global average DMMs for comparison. H_2O, K, P, Cr, Sr, V, Sc in ppm, other oxide values in wt. %.

	MO DMM[a]	**WH DMM[b]**	**SS DMM[c]**	**Cushman et al. GSC[d]**	**GSC dry DMM[e]**	**GSC wet DMM[e]**	**GSC primary melt (wet)**
SiO_2	45.57	44.71	44.90		47.86	47.86	47.8
TiO_2	0.17	0.13	0.13	0.17	0.10	0.10	0.71
Al_2O_3	2.7	3.98	4.28		2.19	2.20	12.8
Fe_2O_3	0.111	0.191	--		0.07	0.06	0.20
FeO	7.92	8.008	8.07[f]		7.42	7.41	9.14
MgO	40.8	38.73	38.2		40.3	40.3	17.9
CaO	2.41	3.17	3.50		1.90	1.90	9.87
Na_2O	0.24	0.13	0.29	0.23	0.14	0.13	1.48
H_2O	--	--	116	133	--	60	855
K	20	24.9	60	34	10.9	9.8	143
P	40	40.7	40.7		11.3	11.3	134
Cr	3010	3900	2500		300	305	345
Sr	14.7	7.7	9.8		5.4	5	64
V	100	110	79		100	100	204
Sc	12	8.6	16.3		8.6	8.6	30

[a] Global average DMM from McKenzie and O'Nions (1991).

[b] Global average DMM from Workman and Hart (2005).

Table 2.4 (Continued) Modeled GSC source and primary magma compositions

[c] Global average DMM from Salters and Stracke (2004).

[d] GSC oxide concentrations from Cushman et al. (2004) hydrous melting model.

[e] Local GSC mantle source, modeled from N-MORB sample compositions assuming a crustal thickness of 5.6-6.0 km. GSC source composition was determined by adjusting the McKenzie-O'Nions DMM to account for the depletion in Ti, Na, K, and P seen in the GSC N-MORB. The modeled continuous melting path for the dry source begins melting at a pressure P_0 of 2.47 GPa with a potential temperature of ~1430ºC, and melts to an F_{max} ~0.19 to produce a crust 5.9 km thick. For the wet source, melting to an F_{max} ~0.18 from P_0 ~3.07 GPa produces a crust 5.8 km thick. Produced melts then crystallize at a crustal pressure of 1.0 kb to produce the GSC N-MORB trends seen in Fig. 2.2.

[f] Total Fe content (FeO*).

an entropy of 263.5 J/K and begins melting at P_0 ~3.07 GPa, reaching a slightly lower F_{max} ~0.18. Subsequent fractional crystallization at a pressure (P_F) of 1.0 kb yields reasonable fits to GSC N-MORB trends (Fig. 2.2). Fractionating phases include olivine followed by plagioclase, which begins crystallizing at 9.1 wt. % MgO, and clinopyroxene, which joins the assemblage at 8.5 wt. % MgO. These are unusually high Mg-contents for the incoming of plagioclase and clinopyroxene in MORB crystallization sequences, however, the rock assemblages appear to support this. Petrographic observations of the N-MORB suite confirms that plagioclase is a phenocryst phase in virtually all of the high-Mg basalts, and clinopyroxene is present in samples with up to 8.7 wt. % MgO.

Table 2.4 shows the preferred mantle source compositions determined by pHMELTS modeling (GSC dry and wet sources) compared to other modeled DMMs (global averages from McKenzie and O'Nions (1991), Salters and Stracke (2004) and Workman and Hart (2005)). The pHMELTS-determined sources are extreme mantle compositions – both the wet and dry sources are very high in SiO_2 and extremely depleted in incompatible elements. Our models require a very high CaO/Al_2O_3 ratio in the source to approximate the observed liquid lines of descent. Incompatible elements are lower in the model GSC sources than the McKenzie and O'Nions (1991), Workman and Hart (2005) and Salters and Stracke (2004) global average DMMs. Additionally, the pHMELTS Galápagos source is more depleted than the source modeled by Cushman et al. (2004), which uses averages of a more limited selection of oxides to calculate melting extents. The reliability of our modeled source compositions is discussed further in a later section (see Discussion).

2.6 High-Al MORB

We have identified nine samples from seven locations that contain > 16.0 wt. % Al_2O_3 in glass samples with > 8.5 wt. % MgO. Corresponding with this enrichment in Al is a slight enrichment in Na, though there appears to be no significant difference in K from normal low-Al MORB (see Fig. 2.2, 2.3). These samples also appear to have slightly higher Fe contents, and are consistently low in Si and Ca. In this paper, we distinguish those samples with glass compositions of > 16.0 wt. % Al_2O_3, > 8.5 wt. % MgO and < 50.0 wt. % SiO_2 as high-Al GSC N-MORB. In subsequent sections we evaluate two possible processes to account for these unusual compositions. In our modeling treatment, we assume the high-Al rocks are derived from a similar mantle source as the N-MORB from this area of the ridge. The model runs discussed in the following section use our modeled pHMELTS GSC mantle as the source composition.

2*.6.1 Low-F melting models*

Because Al behaves incompatibly during melting, it might be expected that high-Al samples represent low degrees of partial melting. Melting runs with lower entropy values (i.e. cooler mantle) have solidus intersections at shallower depths in the mantle, and proceed to a lower F before accumulating in the crust (Klein and Langmuir, 1987). However, although lowering F for our GSC mantle source does indeed increase primary

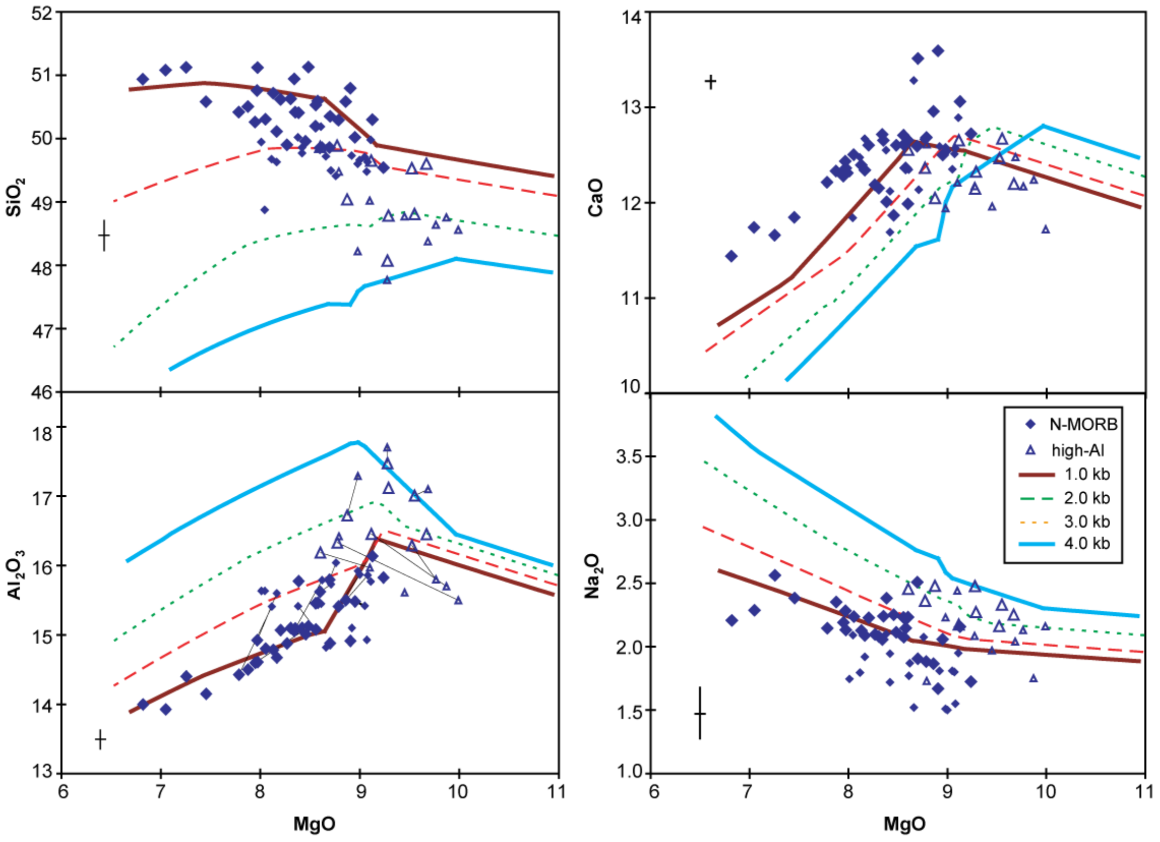

Figure 2.3 Modeling of high-Al samples with dry GSC DMM source and variable crystallization processes. Melting starts at 2.47 GPa and proceeds to a pressure P_F, where the melts are aggregated and cooled. Crystallization runs are isobaric and fractional with an oxygen fugacity of FMQ -2. Tie lines in the Al_2O_3 plot denote glass-whole rock pairs.

magma Al, decreasing F and P_0 also causes an increase in Si (an effect of lower mean pressure of melting as melt Si content is inversely related to pressure of melting (Jaques and Green, 1979)), while the high-Al glasses have lower Si values than low-Al MORB at the same MgO (Fig. 2.2). Alternatively, low F melts can be derived from melting paths with a higher entropy (and correspondingly higher P_0) by extracting melts from deep in the melting region. This process also was modeled, extracting low-F, high-P melts early and then fractionating them at crustal pressures (1-1.5 kb). However, although this process can produce low-Si melts, it fails to produce melts with Al contents as high as required by our data while still matching our other chemical and geophysical constraints (Fig. 2.2). To increase Al enough to produce the very high values in our rocks under normal crustal fractionation, F has to be decreased so extensively that the modeled crustal production suffers such that the source no longer produces nearly enough melt to form the 5.6-6.0 km of crust seen in this area, and other oxide compositions are over-corrected with model trends lying far outside the observed glass chemistry. Thus, our modeling has not found any satisfactory combination of source composition and melting conditions that yield parental magmas that can account for the observed crustal thickness and reproduce high-Al Galápagos N-MORB compositional trends by low-pressure fractionation. Although simple low-F melting scenarios can produce high-Al melts, these models result in crust that is too thin and magmas that have significant chemical misfits in other oxides. We conclude from this exercise that we need to consider alternative fractionation paths.

2.6.2 High-P fractionation models

Although low degrees of partial melting alone cannot explain the high-Al, low-Si chemistry observed in these rocks using this mantle source, we are able to reproduce the compositional variations in our high-Al MORB with models that allow crystallization at pressures up to 0.3-0.4 GPa (Fig. 2.3). At these pressures, the pyroxene phase volume (stability field) is much larger and clinopyroxene can crystallize very early in the fractionation sequence (up to 10.5 wt. % MgO), driving Al values in the residual melt to higher values while keeping Si values low. Melting for these model runs begins at $P_0 =$ 2.47 GPa and follows the same temperature adiabat as the dry (pMELTS) N-MORB model. However, because melting is terminated at higher pressures to allow melt aggregation and crystallization in the upper mantle, the maximum extent of melting for high-Al model runs is inherently lower (F_{max} ~0.16 for $P_F = 4$ kb) than for the N-MORB melting path (F_{max} ~0.19), which allows melting all the way to the base of the lithosphere along the same adiabat. Thus, although low degrees of partial melting alone cannot explain the high-Al chemistry, slightly lower-F melts are built into the high-P crystallization models.

Trace element data on Galápagos high-Al MORB are consistent with evolution involving significant amounts of clinopyroxene crystallization (Fig. 2.4). The high-Al basalts tend to be low in Cr, Sc, and V, all elements that are partitioned preferentially into clinopyroxene (McKenzie and O'Nions, 1991, 1995). In addition, Sr content is significantly higher than in average N-MORB (Fig. 2.4). We modeled selected trace elements for the same two-stage melting and fractionation model described above using

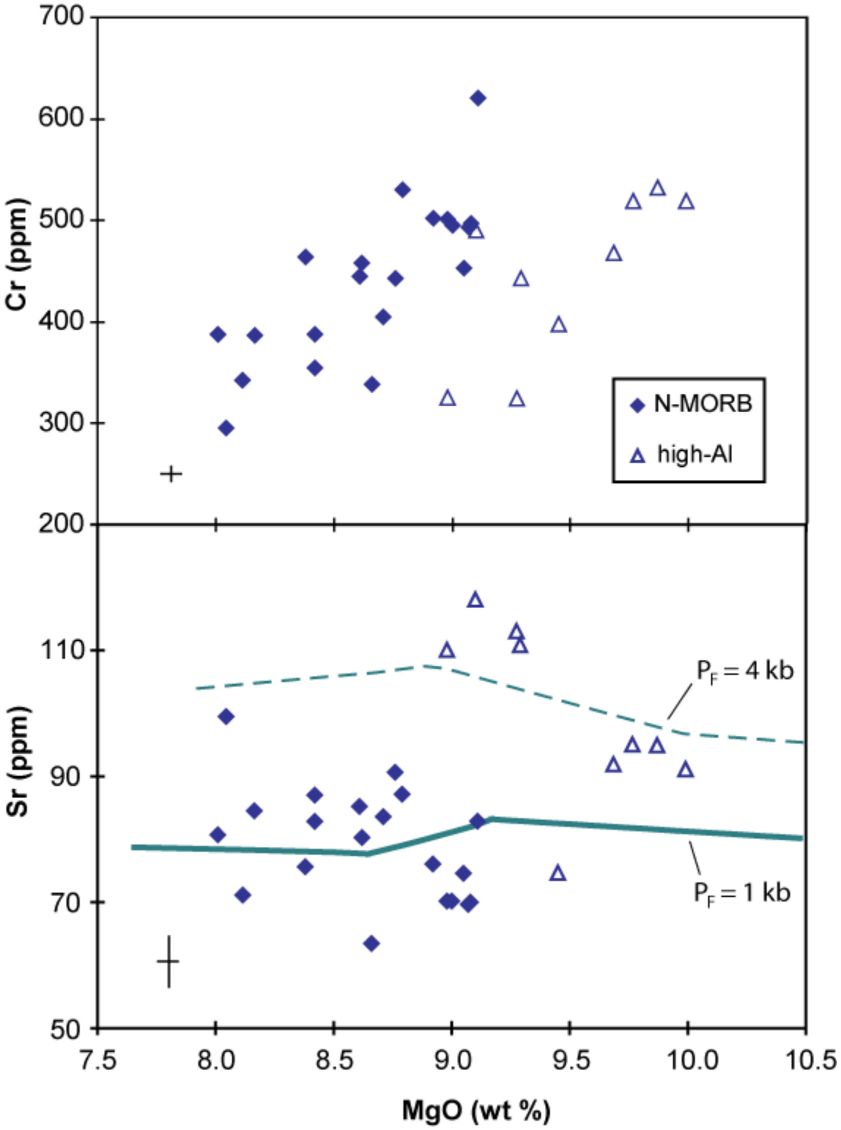

Figure 2.4 Sr and Cr trace element data for N-MORB and high-Al samples data – whole-rock XRF analyses. Error bars denote ±1σ standard deviation of whole-rock analyses (Cr is within symbol size) based on system data reported in Sinton et al. (2005). Sr model runs calculated using constant partition coefficients from McKenzie and O'Nions (1991, 1995) with a source concentration of Sr_0 = 5.4 ppm.

constant partition coefficients from McKenzie and O'Nions (1991, 1995). Although the model runs do not match the data trends exactly, probably owing to inapplicability of the chosen partition coefficient values, it is apparent that the effect of early crystallization of clinopyroxene on Cr, Sc, and V concentrations in the high-Al model runs is in the correct direction. In contrast to these elements, Sr shows a clear separation between the high-Al and normal MORB fractionation paths. High-Al model runs using a crystallization pressure of 4 kb show the ~20 ppm increase in Sr needed to match the high-Al samples, largely an effect of the ~0.03 difference in melt fraction between the two models. The suppression of plagioclase crystallization in the high-Al models help maintain high Sr in the liquid.

The mineralogy produced by these high pressure fractionation runs consists of ~22% olivine (a high value that reflects the high MgO primary melt, an artifact of pMELTS (Ghiorso et al., 2002)), ~5% plagioclase (An 79), and ~7% clinopyroxene at an MgO of 8.9 wt. %. (see Table 2.5 for a direct comparison with a specific sample at similar glass MgO). Although the fractionation of clinopyroxene is integral to matching the chemistry of the glasses in these model runs, there are no clinopyroxene phenocrysts observed in our rocks. Plagioclase is typically more abundant in the samples than predicted by fractionation models (by as much as a factor of two in EW 79-1), and often has a higher An content.

Table 2.5 Mineralogy of fractional crystallization model runs compared with sample analysis. 3kb runs best approximates the glass chemistry of EW 79-1. Model modes represent total fractionated phases.

		pMELTS		*pHMELTS*	
	EW 79-1	**P_F=1 kb**	**P_F=3 kb**	**P_F=1 kb**	**P_F=3 kb**
Liquid					
SiO_2	49.0	50.4	48.6	50.3	48.5
TiO_2	1.01	1.01	1.08	1.02	1.12
Al_2O_3	16.7	15.6	16.8	15.5	16.7
FeO*	9.73	9.20	9.75	9.27	10
MgO	8.87	8.85	8.92	8.89	8.85
CaO	12.0	12.6	12.1	12.7	12.1
Na_2O	2.48	2.04	2.38	1.97	2.37
K_2O	0.04	0.05	0.06	0.05	0.06
P_2O_5	0.07	0.08	0.09	0.07	0.09
H_2O	0.16	0.13	0.13	0.12	0.15
Mineral Mode					
% ol	1.6	24	22	24	22
Fo	86	83	83	83	83
% plag	15.5	5.4	4.2	5.3	5.1
An	82	80	79	80	79
% cpx	--	--	6.4	--	7

2.7 Discussion

2.7.1 GSC Source

As noted previously, the GSC source composition we derive from (pH)MELTS modeling is extremely depleted in incompatible elements and 2-3 wt. % higher in SiO_2 than WH and MO (Table 2.4). The high SiO_2 value is required by the (pH)MELTS algorithms to approximate GSC N-MORB SiO_2 content with sufficient melting to create the observed crustal thickness. As P_0 deepens to create sufficient melting, SiO_2 in the resulting melts tends to decrease as a result of the higher pressure, requiring higher values of SiO_2 in the source to compensate and reproduce the observed chemistry. The (pH)MELTS models also require very high CaO/Al_2O_3 in the source (~0.86) to approximate the observed liquid lines of descent for these oxides. This composition requires a large amount of orthopyroxene in the source (>40%) at the expense of olivine and clinopyroxene. Although it might be possible for the mantle in this region to contain local horizons that are anomalously rich in pyroxene, we suspect that the derived GSC source composition could be either an artifact of the (pH)MELTS calculations, or of assumptions about the melting processes that are inherent in these calculations.

The extreme depletion of our modeled GSC source composition is in part an artifact of (pH)MELTS calculations. Testing of the (pH)MELTS algorithms against MORB experimental data has revealed a number of discrepancies. Calculated liquid MgO is too high (Ghiorso et al., 2002), which accounts for the high value of our primary magma (17.9 wt. %). Na is known to be too incompatible in MELTS calculations, in which the multiple saturation slope is too steep, causing it to be high in calculated liquid compositions (Hirschmann et al., 1998). The high MgO content of the primary magma results in substantial fractionation and a potentially large error in Na, meaning the source must be artificially low to compensate.

In addition, certain assumptions about the melting process may contribute to the extreme values we need for our source. Our model assumes perfect passive flow in which all melts are integrated to produce the crust. Any dynamical effects would decrease the concentration of incompatible elements in the aggregated melts by excluding some of the lowest F melts from the corners of the melt regime. Any amount of active upwelling would decrease the amount of source depletion required to reproduce the low K, Ti, and P values of the sample glasses, and Si in the source would decrease to more reasonable values (a consequence of normalizing with increased incompatibles as well as the effect of needing higher pressures to produce the given amount of melt needed). As a comparison, an end-member active upwelling model using pHMELTS in which all streamlines are the height of the full (1-D) melting column gives us a source with approximately 42 wt. % SiO_2, 2.7 wt. % Al_2O_3 and 0.27 wt. % Na_2O for our crustal thickness. Although pure active upwelling also is unlikely to be realistic for our ridge setting, some component of dynamic flow could help explain our relatively depleted N-MORB samples. As has been noted by Asimow et al. (2001), MELTS is unable to produce average MORB crust with the K_2O/TiO_2 ratios seen in depleted MORB (<0.09) with any reasonable amount of K_2O in the source. Considerations of dynamical effects that exclude some of the lower F melts from the aggregate seem to be required in order to successfully model depleted MORB.

There are additional process assumptions inherent in the thermodynamic calculations of MELTS and p(H)MELTS (see Ghiorso and Sack (1995), Ghiorso et al. (2002) for further explanation of these algorithms). Perhaps most significantly, p(H)MELTS assumes the system is closed during melt migration, such that no mixing or contamination occurs as the melt rises through the mantle. Although there is good evidence that melt migration is not a closed system process (e.g., (Keleman et al., 1997; Niu, 1997)), we have not considered the consequences of reactive flow processes in our modeling. We do not have textural evidence for any disequilibrium processes or mineral assimilation, and we are able to explain the observed chemistry without invoking such processes.

An additional assumption in our model is that melting continues all the way to the base of the crust. Recent studies indicate melting may actually stop at some distance below the Moho (Niu and Batiza, 1991; Shen and Forsyth, 1995; White et al., 2001). Melting accompanies mantle upwelling until the mantle reaches the thermal boundary layer which defines the final melting pressure (P_f). This boundary is primarily controlled by the conductive thermal gradient, which Niu (1997) and Niu and Hékinian (1997) argue to be spreading rate dependent. Because a precise determination of P_f is currently unconstrained, we chose to model N-MORB melting using the assumption of earlier MORB genesis models that melting continues to the Moho rather than pick an equally arbitrary P_f at some depth below. If melting terminates at a higher P_f, the solidus intersection at P_0 would also need to be deeper to maintain high enough melt fractions to match crustal production and some adjustments of source chemistry would be necessary (higher SiO_2, possibly lower FeO*). Finally, our assumed melt productivity is susceptible to uncertainties in the crustal thickness estimate from multichannel seismic reflection and seafloor refraction data (Canales et al., 2002; Detrick et al., 2002).

Although our modeled source is unlikely to be a realistic composition for the bulk mantle below this part of the GSC, we are unable to separate the relative contributions from partitioning errors in the MELTS models from the uncertainty in the melting process. Nevertheless, GSC N-MORB are depleted in incompatible elements relative to global average MORB. Since the crustal thickness in this area is close to (or below) average, the qualitative result of the MELTS modeling that we have a depleted source is probably valid. Such depletion could arise from prior melting beneath the East Pacific Rise coupled to an eastwardly flowing asthenosphere (Bostrom, 1997; Ricard et al., 1991; Doglioni et al., 2003) as previously invoked to explain the abundance of highly depleted lavas from Hole 504B (Autio and Rhodes, 1983) and the relative dearth of T-MORB along the GSC compared to the Southern East Pacific Rise (SEPR) (Sinton et al., 1991).

Given the uncertainties in asthenospheric flow patterns and the lack of comparable studies of crustal thickness and mantle melting along the SEPR, the origin and extent of western GSC major element source depletion remains equivocal. Nevertheless, despite uncertainties in our source composition modeling, the process assumptions and MELTS uncertainties are internally consistent in our comparison between the high-Al, low-Si samples we find near ridge segment terminations, and normal Galápagos MORB.

2.7.2 High-Al MORB

Clinopyroxene crystallization is integral to creating the high-Al, low-Si signatures seen in the GSC samples. Once melts pass out of the adiabatic upwelling and melting regime and into the region of conductive cooling, they will begin to crystallize minerals on the liquidus. Normally this process occurs at low pressure for mid-ocean ridges where the olivine phase volume (stability field) is large, leading to the olivine ± plagioclase crystallization recognized in MORB chemical signatures and excess olivine content in abyssal peridotites sampled at mid-ocean ridges (Niu, 1997). However, at higher pressures corresponding to depths modeled for GSC high-Al MORB, clinopyroxene precedes plagioclase in joining olivine as a crystallizing phase. Because these mineral phases are largely not seen in the GSC samples (only 1-2% olivine in the rocks vs. the 8% fractionated, and no clinopyroxene phenocrysts present), we suppose that these mineral phases are left behind (possibly as wehrlitic horizons) as the melt continues migrating towards the surface. Upper mantle crystallization involving olivine and clinopyroxene ± spinel is well known in the shallow mantle sections of many ophiolites (e.g., (Sinton, 1978; Keleman et al., 1995)). Our models predict crystallization beginning as deep as 4 kb, or as much as 6-10 km below the Moho, which is somewhat deeper than currently recognized in the best documented ophiolites (Keleman et al., 1997).

Many models of MORB paragenesis require early, cryptic crystallization of clinopyroxene and this problem has been widely referred to as the "pyroxene paradox", wherein rock chemistry requires clinopyroxene fractionation at some stage in its evolution, but the mineral is absent in the lavas and unstable in the liquids at low pressures (e.g., Dungan and Rhodes, 1978; Francis, 1980; Elthon et al., 1995). Among the various explanations for the pyroxene paradox (see Sinton and Detrick (1992) for a review) is high-pressure crystallization during or prior to magma ascent and either dissolution or segregation of clinopyroxene during low pressure olivine + plagioclase crystallization (e.g., Elthon et al., 1980; Thompson et al., 1980; Grove et al., 1992).

The GSC high-Al samples are not unique in requiring upper mantle partial crystallization to explain chemical characteristics. Gabbros, megacrysts and cumulate phases believed to be derived from upper mantle fractionation have been found at slow spreading ridges and fracture zones (Elthon et al., 1982; Stakes et al., 1984; Elthon, 1987). Other petrological evidence from MORB geochemistry suggests that partial crystallization occurs in the mantle as well as the crust (Tormey et al., 1987; Grove et al., 1992; Kinzler and Grove, 1992; Elthon et al., 1995; Dmitriev, 1998; Michael and Cornell, 1998; Meurer et al., 2001; Herzberg, 2004).

Our model shows that Galápagos high-Al MORB can be derived from the same mantle source as the GSC N-MORB without requiring source heterogeneity. Because Galápagos high-Al MORB do not exhibit any K or Ti enrichment, an added component enriched only in Al seems unlikely. As mentioned previously, there are additional processes that can increase glass Al content that must be considered. Wet melting experiments have yielded plagioclase-rich, high-Al basalts (Beard and Lofgren, 1992), and water is known to play a role in the formation of high-Al calc-alkaline rocks (Sisson and Grove, 1993). However, the low water content in GSC N-MORB (Cushman et al., 2004) makes this an unlikely alternative, and GSC high-Al samples that have been analyzed for water have the same low H_2O contents (0.14-0.16 wt. %) as normal low-Al

N-MORB at the same MgO. Plagioclase assimilation is an alternative process that can increase the aluminum content in magmas (Flower, 1980; Danyushevsky et al., 2003). However, we see no textural evidence for mineral assimilation, and the high-Al signature appears in both glass and whole-rock data, with the exception of two sites: the nearly aphyric EW-71 (samples a and b) and ALV-1554, for which whole-rock data have low Al, despite corresponding low Si and Ca, and higher Na (other signatures of early fractionation). A comparison of the glass and whole-rock data for these samples indicates they may not have undergone any significant plagioclase or clinopyroxene fractionation – glass-rock tie-lines appear to outline an olivine-only fractionation vector (Fig. 2.3). Thus, although these samples exhibit at least some of the characteristics of the more extreme high-Al N-MORB, high pressure evolution is not required. Along the GSC those samples that appear to require significant high pressure fractionation may be restricted to those with > 16.5 wt. % Al_2O_3.

It is important to note that our fractional crystallization runs are isobaric and assume melt congregates and fractionates at a single depth. In fact, crystallization may be polybaric, proceeding en route while the melt is migrating upwards to the crust, or multi-stage, with high-pressure fractionation followed by low-pressure crustal fractionation. While the high-pressure crystallization may occur in upper mantle magma chambers, this is certainly not required by the data. Polybaric or multistage fractionation modeling would require initial crystallization at higher pressures than our isobaric model to achieve the same glass composition: by crystallizing first at higher pressures (ol+cpx), liquids can achieve higher Al_2O_3 contents at higher MgO, then crystallize at low pressure (ol+plag), decreasing both Al_2O_3 and MgO to reach their target melt composition.

Because crystallization begins at higher MgO contents for these models, more crystallization occurs overall, perhaps explaining why we find larger amounts of plagioclase in some of these samples than the isobaric model mode predicts (Table 2.5). Because adding a low-pressure crystallization stage into the model requires that we initiate crystallization at higher pressure, our isobaric pressure estimates for the onset of crystallization are likely minimum values. Glass-whole-rock tie-lines of the highest Al samples seem to support this, delineating fractionation vectors from even higher Al_2O_3 values than our 4 kb model runs are able to obtain (Fig. 2.3).

2.7.3 Global Distribution

The global distribution of MORB with > 16.0 wt. % Al_2O_3 and > 8.5. wt. % MgO (Fig. 2.1) indicates that they occur preferentially at ridges with slow to intermediate spreading rates and at the ends of ridge segments. Along the western GSC, these samples are restricted to the ends of (possibly dying) ridge segments near the 95.5°W propagator (see Fig. 2.1). We have not found high-Al and N-MORB occurring within single dredge sites.

Slow-spreading ridges and ridge segment terminations are areas where steady-state magma chambers are unlikely to be present (Sinton and Detrick, 1992). Conductive cooling to the surface also has a greater effect on the mantle temperature profile in these regions than at fast-spreading ridges due to slower upwelling. Consequently, melting might stop at significantly deeper levels beneath slow-spreading ridges and fracture zones than at fast-spreading ridges, where the conductive thermal gradient has less of an effect against the adiabat (convective gradient) (Bottinga and Allègre, 1978; Reid and Jackson, 1981; Niu and Hékinian, 1997). High-pressure fractionation is enhanced by conductive cooling in these regions, causing clinopyroxene and olivine to fractionate in the upper mantle. This is consistent with the findings of Michael & Cornell (1998), who found partial crystallization pressures were correlated with spreading rate, and Dmitriev (1998), who associated high pressures of partial crystallization with ridge terminations (including fracture zones, overlapping spreading centers, and devals). Herzberg (2004) modeled partial crystallization in the mantle based on An-Di-En projections and found the same correlation between ridge setting and high pressure MORB crystallization. Application of his petrological model to GSC MORB data gives crystallization pressures ranging from 0.48–0.85 GPa for the high-Al samples, compared with an average of 0.14 GPa for normal low-Al GSC N-MORB (written comm., 2005) – a factor of 2 greater than the pressures estimated by our isobaric fractionation modeling but probably within the range of errors associated with the two approaches. As noted in the previous section, our crystallization pressures are likely minima, and non-isobaric crystallization may require deeper solidus intersections to achieve the high-Al, low-Si signature characteristic of fractionation in the upper mantle.

2.8 Summary

Forward modeling of Galápagos Spreading Center N-MORB using (pH)MELTS requires a highly depleted peridotite mantle source with a maximum melt fraction of ~0.19 and a potential temperature of ~1430°C. When aggregated and cooled in the shallow crust (1 kb), these melts follow fractional crystallization paths that approximate our N-MORB glass compositions. The rather extreme mantle source required by this model is partly a result of errors in the MELTS thermodynamic calculations exacerbated by the process assumptions of perfect passive flow and complete melt focusing. The results of this exercise illustrate some of the limitations of quantitative thermodynamic modeling without a corresponding flow model.

Several high-Mg GSC glass samples contain unusually high concentrations of Al, along with low Si and abundant plagioclase phenocrysts. Although high-Al contents can be obtained by very low extents of partial melting, low-F models result in significant misfits in other major element oxides and do not explain the sample chemistry. Instead, we require high-pressure fractional crystallization of clinopyroxene at pressures of 0.3-0.4 GPa to explain major element compositions of these samples. Although clinopyroxene is not present as a phenocryst phase in these samples, trace element data are qualitatively consistent with clinopyroxene fractionation. Crystallization in the upper mantle is consistent with other recent models correlating high-pressure crystallization with slow spreading ridges and ridge segment terminations. High-pressure crystallization is enhanced by conductive cooling in these regions, causing olivine and clinopyroxene to fractionate in the upper mantle.

Acknowledgments

We thank the shipboard scientific party and crew of R/V *Maurice Ewing* Leg EW00-04 for their help in the data and sample acquisition, and the Ecuadorian government and the Parque Nacional Galápagos for permission to work in their waters. We also thank John Mahoney and David Graham for expert dredging, Kent Ross for assistance with the microprobe and XRF analyses, Buffy Cushman for glass data collection, Chuck Fraley for help with the whole-rock analyses, and JoAnn Sinton for thin section preparation. Discussions with Julia Hammer, Kevin Johnson and Rhea Workman have helped clarify many of the ideas in this paper. This research was supported by the National Science Foundation grants OCE03-27051 and OCE05-24922.

CHAPTER 3

LAVA SHIELDS AND FISSURE ERUPTIONS OF THE WESTERN VOLCANIC ZONE, ICELAND: EVIDENCE FOR MAGMA CHAMBERS AND CRUSTAL INTERACTION

3.1 Abstract

Volcanic eruptions in Iceland occur either from fissures or central vents (lava shields). Within the post-glacial Western Volcanic Zone, the Thjófahraun fissure-fed lava field and Lambahraun lava shield were both erupted ~4000 yrs B.P. with eruptive centers separated by only ~25 km. Thjófahraun erupted ~1 km^3 of pāhoehoe and ‘a‘ā lava from a 9-km long fissure, whereas the Lambahraun lava shield erupted >7 km^3 of low effusion-rate pāhoehoe. Thjófahraun lavas contain higher K, Rb, Y and Zr, and lower CaO than Lambahraun lavas at the same MgO, with variations broadly consistent with evolution by low-pressure crystal fractionation. Lambahraun spans a larger range of MgO, which generally decreases over time during the eruption. Lambahraun samples with high Al_2O_3 and low TiO_2 and FeO likely reflect up to 15 % plagioclase accumulation. In addition, all samples from Lambahraun exhibit increasing CaO and Nb/Zr with decreasing MgO and overall incompatible-element enrichments greater than predicted by crystal fractionation alone. Although the increase in Nb/Zr and other incompatible elements could be explained by gradually more incompatible-element enriched parental magma being supplied to the magmatic system during the course of the Lambahraun eruption, this process requires very small-scale trace element heterogeneities in the mantle that are apparently decoupled from isotopic variations and a systematic

relationship between parental magma composition and extent of differentiation. Alternatively, correlations among incompatible element concentration, increasing differentiation and time during the eruption can be related by concurrent wallrock assimilation and crystallization during melt migration through the crust. Geochemical modeling of assimilation of wallrock clinopyroxene concurrent with crystallization of olivine (± plagioclase) effectively reproduces the observed chemical variations of Lambahraun samples. Similar chemical characteristics exist in several other Western Volcanic Zone lava shields but not in fissure eruptions. Magmas that fed fissure eruptions may also have been modified by interaction with the crust prior to aggregation in crustal magma chambers, but the geochemical signature of this process is obscured by magma mixing. In contrast, Icelandic lava shields that preserve deeper level processes may not have developed shallow magma chambers; rather they probably represent slow effusion from magma systems that are continually being recharged and reacting with the crust during the course of their eruptions.

3.2 Introduction

The study of the products of single volcanic eruptions is one of the most direct ways to assess the nature of underlying magmatic processes that occur prior to and during eruptions. Erupted volumes and chemical composition of individual lava flows constrain the size, temperature, and internal variation within sub-volcanic magma reservoirs, which in turn can affect the style of eruption. The nature and extent of chemical heterogeneity within individual eruptive episodes can be used to constrain melting, differentiation and mixing that must occur over time scales limited by eruption durations and periods between eruptions at specific locations. Among the questions that can be addressed by such studies include magmatic controls on eruption rate, resultant lava morphology, and the nature of magma chambers, if any, from which the magma is erupted.

To fully address relationships among melting and differentiation processes of individual eruptions and their corresponding eruptive style, magma supply, and crustal storage characteristics requires information on flow morphology, eruptive vent characteristics, estimates of erupted volume, and sufficient sampling to quantify chemical heterogeneity. The highest level of detail for volcanic eruptions can only be attained for historical events with contemporaneous observations and sampling. For pre-historical eruptions, detailed mapping and sampling is especially difficult to accomplish along submarine mid-ocean ridges and consequently, studies at the scale of individual mid-ocean ridge eruption units are rare (Perfit and Chadwick, 1998; Embley et al., 2000; Sinton et al., 2002; Bergmanis et al., 2007). Even in Iceland, where the mid-ocean ridge system is well exposed above sea level, there have been relatively few detailed studies of single lava flow fields (Maclennan et al., 2003b) and no lava shields have erupted in historical time.

The neovolcanic zones of Iceland are ideal for investigating processes associated with individual eruptive units. The very slow-spreading (3-7 mm/yr (LaFemina et al., 2005)) Western Volcanic Zone (WVZ) forms a 170-km long portion of the Mid-Atlantic Ridge plate boundary, comprising the western limb of a microplate in South Iceland (Fig. 3.1). All post-glacial (since ~12 ka) eruptive units of the WVZ have been mapped, sampled and analyzed for major and trace elements, and age constraints have been determined for most eruptions from ^{14}C-dating and tephrochronology (Sinton et al.,

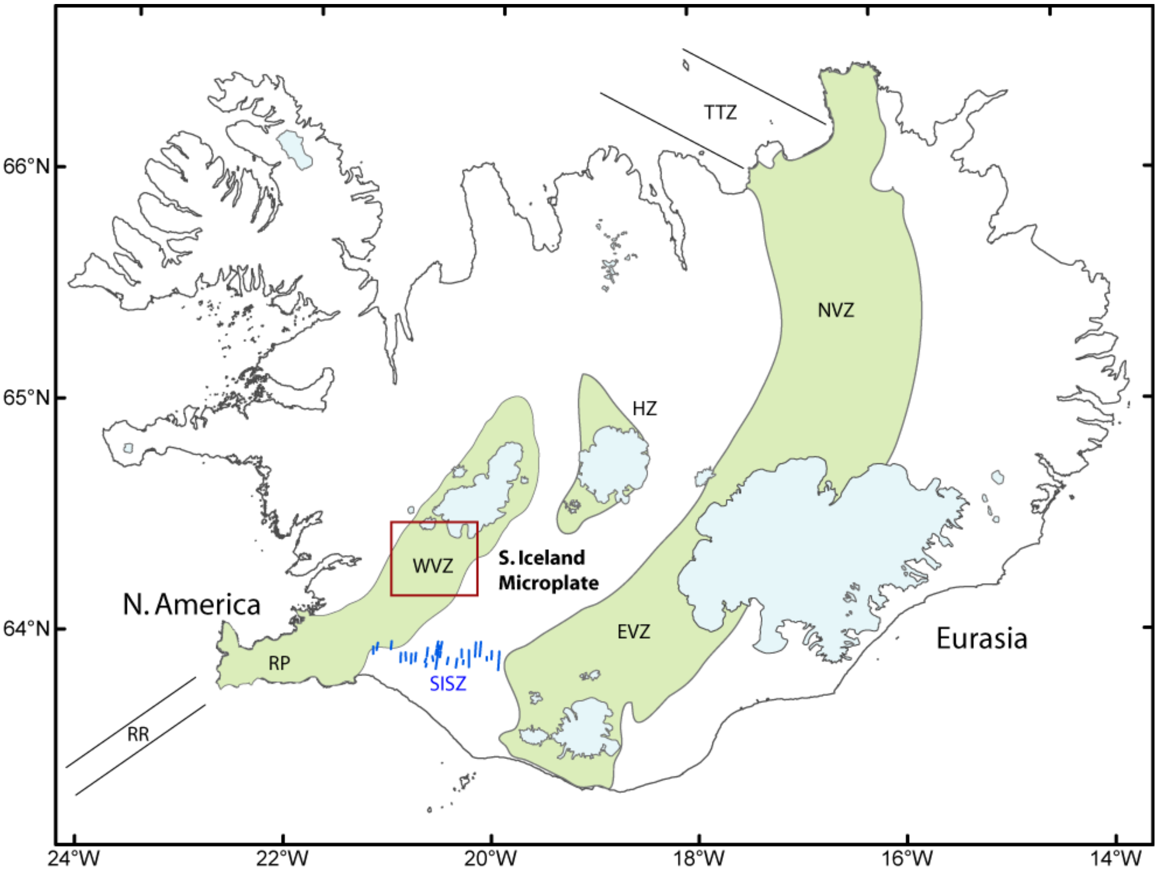

Figure 3.1 Map of Iceland showing the principal plate-boundary zones in Iceland: the Northern Volcanic Zone (NVZ), Eastern Volcanic Zone (EVZ), Hofsjökull Zone (HZ), Western Volcanic Zone (WVZ), and Reykjanes Peninsula (RP). These volcanic zones connect up to the Tjörnes Transform Zone (TTZ) and Reykjanes Ridge (RR) offshore. The south Iceland seismic zone (SISZ) represents a transform boundary on the south side of the south Iceland microplate. Box outlines the area of Figure 2.

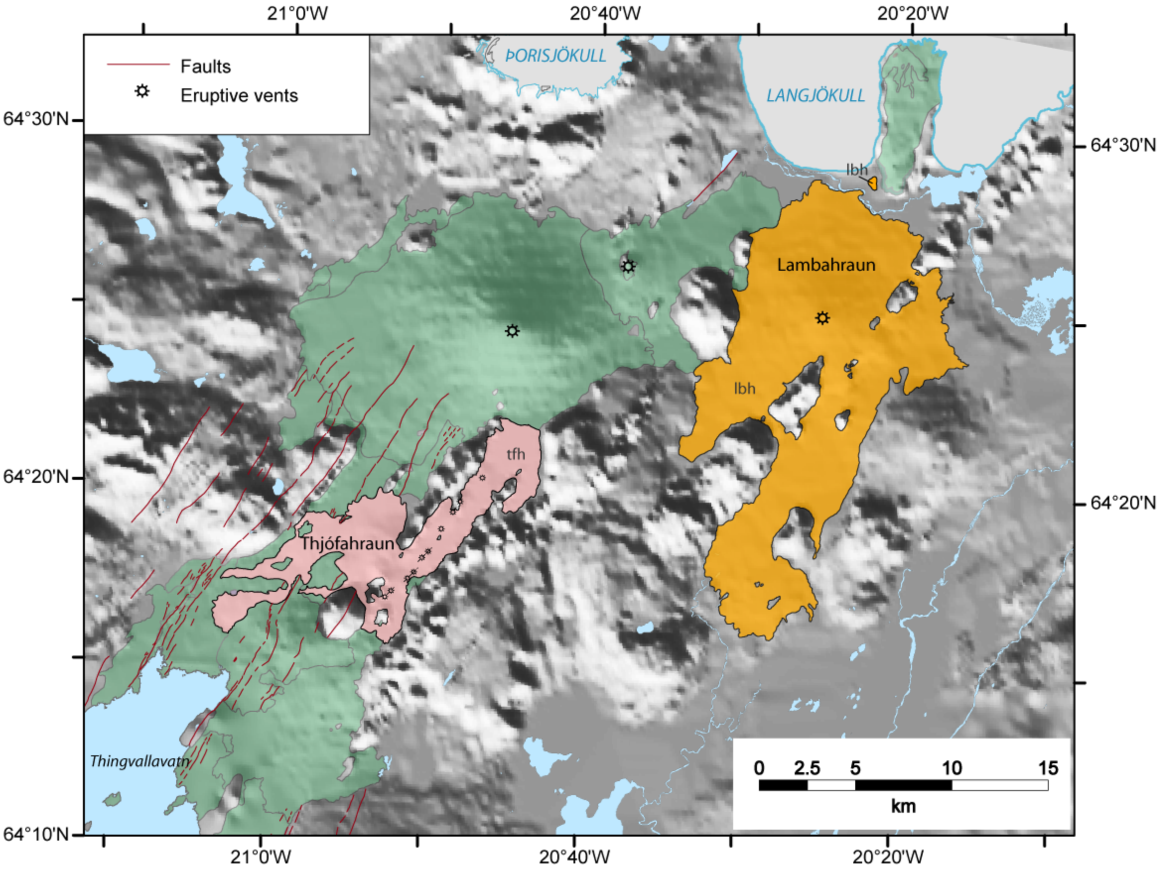

Figure 3.2 Shaded relief map of the central Western Volcanic Zone showing the distribution of postglacial lava units, including Lambahraun (lbh) and Thjófahraun (tfh). Modified after Sæmundsson (1992) and Sinton et al. (2005).

2005). Sr, Nd, Pb and Hf isotopic ratios have been determined for a subset of samples (Halldórsson et al., 2008b). Lava flow fields produced during single eruptive episodes range from ~0.1 to >15 km^3, encompassing a range in lava morphology and styles of eruptive activity. Thus, this portion of the ridge is an ideal location to investigate a variety of volcanic processes, including spatial and temporal variations in eruption style, melting and differentiation processes, and source heterogeneity.

Volcanic eruptions in Iceland occur either as fissure or central vent (lava shield) eruptions. Fissure eruptions tend to produce lavas indicative of high average effusion rates from small spatter cones extending over several kilometers to tens of kilometers. In contrast, most lava shields are composed almost entirely of relatively dense pāhoehoe lava from edifices that are surmounted by a central caldera, typically 0.5-2 km in diameter. However, the nature of the reservoirs that feed these eruptions and the underlying magmatic processes that occur prior to eruption are poorly known. Sinton et al. (2005) proposed that fissure eruptions tap extant, well-mixed crustal magma chambers, whereas the chemical variations in lava shields are inconsistent with large, well-mixed magma reservoirs and seem to require mantle recharge during the course of several decade-long eruptions. In order to better understand the underlying magmatic processes associated with differences in eruptive style, we have undertaken a detailed study of the products of two WVZ eruptions – a lava shield (Lambahraun) and a fissure eruption (Thjófahraun) – both erupted about 4000 yrs ago with the locus of activity separated by about 25 km (Fig. 3.2). The selection of two units erupted close to one another in both space and time along the WVZ minimizes temporal and spatial variations in processes related to mantle composition and crustal structure. We use the geochemical variability of the erupted products of Lambahraun and Thjófahraun to constrain the differences in their respective crustal reservoirs, their melting and differentiation histories, and potential source variations. The selection of Thjófahraun and Lambahraun requires that any spatial or temporal variations must be less than ~25 km and ~400 years.

3.3 Data and methods

3.3.1 Field Study

The areal limits of both Lambahraun and Thjófahraun flow fields and internal contacts within the Thjófahraun field were determined using a combination of aerial photographs and field mapping; the external contacts shown in Figs. 3.2-3.4 are modified slightly from those of Sinton et al. (2005). Sub-units within the Thjófahraun field and their relative ages were determined from aerial photographs and field observations. Where possible, we attempted to assign individual flow units to the vents from which they were erupted, although this is typically only possible for the youngest units. Sixteen additional samples collected for this study from both units supplement the 33 analyses reported by Sinton et al. (2005) to better cover the spatial range of each flow field.

3.3.2 XRF Analysis

Whole rock x-ray fluorescence (XRF) data were measured on the University of Hawai‘i Siemens 303AS XRF spectrometer using a Rh-target, end-window x-ray tube. Whole rocks were crushed in an alumina swing mill, and powders were analyzed for major elements on fused disks following methods similar to those of Norrish and Hutton

(1977). Trace elements were analyzed on pressed powder pellets. Peak intensities for the trace elements were corrected for backgrounds, line interferences and matrix absorption using methods similar to those of Chappell (1992). Corrected intensities were calibrated against a wide range of natural rock standards. Accuracy and precision data for this system are reported in Sinton et al. (2005). New analytical data are reported in Table 3.1. Additional analytical data from Lambahraun and Thjófahraun published in Sinton et al. (2005).

3.3.3 ICP-MS Analysis

Low-abundance trace elements were analyzed in selected samples by inductively-coupled, plasma mass spectrometry (ICP-MS) using the University of Hawai‘i VG PlasmaQuad instrument. Clean rock chips were crushed in alumina, from which 0.1200 gms were digested in a mixture of HNO_3, HCl and HF in sealed teflon CEM digestion vessels, using a microwave digestion oven at 90 psi. After digestion, the vessels were uncapped and heated to evaporate the solutions to near dryness, which were then diluted to ~100 grams with 2% ultra-clean, distilled HNO_3. The solutions were stored in acid-cleaned plastic bottles until analyzed. Prior to analysis, samples were diluted 1:10 in 2% HNO_3. A mixed internal standard solution of Zn 67, In 115, and Bi 209, diluted to 1.0, 2.5, 5.0, and 10.0 ppb, in 2% HNO_3 was run along with each sample for instrument calibration. Samples were calibrated against international rock standards JB-3, NIM-N, JB-2, JGb-1 (Table 3.2).

Table 3.1 Whole-rock XRF analyses.

Unit	**Lambahraun**					
Samp. no.	**IT-390**	**IT-476**	**IT-477**	**IT-479**	**IT-483**	**IT-485**
easting	0527548	0522666	0524173	0525844	0529247	0530936
northing	7150977	7137528	7139409	7140971	7142661	7141047
SiO_2	48.80	47.40	48.15	48.18	48.54	49.03
TiO_2	2.13	1.85	1.86	1.61	1.75	1.86
Al_2O_3	13.98	15.14	14.97	16.41	15.99	15.91
FeO*	13.08	12.37	12.28	11.12	11.57	11.74
MnO	0.20	0.20	0.20	0.18	0.19	0.20
MgO	6.86	9.68	7.79	7.70	7.04	6.76
CaO	12.64	11.53	12.41	12.62	12.80	12.95
Na_2O	2.06	1.89	1.96	1.88	1.82	1.99
K_2O	0.21	0.16	0.18	0.17	0.17	0.18
P_2O_5	0.26	0.19	0.22	0.20	0.21	0.22
Sum	100.24	100.41	100.01	100.08	100.09	100.85
Sc	50	41	42	38	39	41
V	404	323	351	296	326	343
Cr	309	386	330	331	308	322
Co	46	55	50	45	43	42
Ni	64	176	108	114	90	76
Cu	--	102	--	--	--	--
Zn	108	104	102	83	91	93
Rb	3.8	3.3	3.3	3.1	3.3	3.1
Sr	195	198	193	208	204	203
Y	31	24	27	23	25	26
Zr	119	84	99	91	96	101
Nb	15.0	10.0	12.9	11.7	12.7	12.8
Ba	38	36	33	41	37	42

Table 3.1 (Continued) Whole-rock XRF analyses.

Unit			**Lambahraun**		
Samp. no.	**IT-486**	**IT-487**	**IT-488**	**IT-490**	**IT-492**
easting	0533027	0525108	0523195	0529601	0530315
northing	7141556	7129769	7130099	7135985	7138932
SiO_2	48.78	48.17	47.60	47.99	48.88
TiO_2	1.62	1.88	1.89	1.66	2.28
Al_2O_3	17.06	15.14	15.05	15.70	13.84
FeO*	10.63	12.31	12.43	11.71	13.52
MnO	0.18	0.20	0.20	0.20	0.22
MgO	6.72	8.58	8.56	8.29	6.62
CaO	13.27	12.00	11.95	12.33	12.51
Na_2O	1.86	1.90	1.89	1.73	2.08
K_2O	0.16	0.17	0.17	0.13	0.21
P_2O_5	0.20	0.18	0.19	0.16	0.27
Sum	100.50	100.55	99.95	99.91	100.44
Sc	39	43	39	43	48
V	309	330	334	351	391
Cr	380	297	306	315	282
Co	41	47	47	50	46
Ni	84	121	124	129	64
Cu	--	109	106	--	--
Zn	83	99	98	101	109
Rb	2.9	3.3	3.2	3.3	3.5
Sr	208	189	191	187	202
Y	23	27	27	26	33
Zr	86	91	92	91	120
Nb	10.8	11.2	11.2	10.8	15.7
Ba	32	35	46	30	50

Table 3.1 (Continued) Whole-rock XRF analyses.

Unit			**Thjófahraun**		
Samp. no.	**IT-13**	**IT-53**	**IT-137**	**IT-278**	**IT-473**
easting	0505300	0506340	0507290	0506190	0508819
northing	7128150	7128665	7130275	7133885	7132715
SiO_2	48.41	48.41	49.26	48.51	49.03
TiO_2	1.87	1.73	1.91	1.77	1.78
Al_2O_3	14.94	15.46	15.47	15.07	15.46
FeO*	12.26	11.73	11.82	12.05	12.15
MnO	0.20	0.19	0.19	0.19	0.18
MgO	8.00	8.46	7.34	8.33	8.39
CaO	11.94	11.96	11.99	11.92	11.49
Na_2O	1.99	2.09	2.19	2.06	1.48
K_2O	0.23	0.21	0.24	0.23	0.18
P_2O_5	0.23	0.17	0.21	0.21	0.21
Sum	100.08	100.42	100.63	100.33	100.36
Sc	40	42	43	41	39
V	352	336	378	350	336
Cr	352	404	336	389	365
Co	46	51	45	51	49
Ni	122	157	107	140	160
Cu	--	--	--	--	--
Zn	98	100	102	102	99
Rb	4.6	3.9	4.8	4.4	4.0
Sr	190	185	203	193	200
Y	28	25	28	27	25
Zr	106	92	115	103	107
Nb	12.5	10.1	13.5	12.3	12.3
Ba	50	42	53	38	45

Oxide abundances in wt. %, trace elements in ppm. FeO* = total Fe expressed as FeO.

Sample locations are given in WGS84 UTM coordinates.

Table 3.2 ICP-MS standards data.

		JGb-1			**JB-3**			**JB-2**	
n	*6*	σ	value	*3*	σ	value	*3*	σ	value
Ba	61	2.19	63	223	12.08	245	208	9.26	208
La	3.50	0.09	3.6	8.48	0.17	8.85	2.34	0.06	2.36
Ce	8.48	0.27	8	21.16	0.42	21.5	6.62	0.13	6.77
Pr	1.20	0.05	1.14	3.38	0.17	3.39	1.21	0.04	0.99
Nd	5.27	0.19	5.56	15.41	0.39	15.4	6.20	0.05	6.65
Sm	1.44	0.08	1.49	4.15	0.05	4.27	2.24	0.01	2.25
Eu	0.66	0.03	0.63	1.37	0.03	1.31	0.86	0.01	0.86
Gd	1.66	0.06	1.63	4.71	0.23	4.57	3.31	0.10	3.28
Tb	0.27	0.02	0.3	0.75	0.04	0.74	0.58	0.01	0.62
Dy	1.74	0.07	1.55	4.60	0.22	4.55	4.01	0.11	3.7
Ho	0.36	0.02	0.33	0.94	0.05	0.8	0.88	0.04	0.81
Er	0.99	0.05	1.06	2.63	0.14	2.61	2.57	0.11	2.62
Tm	0.14	0.01	0.15	0.38	0.03	0.41	0.37	0.01	0.43
Yb	0.92	0.04	1.02	2.45	0.09	2.62	2.52	0.10	2.51
Lu	0.14	0.01	0.15	0.37	0.03	0.39	0.39	0.02	0.39

		NIM-N		**B-THO**		**BIR-1**
n	*4*	σ	value	*3*	σ	value
Ba	78.6	2.56	84	6.2	0.31	7.14
La	2.81	0.04	3	0.68	0.01	0.62
Ce	5.81	0.04	5.8	1.90	0.09	1.92
Pr	0.77	0.04	0.71	0.38	0.01	0.37
Nd	3.17	0.10	3	2.30	0.12	2.38
Sm	0.82	0.03	0.8	1.04	0.05	1.12
Eu	0.61	0.02	0.63	0.53	0.03	0.53
Gd	1.00	0.05	0.97	1.73	0.07	1.87
Tb	0.16	0.01	0.16	0.33	0.01	0.36
Dy	1.05	0.05	1.04	2.41	0.09	2.51
Ho	0.22	0.02	0.2	0.53	0.01	0.56
Er	0.64	0.03	0.66	1.56	0.05	1.66
Tm	0.09	0.00	0.1	0.23	0.01	0.25
Yb	0.63	0.02	0.67	1.54	0.06	1.65
Lu	0.10	0.01	0.1	0.23	0.01	0.25

Standard analyses given with number of runs (*n*) and standard deviation (σ). B-THO is a re-collected sample from the same locality as BIR-1.

Table 3.3 ICP-MS analyses.

Unit			**Thjófahraun**			
Sample no.	**IT-35**	**IT-35**	**IT-35**	**IT-133**	**IT-144a**	**IT-144a**
Ba	56.6	58.1	59.2	53.5	58.8	57.7
La	8.42	8.65	8.76	8.04	9.53	9.38
Ce	21.1	22.0	22.2	19.9	23.2	22.8
Pr	3.03	3.12	3.18	2.86	3.44	3.39
Nd	13.6	14.1	14.2	12.9	15.0	14.6
Sm	3.76	3.88	3.91	3.51	4.20	4.17
Eu	1.41	1.46	1.50	1.33	1.59	1.53
Gd	4.27	4.35	4.45	4.16	4.92	4.75
Tb	0.71	0.75	0.76	0.69	0.85	0.83
Gd	4.41	4.55	4.63	4.27	5.05	4.91
Dy	4.58	4.72	4.81	4.40	5.19	5.05
Ho	0.95	0.97	0.98	0.90	1.09	1.07
Er	2.62	2.71	2.74	2.52	3.03	2.93
Tm	0.37	0.37	0.39	0.35	0.44	0.43
Yb	2.46	2.53	2.57	2.34	2.73	2.68
Lu	0.36	0.38	0.38	0.35	0.42	0.42

Unit		**Lambahraun**		
Sample no.	**IT-181**	**IT-182**	**IT-184**	**IT-184**
Ba	40.7	49.2	46.4	48.9
La	6.26	8.54	7.83	8.31
Ce	15.9	21.0	19.5	20.6
Pr	2.48	3.20	2.96	3.12
Nd	11.3	14.1	13.1	13.8
Sm	3.29	3.99	3.72	3.90
Eu	1.33	1.53	1.44	1.51
Gd	3.97	4.61	4.42	4.60
Tb	0.69	0.80	0.76	0.80
Gd	4.07	4.73	4.51	4.70
Dy	4.22	4.86	4.70	4.93
Ho	0.88	1.01	0.98	1.04
Er	2.44	2.83	2.74	2.92
Tm	0.36	0.41	0.40	0.42
Yb	2.22	2.55	2.52	2.64
Lu	0.34	0.40	0.38	0.41

3.3.4. Mineral Analyses by Electron Microprobe

Mineral compositions were determined using the University of Hawai‘i Cameca SX-50 five-spectrometer electron microprobe, using an accelerating voltage of 15 kV, 20 nA beam current, and 10 μm beam diameter. Olivine and plagioclase analyses reported here are averages of a minimum of three spots collected from individual crystals (Table 3.4). Zoning profiles also were collected for selected plagioclase phenocrysts. A PAP-ZAF matrix correction was applied to all analyses.

Olivine was analyzed for Si, Mg, Fe, Ca, Mn and Ni using peak counting times of 60 s for Mg, Si, Ca and Fe, and 30 s for Mn and Ni. Background counting times were 30 s for Mg, Si, Ca and Fe, and 15 s for Mn and Ni. Samples were calibrated against San Carlos olivine (Mg), Springwater olivine (Fe), Verma garnet (Mn), diopside (Si and Ca) and Ni-metal (Ni) standards.

Plagioclase was analyzed for Si, Al, Fe, Mg, Ca, Na and K with peak counting times of 30 s for Si, Mg, Al and Na and 60 s for Fe, Ca and K. Background counting times were 30 s for Fe, Ca and K, and 15 s for Si, Mg, Na and Al. Na was analyzed first in each acquisition to minimize loss due to volatilization. Samples were calibrated against mineral standards Lake County plagioclase (Si and Al), San Carlos olivine (Fe and Mg), Amelia albite (Na), anorthite (Ca) and orthoclase (K).

3.3.5 Petrographic Study

Thin sections were examined for textural indications of disequilibrium and 1000-point counts were collected on selected samples to determine mineral modes. Mineral grains <0.05 mm in size appear to have crystallized post-eruption, and are considered

Table 3.4 Representative mineral analyses.

Representative Analyses of Plagioclase

Unit	Lambahraun					
Sample	**IT-184^e**	**IT-273^e**	**IT-297**			**IT-300**
Anal.			1	2	3	
SiO_2	45.7	47.5	48.8	47.3	47.4	49.7
Al_2O_3	34.0	32.8	31.8	33.0	32.7	31.2
FeO^a	0.57	0.49	0.58	0.59	0.55	0.66
MgO	0.15	0.19	0.19	0.19	0.18	0.21
CaO	17.3	15.9	15.2	16.3	16.0	14.3
Na_2O	1.47	2.18	2.73	2.09	2.37	3.15
$Total^b$	99.2	99.0	99.3	99.5	99.2	99.2
Cations on the basis of 8 oxygens						
Si	2.127	2.202	2.253	2.188	2.198	2.292
Al	1.865	1.792	1.730	1.799	1.787	1.696
Fe	0.010	0.009	0.010	0.010	0.010	0.011
Mg	0.010	0.013	0.013	0.013	0.012	0.014
Ca	0.863	0.789	0.754	0.808	0.795	0.706
Na	0.133	0.196	0.244	0.187	0.213	0.282
Total	5.007	5.000	5.004	5.006	5.015	5.001
An^c	86.7	80.0	75.4	81.1	78.7	71.3

Representative Analyses of Olivine

Unit	Lambahraun					
Sample	**IT-182**	**IT-273^e**		**IT-276**	**IT-297**	**IT-300**
Anal.		1	2			
SiO_2	38.9	38.4	38.2	37.7	38.6	38.3
FeO^a	17.3	19.2	19.5	21.9	19.9	21.3
MnO	0.26	0.31	0.29	0.32	0.27	0.31
MgO	43.5	41.5	41.5	39.4	40.7	39.8
CaO	0.29	0.36	0.33	0.35	0.34	0.39
NiO	0.16	0.14	0.12	0.10	0.10	0.07
Total	100.4	99.9	99.9	99.8	99.9	100.2
Cations on the basis of 4 oxygens						
Si	1.039	1.047	1.044	1.054	1.057	1.059
Fe	0.174	0.197	0.201	0.230	0.205	0.222
Mn	0.006	0.007	0.007	0.008	0.006	0.007
Mg	1.731	1.687	1.692	1.642	1.662	1.640
Ca	0.008	0.011	0.010	0.010	0.010	0.012
Ni	0.003	0.003	0.003	0.002	0.002	0.002
Total	2.961	2.953	2.956	2.946	2.943	2.941
Fo^d	81.7	79.4	79.1	76.2	78.5	76.9

Table 3.4 (Continued) Representative mineral analyses.

Representative Analyses of Plagioclase

Unit	**Thjófahraun**	
Sample **Anal.**	**IT-35**	**IT-133**
SiO_2	48.6	49.0
Al_2O_3	32.1	31.7
FeO^a	0.64	0.69
MgO	0.19	0.18
CaO	15.3	15.2
Na_2O	2.60	2.76
$Total^b$	99.4	99.5
Cations on the basis of 8 oxygens		
Si	2.242	2.260
Al	1.746	1.723
Fe	0.011	0.012
Mg	0.013	0.012
Ca	0.756	0.749
Na	0.233	0.247
Total	5.001	5.002
An^c	76.4	75.0

Representative Analyses of Olivine

Unit	**Thjófahraun**	
Sample **Anal.**	**IT-35**	**IT-133**
SiO_2	39.4	38.9
FeO^a	17.0	16.3
MnO	0.25	0.36
MgO	43.0	44.0
CaO	0.29	0.28
NiO	0.14	0.22
Total	100.1	100.1
Cations on the basis of 4 oxygens		
Si	1.051	1.035
Fe	0.171	0.163
Mn	0.006	0.008
Mg	1.710	1.746
Ca	0.008	0.008
Ni	0.003	0.005
Total	2.949	2.965
Fo^d	81.9	82.8

[a] Total Fe as FeO

[b] K_2O for all plagioclase analyses is below detection limit = 0.017 wt. %

[c] An = Ca*100/(Ca+Na+K)

[d] Fo = Mg*100/(Mg+Fe)

[e] Lambahraun sample with plagioclase accumulation

Table 3.5 Petrographic modes. Rock modes based on 1000-point counts.

		Relative Phase Abundance (%)					
unit	**sample**	**ol**	**plag**	**cpx**	**gm**	**vesicles**	**total**
Lambahraun	IT-181	5.9	8.5	0.2	70	15.4	100.0
	IT-182	0.2	7.6	--	74.4	17.8	100.0
	IT-183[a]	22.7	36.2	3.6	15.4	22.1	100.0
	IT-185	1.6	4.4	0.1	87	6.9	100.0
	IT-274[a]	12.6	20.6	5.5	43.5	17.8	100.0
	IT-298[a]	23.4	34.8	3.6	25.1	13.1	100.0
	IT-299	1.4	3.1	--	75.5	20	100.0
	IT-301	2.8	16.2	0.7	57.8	22.5	100.0
	IT-483[a]	6.4	19.1	1.5	54.5	18.5	100.0
	IT-485[a]	6	17.2	1.3	58	17.5	100.0
	IT-486[a]	7.7	14.8	--	53.2	24.3	100.0
	IT-487	3.8	3.8	--	69.2	23.2	100.0
	IT-490[a]	9.3	13.6	0.4	63.6	13.1	100.0
	IT-492[a]	18.7	29.3	5.6	26.3	20.1	100.0
Thjófahraun	IT-35	2.8	5.9	--	76.9	14.4	100.0
	IT-42A	1.8	1.1	--	79.8	17.3	100.0
	IT-42B	2.0	1.3	--	78.5	18.2	100.0
	IT-81	1.7	2.7	--	75.5	20.1	100.0
	IT-133	2.2	0.3	--	87.2	10.3	100.0
	IT-134A	1.3	0.4	--	82.2	16.1	100.0
	IT-135	2.9	1.2	--	79.5	16.4	100.0
	IT-139	1.3	4.1	--	79.3	15.3	100.0
	IT-144A	2.5	1.6	--	86.2	9.7	100.0
	IT-156	4.1	6.8	--	71.4	17.7	100.0
	IT-158	3.4	0.1	--	78.7	17.8	100.0
	IT-159	2.2	6.3	--	76	15.5	100.0
	IT-169	1.8	0.9	--	90.1	7.2	100.0
	IT-367	3.2	1.1	--	87.8	7.9	100.0

[a] Sample has coarse groundmass. Point counts not representative of phenocryst assemblage.

"groundmass" for counting purposes, so that our modes reflect the pre-eruptive phenocryst assemblage. Exceptions to this are some samples from Lambahraun whose groundmass has crystallized to sub-ophitic textures – modes from these samples represent an assemblage that has cooled relatively slowly after eruption. Modal data are reported in Table 3.5 with estimated errors ranging from <1-3 % (Howarth, 1998).

3.4 Results and observations

3.4.1. Eruptive Units and Chronology

3.4.1.1 Thjófahraun

Thjófahraun lavas erupted from a highly effusive fissure system approximately 9 km long (Fig. 3.3). Radiometric carbon dating of charcoal remains beneath flows of this unit yields an age of 3680 ± 60 calibrated years B.P. (Sinton et al., 2005). About 1.0 km^3 of lava was erupted from 10 separate spatter cones aligned in a SW-NE trend. Lava channels up to 100-m wide are well developed close to eruptive vents, but we have not identified lava tubes or tube break-out structures in this unit.

We have divided the Thjófahraun field into 19 different subunits with boundaries defined by field observations and mineralogical differences (Fig. 3.3). All of the early phases of the eruption are pāhoehoe lava. Later units include some flows with transitional morphology. The youngest flow units are small-volume ‘a‘ā flows. Individual lava flows range up to 5 m thick, although many are less. Many of the subunits can be correlated to specific vent locations.

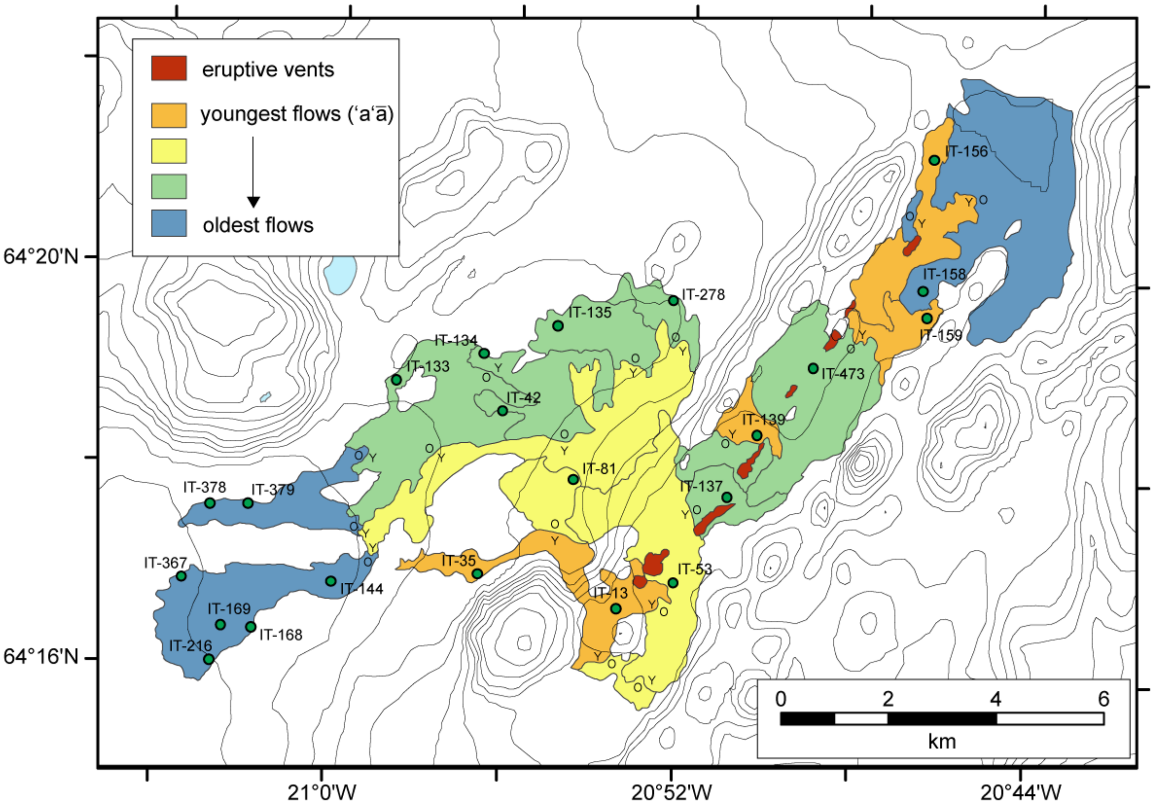

Figure 3.3 Geologic map of Thjófahraun. Subunits defined on field relations (overlapping flows) and mineralogical differences. Y in Y-O pairings designates younger flows. Circles denote locations of samples with whole-rock XRF analyses. Topographic contours are in 20 m intervals.

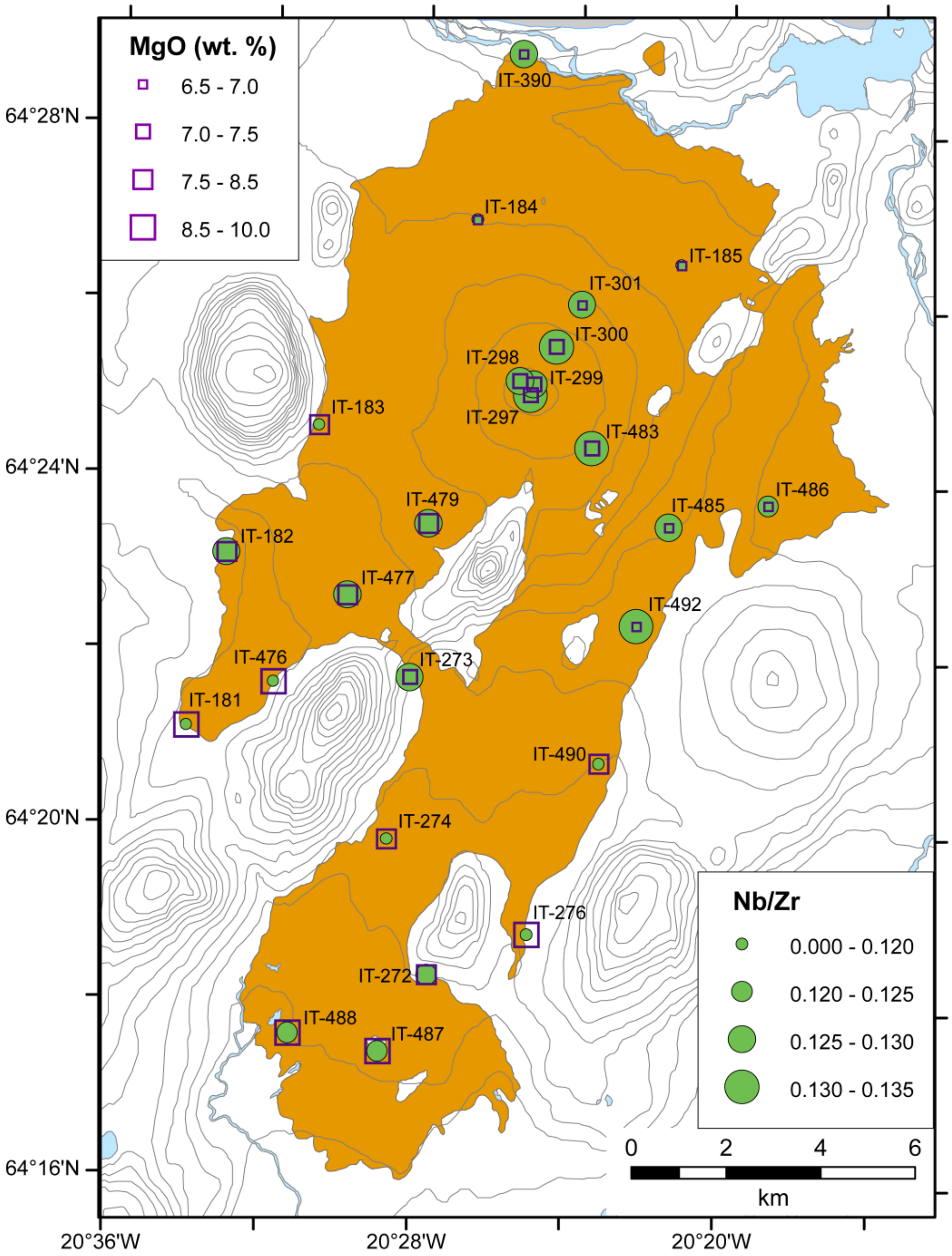

Figure 3.4 Geologic map of Lambahraun. Sample locations with XRF analyses shown. Symbol size scales with Nb/Zr (circles) and MgO wt. % (squares). More distal samples tend to have higher MgO and lower Nb/Zr than samples closer to the vent. Topographic contours are in 20 m intervals.

The relative age relations between subunits allow us to trace this eruption's chemical and mineralogical variability through time. Some of the oldest lavas make up the lower SW and NE-most portions of Thjófahraun. These subunits tend to be more olivine-phyric (up to 7 %) and have slightly higher MgO contents than lavas in the SE. We are unable to determine age relations between the older NE and SW subunits, so it is difficult to say if there is an age sequence to vent activity, but both areas are generally older than the SE lavas based on stratigraphic field relations. The last lavas erupted are plagioclase-phyric ʻaʻā lavas erupted from at least three vents spanning almost the entire length of the eruptive fissure system. These later lavas contain very little olivine (<3 %), but more abundant plagioclase phenocrysts (5-7 %). By comparison with the well-documented 1975-1984 fissure-fed Krafla Fires eruptive episode (Björnsson, 1985; Sæmundsson, 1991), the flow field was probably produced during a series of short-lived (days to weeks) eruptive events that together comprise a major rifting episode. Although the exact duration of this episode is not known, estimates of effusion rates for pāhoehoe and ʻaʻā lavas (Rowland and Walker, 1990) indicate a total eruption time for the complete 1 km^3 of Thjófahraun lava on the order of months to years.

3.4.1.2 Lambahraun lava shield

Lambahraun is a moderately large, monogenetic, low-angle lava shield covering >140 km^2, with an estimated 7.3 km^3 of erupted lava (Fig. 3.4). Radiometric dating from two separate localities gives an average age of 4100 ± 500 years B.P. (Sinton et al., 2005). Lambahraun mainly consists of dense pāhoehoe lava in hundreds of thin flow units that likely formed at low effusion rates (Rowland and Walker, 1990; Rossi, 1996).

The large erupted volume and inferred low average eruption rate suggests that this lava shield was produced over a period of several decades. Although the field mainly consists of on-lapping flow units, there are no mappable subunits within it. Furthermore, large hornito spires are common around the summit caldera and we have identified at least one major tube breakout elsewhere in the flow field. Thus, tube-fed lavas are probably more common in Lambahraun than in Thjófahraun and correlation of individual samples with time during eruption is more equivocal. Lambahraun lavas tend to be more porphyritic than Thjófahraun lavas with little indication for any systematic spatial correlation of its mineralogy. Many samples are nearly holocrystalline, particularly in the interiors of tumuli, indicating relatively slow cooling after eruption.

Although we are unable to define a strict eruption chronology for Lambahraun, the flow field is areally zoned with respect to several chemical parameters. Samples from the SW portions of the flow field tend to have higher MgO and lower Nb/Zr than those closer to the summit vent in the NE (Fig. 3.4). Despite the complications that tube-fed lava adds to determining an eruption chronology, in general the more distal SW lavas appear to have erupted earlier than the more evolved lavas N and E of the summit caldera. The spatial relationships therefore suggest that the erupted magma generally became progressively more differentiated with higher Nb/Zr during the course of the eruption. Late eruption of more differentiated magma has also been observed in other WVZ lava shields (Sinton et al., 2005) and elsewhere in Iceland (N. Óskarsson, pers. comm.).

3.4.2 Chemical Variations

3.4.2.1 Crystal fractionation

Olivines in both Thjófahraun and Lambahraun appear to be in equilibrium with their host rocks (Roeder and Emslie, 1970) based on mineral and whole rock compositions. Groundmass olivines and rims on olivine phenocrysts commonly have slightly lower forsterite (Fo = Mg*100/(Mg+Fe)) contents than phenocryst cores, consistent with later crystallization. Plagioclase phenocrysts tend to have normal or oscillatory zoning, and some of the larger phenocrysts have a sieved texture. Thjófahraun plagioclase grains have significantly lower An content for a given rock MgO or coexisting olivine Fo content than Lambahraun plagioclase. We interpret this to reflect the lower CaO of the melt from which they crystallize, as Thjófahraun lavas have lower CaO contents than Lambahraun at the same MgO (Fig. 3.5), while Na and Al contents are not significantly different.

The whole-rock chemical variation of Thjófahraun is broadly consistent with evolution by shallow crystal fractionation. Analyzed samples span a range of ~1.5 wt. % MgO around a median of 8.0 wt. %, and exhibit limited chemical variability at a given MgO (Fig. 3.5). While lava compositions are more restricted in MgO than for Lambahraun, the range of values at a given MgO appears to be greater. Although plagioclase occurs in some of the samples, CaO and Al_2O_3 values anti-correlate with MgO, suggesting that Thjófahraun magmas did not fractionate plagioclase prior to eruption. Early Thjófahraun flows have compositions spanning the entire spread of MgO. Late-stage ‘a‘ā lavas have relatively low MgO with limited chemical variability

(Fig. 3.5). These results suggest early eruption from a relatively poorly mixed magma chamber, followed by later eruptions that tapped a more homogeneous and probably smaller volume of more differentiated magma.

The major and trace element variation of Thjófahraun whole rocks can be modeled by simple fractionation scenarios using MELTS (Ghiorso and Sack, 1995; Smith and Asimow, 2005). The best-fit model run contains 0.4 wt. % H_2O for a crystallization pressure of 1 kb (QFM-2). A value of 0.4 wt % is within the range expected for Iceland magmas (e.g., Schilling et al., 1983; Metrich et al., 1991; Nichols et al., 2002), although MELTS runs with lower water contents are also able to approximate the observed trends at slightly higher pressures (1.5-2 kb). Note that there is some uncertainty in the water content due to the interplay with the model pressure, because both higher water content and higher pressures suppress the appearance of plagioclase on the liquid line of descent. Although we biased our analyses to the least phyric samples, the data reported are for whole rocks, and therefore not true liquid compositions.

Lambahraun samples show a greater variation in MgO than Thjófahraun (~2.5 wt. % MgO), and are significantly lower in K_2O, Rb, Y and Zr, and higher in CaO than Thjófahraun lavas for the same MgO. Overall chemical variations within Lambahraun are more complicated than for Thjófahraun. For example, there are two distinct populations of Lambahraun samples on Al_2O_3, FeO and TiO_2 versus MgO (Fig. 3.5). Also, both CaO and Nb/Zr increase with decreasing MgO, despite widespread presence of plagioclase in Lambahraun lavas. Thus, several features of Lambahraun are inconsistent with simple low-pressure fractionation of the mineral phases observed in the lava, especially at low MgO.

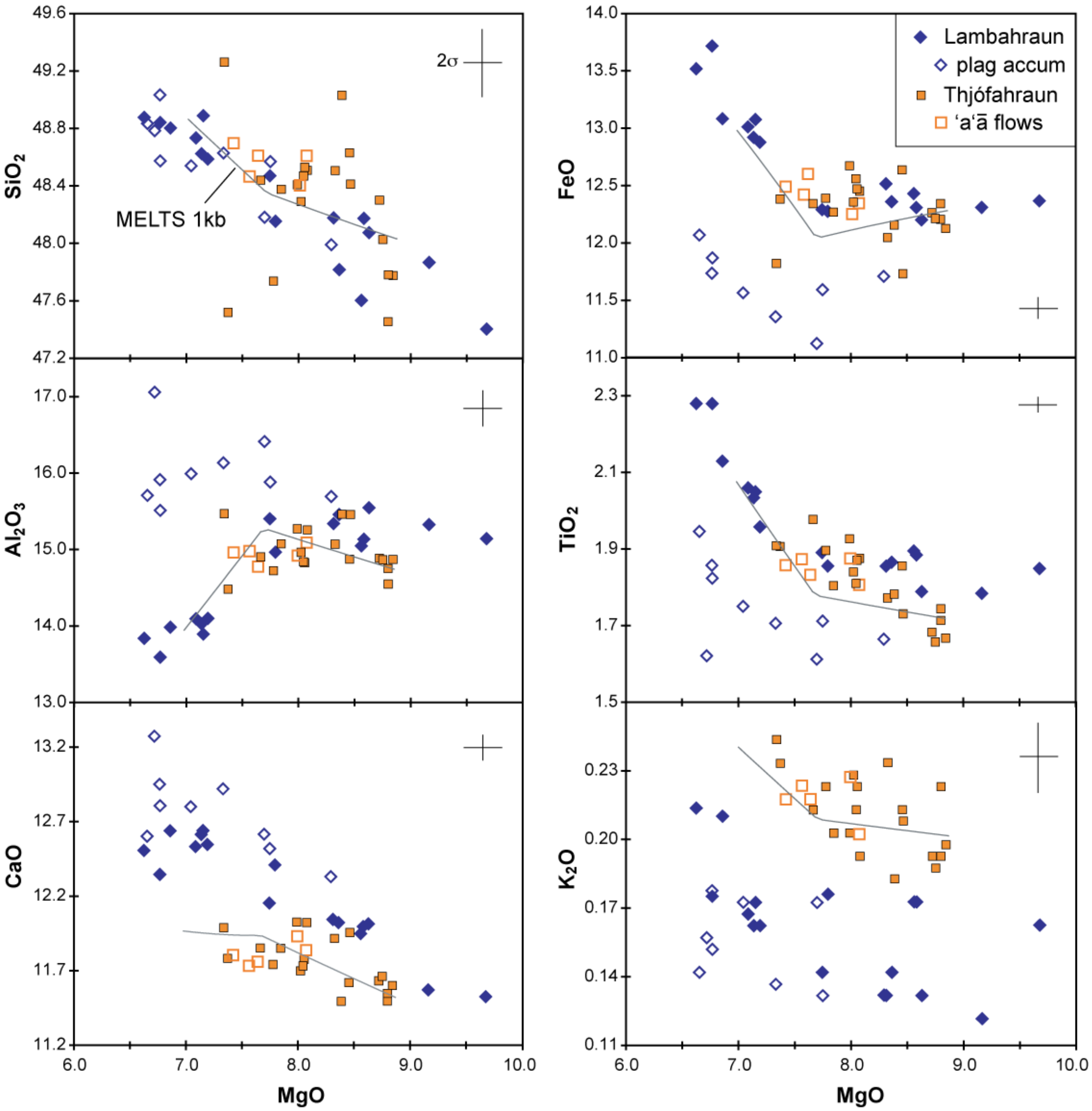

Figure 3.5 Major element chemical variations of Thjófahraun (squares) and Lambahraun (diamonds). Open diamonds are Lambahraun samples displaced from the main trend, which we interpret to be affected by plagioclase accumulation (see text for discussion). Open squares denote Thjófahraun late-stage ‘a‘ā flows. Solid line shows 1 kb fractionation model for Thjófahraun determined by the Adiabat_1ph version of MELTS (Ghiorso and Sack, 1995; Smith and Asimow, 2005) with oxygen fugacity of QFM-2 and

0.4 wt. % H_2O in the starting magma (IT-133). Crosses in each panel denote 2σ uncertainty in analytical data.

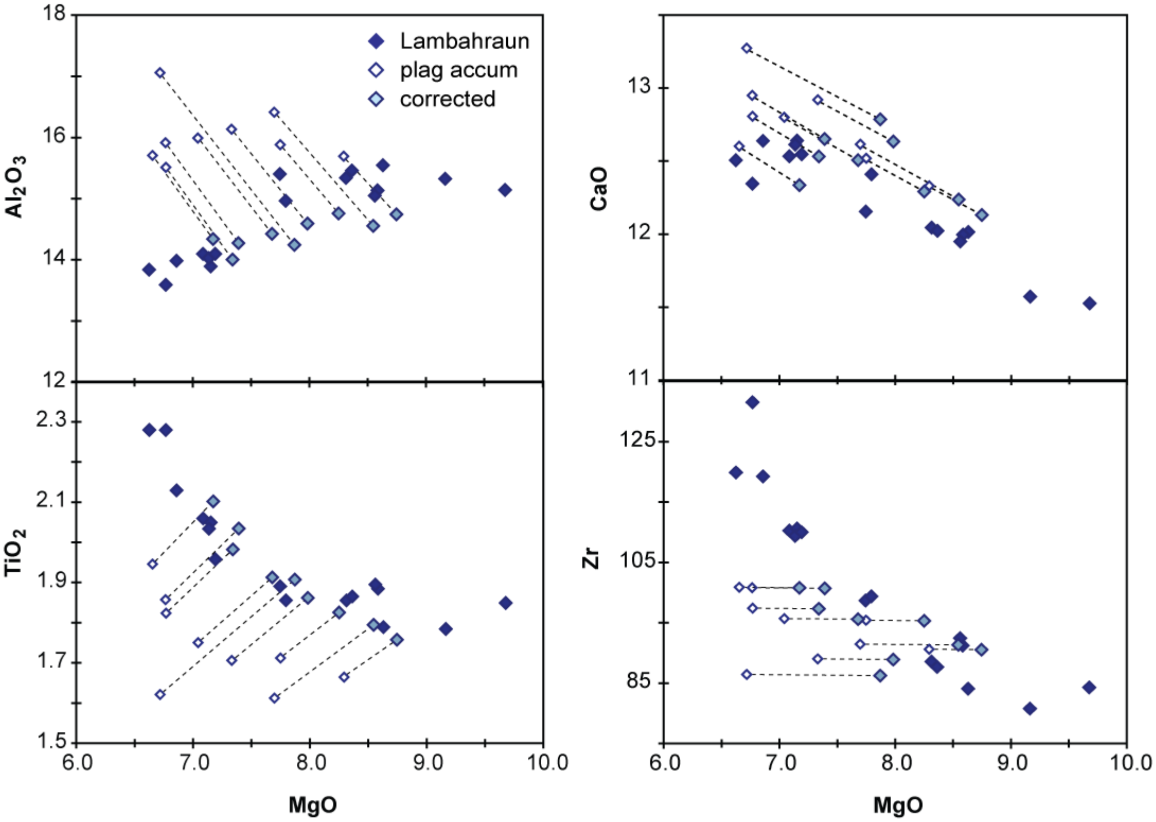

Figure 3.6 Correction for plagioclase accumulation in Lambahraun samples. Sample compositions corrected back to the main liquid line of descent for Lambahraun (solid symbols) along lines of constant Mg# using an average plagioclase composition. Open diamonds are uncorrected values, shaded diamonds are corrected compositions.

3.4.2.2. Crystal accumulation in Lambahraun lavas

Some Lambahraun samples have higher Al_2O_3 and CaO and significantly lower FeO, TiO_2, P_2O_5, and to a lesser degree K_2O (open symbols, Fig. 3.5), than the main trend of most samples from this unit. These same samples also tend to be low in Mn, Sc, V, Zn, Y, Zr and Nb, while exhibiting slightly higher Sr. Such variation is not consistent with crystal fractionation, but can be explained by up to 15 % accumulation of plagioclase in these whole-rock samples. The amount of plagioclase accumulation has been evaluated by linear subtraction of a representative plagioclase composition (IT-273 analysis in Table 3.4) from these sample compositions along a path of constant Mg# until the liquid intersects the main liquid line of descent. The amount of plagioclase subtracted ranges from 5-15%, and is in all cases less than the amount of modal plagioclase in the sample (Table 3.6, Fig. 3.6). The part of the system where excess plagioclase was

Table 3.6 Plagioclase accumulation in Lambahraun samples (mass fractions).

sample	modal plag	modeled accum
IT-183	0.43	0.06
IT-273	0.20	0.08
IT-184	0.15	0.07
IT-301	0.20	0.08
IT-479	0.19	0.10
IT-483	0.22	0.09
IT-485	0.19	0.09
IT-486	0.18	0.15
IT-490	0.14	0.05

accumulated is poorly constrained, but presumably could occur by gravitative or dynamic processes in a magma reservoir, during transport to the surface, or in lava flows after eruption. The latter interpretation is supported by the observation of substantial variations in plagioclase abundance over scales of a few decimeters within individual tumuli of the flow field, although this observation does not preclude the possibility that some accumulation could be pre-eruptive.

Among the most surprising features of the Lambahraun data are steady increases in CaO, highly incompatible element abundances, and incompatible element ratios such as Nb/Zr with decreasing MgO (Fig. 3.7). Although some major element trends (e.g., Al_2O_3, FeO) indicate plagioclase fractionation has occurred, CaO abundances are higher than would be predicted by simple crystal fractionation alone, even after correcting for plagioclase accumulation. Low-pressure crystal fractionation paths predicted by MELTS (Ghiorso and Sack, 1995; Smith and Asimow, 2005) yield CaO and incompatible element values significantly lower than the observed trends (Fig. 3.7). While crystallization at slightly higher pressures can lead to higher CaO contents due to the delay in plagioclase crystallization, this is inconsistent with other major element trends, particularly that of Al_2O_3. CaO will become even more depleted at higher pressures of fractionation because of the early crystallization of Ca-rich pyroxene at high pressure. These results indicate that Lambahraun lava compositions are inconsistent with the combined effects of crystal fractionation and plagioclase accumulation.

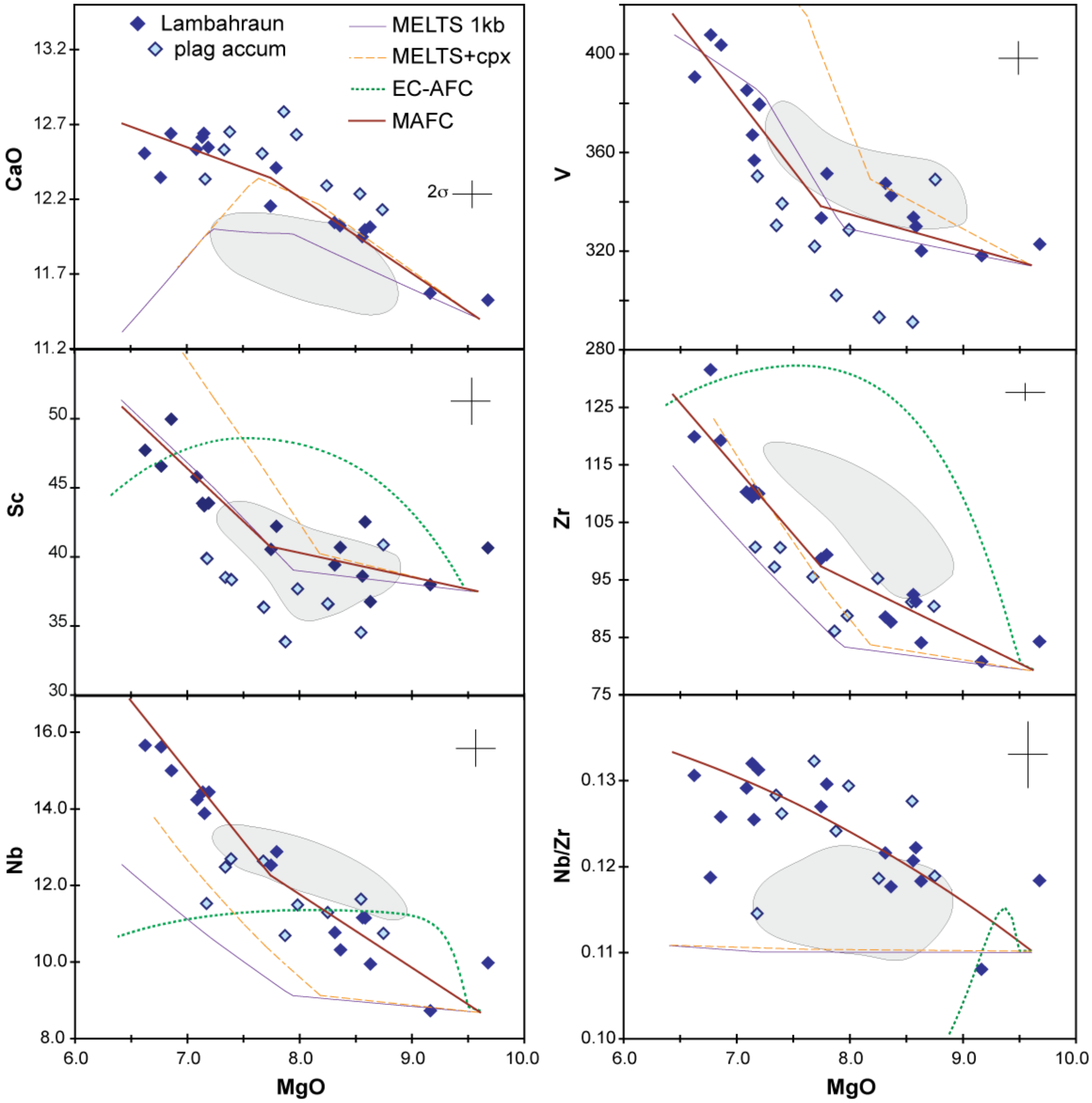

Figure 3.7 Selected chemical variations of Lambahraun; shaded diamonds are sample compositions that have been corrected for plagioclase accumulation (see text and Fig. 3.6). Thjófahraun data shown as gray fields. Thin solid line is the MELTS fractionation model for Lambahraun (see Fig. 3.5 caption for run conditions); thin dashed line is the MELTS fractionation trend plus the addition of increasing amounts of clinopyroxene accumulation (see text for discussion); dotted line shows energy-constrained AFC model

using equations of Spera and Bohrson (2001); thick solid line is the MAFC model calculation which simulates crustal interaction during melt migration by “refreshing” wallrock composition in each step (see text for description of calculation). Wallrock composition and other details of the AFC and MAFC models are given in Table 3.8.

Table 3.7 Linear regression of Lambahraun evolution.

	Parent IT-181	**Daughter** IT-185	**ol**	**plag**	**cpx**	**predicted melt comp.**
SiO_2	47.87	48.84	40.14	46.73	53.58	48.83
TiO_2	1.78	2.28	0	0	1.12	2.22
Al_2O_3	15.33	13.59	0	34.16	4.01	13.59
FeO	12.31	13.72	11.46	0.40	6.37	13.74
MnO	0.19	0.22	0.24	0	0.10	0.25
MgO	9.16	6.77	47.00	0	15.45	6.77
CaO	11.57	12.35	0.30	17.10	20.03	12.37
K_2O	0.12	0.18	0	0.02	0	0.19
P_2O_5	0.16	0.26	0	0	0	0.24
	Predicted contributions:		-0.11	-0.14	0.05	

Negative predicted contributions represent net fractional crystallization of the mineral phase; positive values represent net addition (assimilation).

The progressive increase in CaO and decrease in Al_2O_3 with decreasing MgO requires the addition of a Ca-rich, Al-poor component, such as clinopyroxene, in this process. Multiple linear regression of the major elements indicates a net addition of ~5 % clinopyroxene for the total range of MgO concurrent with olivine and plagioclase removal to explain the high CaO and other major element values in the more evolved rocks (Table 3.7). As crystal accumulation has already been shown to play a role in Lambahraun's evolution, and there is both petrographic and chemical evidence for clinopyroxene accumulation in selected other Icelandic lava flows (Maclennan, 2008a; Halldórsson et al., 2008), it is appropriate to consider whether the progressive enrichment in CaO and incompatible elements can be accounted for by increasing amounts of clinopyroxene accumulation with decreasing MgO content, despite a lack of petrographic evidence for this process in Lambahraun samples. The thin dashed line in Fig. 3.7 shows a predicted evolutionary trend calculated by addition of increasing amounts of clinopyroxene, up to a total ~5 % accumulation predicted from mass balance at low MgO, to the MELTS-predicted fractionation run. This predicted trend fits the major element data better than fractionation ± plagioclase accumulation alone, but only at MgO values greater than ~7.5 wt. % MgO, below which clinopyroxene accumulation and the MELTS-predicted clinopyroxene fractionation paths are co-linear. Although the major element data could be reconciled with clinopyroxene accumulation to magmas that failed to fractionate clinopyroxene, e.g., magmas that crystallized clinopyroxene crystals that were not fractionated, this process produces striking misfits to the trace element variations. Incompatible elements such as Nb and Zr show under-enrichments at lower

MgO, and trace elements that are less incompatible in clinopyroxene, like V and Sc, exhibit striking over-enrichments.

Taken together, there is both petrographic and chemical evidence for accumulation of excess plagioclase crystals in some Lambahraun rocks, and visual evidence in outcrops that plagioclase crystals are mobile in surface lava flows of this unit. Although clinopyroxene accumulation produces slightly better fits to major element data, it produces greater misfits in trace element variations. Thus, although clinopyroxene accumulation has been well documented in some Icelandic lava flows, we lack both petrographic and chemical evidence that it has been important in controlling the unusual Lambahraun chemical variation.

3.4.2.3. Evidence for partial melting processes in Lambahraun evolution

In addition to the enrichment in CaO and Nb at low MgO values, are enrichments in light rare earth elements (REE) (Fig. 3.8). The magnitude of enrichment for a given element is approximately inversely correlated with melting partition coefficients for these elements, such that the most highly incompatible elements Nb, Zr, La, Ce show the greatest enrichment at low MgO. We calculate the effective over-enrichment for elements i in a low-MgO Lambahraun composition (6.7 wt. %) as $\varepsilon_i = C_i/C_i^*$, where C_i is the concentration of element i in the sample, and C_i^* is the expected concentration of that element from crystal fractionation. There is a clear negative correlation between the cpx-liquid partition coefficient ($K_d^{\text{cpx-liq}}$) and the degree of over-enrichment (ε_i) (Fig. 3.9). The relationship between trace element incompatibility and the relative misfits of Lambahraun data from predicted crystal fractionation trends is consistent with partial

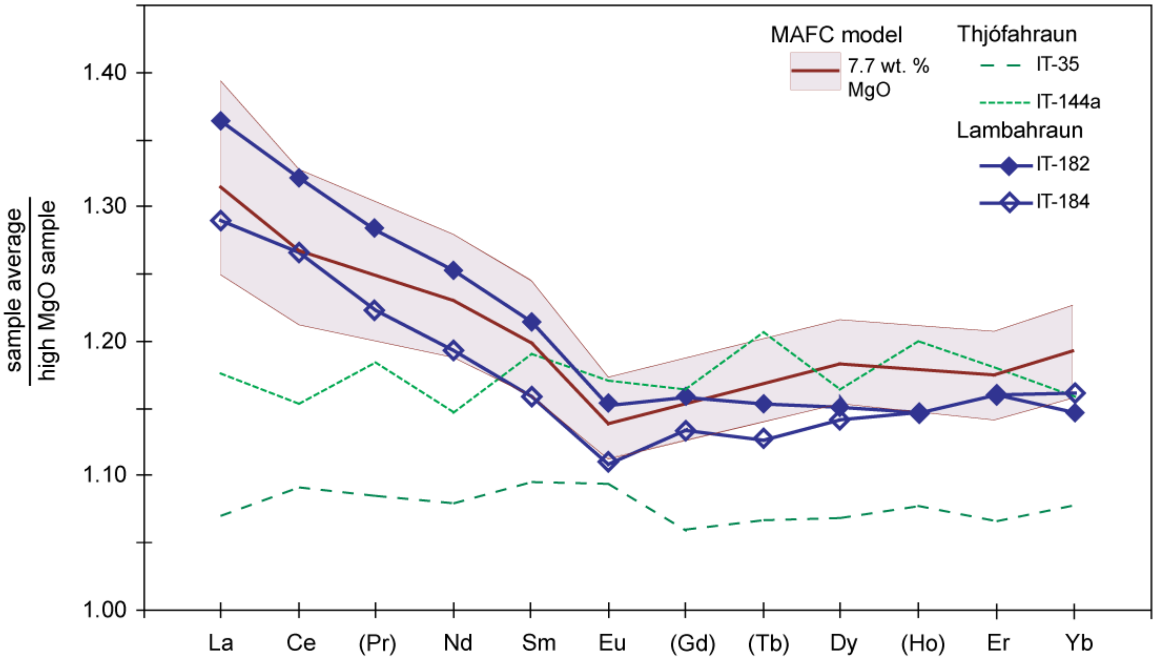

Figure 3.8 Selected rare earth elements (REE) for Lambahraun and Thjófahraun samples normalized to the highest MgO sample analyzed by ICP-MS for their respective units (IT-181 for Lambahraun, IT-133 for Thjófahraun). Elements in parentheses not included in modeling. Relatively flat patterns for Thjófahraun samples with total REE abundance increasing with decreasing MgO are consistent with fractionation. Note the pronounced enrichment in light REE relative to heavy REE in Lambahraun samples with low MgO. Model runs represent mixing of 0.1 % partial melting of wallrock in each increment of -0.1 wt. % MgO, shown for a range of mixing proportions (*M* = ratio of anatectic to primary melt).

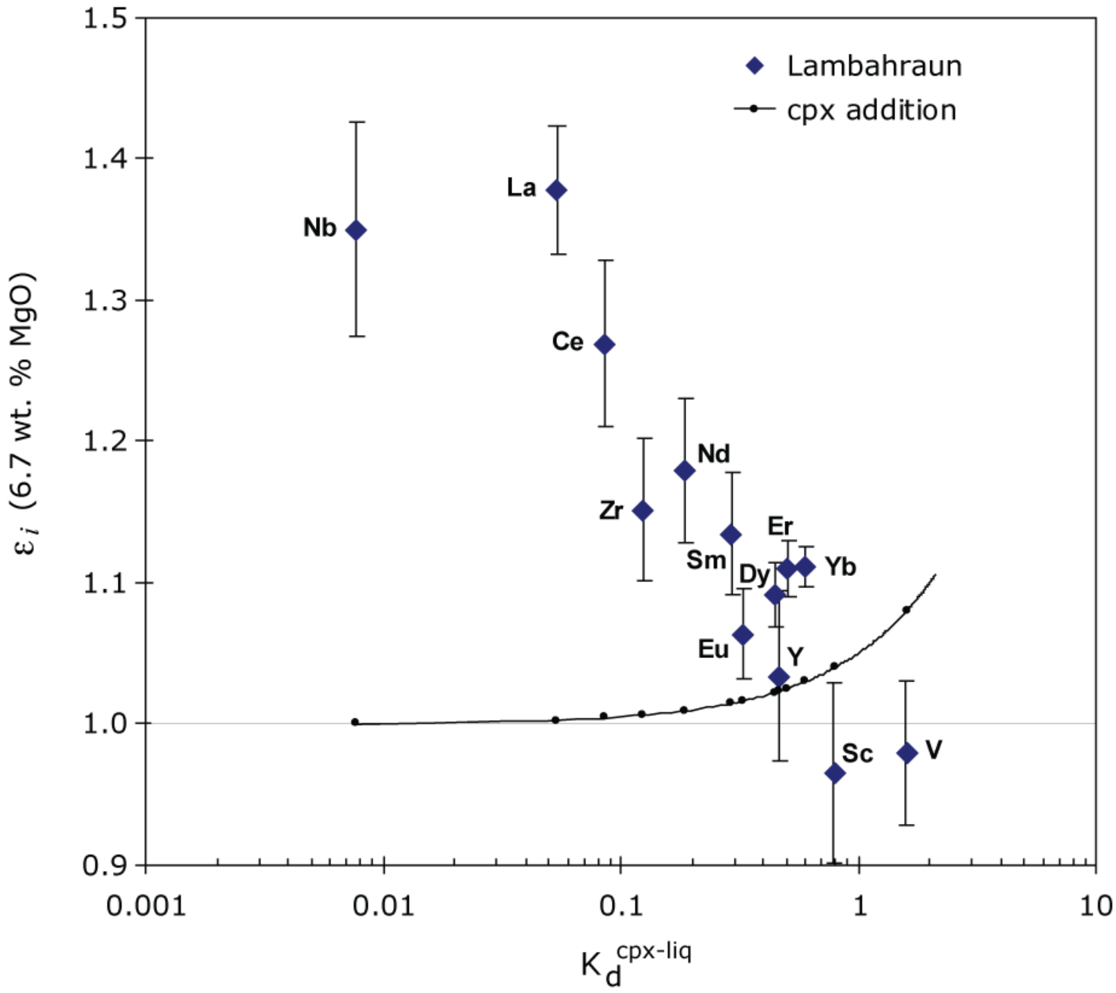

Figure 3.9 Plot of enrichment factors (ε_i) for selected trace elements at 6.7 wt. % MgO vs. clinopyroxene-liquid partition coefficient ($k_d^{cpx\text{-}liq}$). Enrichment factor for each element calculated as $\varepsilon_i = C_i/C_i^*$, where C_i is the concentration of element i in the sample, and C_i^* is the expected concentration of that element from crystal fractionation; error bars denote root mean square deviation of ε_I-MgO for all samples. Black line shows values for accumulation of ~5 % clinopyroxene crystals. The result indicates that Lambahraun incompatible element enrichment is consistent with partial melting of clinopyroxene, and not accumulation or digestion of clinopyroxene crystals.

melting, and opposite of what one would expect for clinopyroxene crystal accumulation in the proportion required by the major element linear regression analysis (Fig. 3.9). We therefore consider various scenarios in which a partial melting process may contribute to Lambahraun's geochemical evolution. This partial melting signature could be produced either in mantle melting, e.g., by variable melting or source variations, or by reaction in the crust. In this section, we outline and evaluate different mechanisms by which apparent coupling between magma evolution and enrichment via partial melting could occur.

Simple magma mixing between incompatible element-depleted, high-MgO magma and incompatible element-enriched, low MgO magma should produce linear chemical variation versus MgO, as seen, for example, in the variation trends of P and Nb. However, many element trends exhibit distinct kinks correlated to fractionating phases or curved relations with MgO (e.g., Al_2O_3, TiO_2, FeO, Sc, V). Additionally, spatial variations in the Lambahraun flow field (Fig. 3.4) suggest that low-MgO lavas with the highest Nb/Zr ratios were erupted late in the sequence of the volcano. Thus, the inferred eruptive sequence and chemical variations are inconsistent with progressive recharge where the most recent magma would be expected to be more Mg-rich than the resident magma.

A slightly different scenario is that incompatible element-depleted resident magma is progressively diluted with more enriched recharge magma prior to or concurrent with crystal fractionation. Concurrent mixing and crystallization was proposed by Maclennan (2008a) to explain olivine melt inclusion data from the Northern Volcanic Zone in Iceland. However, although the relative trace element enrichments are correlated with $K_d^{cpx\text{-}liq}$, they also are associated with enrichment of CaO, which would not be expected from variable partial melting of a common upper mantle assemblage. Therefore, if Lambahraun variations reflect mixing of melts derived from mantle melting, the source mantle must be heterogeneous on a very small scale and produce differing primary magma compositions over a timescale of decades. Although there is evidence for heterogeneities in the mantle under Iceland (Zindler et al., 1979; Hémond et al., 1993; Stracke et al., 2003; Thirlwall et al., 2004; Maclennan, 2008a), preliminary isotopic data (Haldórsson et al., 2008b) indicates that the source mantle for Thjófahraun and both high-Nb/Zr and low-Nb/Zr Lambahraun lavas are isotopically similar. Thus, if mantle heterogeneity is responsible for varying incompatible element ratios in Lambahraun, the trace element heterogeneity must be decoupled from isotopic ratios, and progressive recharge must be accompanied by an increase in fractionation.

3.4.3 Crustal interaction in Lambahraun magmas

An alternative process that couples incompatible element enrichment and decreasing Mg# is melt-wallrock interaction during melt migration and/or storage in the crust. Our major element mass balance results indicate combined addition of a clinopyroxene component coupled to fractional crystallization of plagioclase and olivine. Because the magnitudes of enrichment are approximately inversely correlated with clinopyroxene-liquid partition coefficients (Fig. 3.9), the clinopyroxene assimilant must be in the form of clinopyroxene-dominated melts, rather than whole-scale digestion of clinopyroxene crystals. In this regard, the process is similar to concurrent assimilation and fractional crystallization (AFC) (e.g. DePaolo, 1981; O'Hara, 1995, 1998; Spera and Bohrson, 2001).

Most AFC models assume constant pressure, such as a resident magma chamber that reacts with surrounding wallrock. The composition of the anatectic (wallrock-derived) melts follow melting functions based on the partition coefficients of each element, so that the earliest anatectic melts are the most enriched in incompatible elements, followed by a gradual decline in incompatible element concentration as they are stripped from the surrounding wallrock. This process results in concave down incompatible element versus MgO variation curves for the magma (Fig. 3.7) that differ from observed Lambahraun sample data, which show a steady, continuous increase in incompatible element concentrations with MgO-variation trends that are linear to concave up.

To avoid the inevitable depletion in incompatible elements that occurs during reaction with a static wallrock, we envision a process that allows the crustal assimilant to remain relatively undepleted by prior melting. In a magma chamber setting, this might occur if partially melted wallrock is progressively stoped into the convecting interior of the chamber, exposing new wallrock for partial melting. However, we see no physical evidence for partially digested wallrock, and complete digestion should have strong effects on the major element chemical variability, depending on the mode of the digested crustal material. While we have not fully explored the chemical consequences of this process, we propose instead that wallrock melting occurs during melt migration through the crust, which eliminates the need to account for undigested crustal material. In this model, partial melts of wallrock are assimilated over a range of pressures determined by the initial temperature and solidus of the wallrock, and the amount of heat conducted from a migrating melt into its surroundings. This process naturally increases the melt's incompatible element concentration by continually introducing fresh, unmelted wallrock to the anatexis process as the surrounding crust heats above its solidus. Hereafter, we refer to this process as migrating AFC (MAFC).

3.4.4 Assimilation Modeling

To model the MAFC process, we utilize equations of nonmodal fractional melting and crystallization (Shaw, 1970) in a simple, stepwise calculation. By discretizing the problem into small steps in melt MgO content (equivalent to small steps of temperature of the cooling melt), we can model crystallization of the magma and mix in variable proportions of melted wallrock, tracking the combined effects on melt composition. Crystallizing phase proportions are determined from the major element compositional variations. We define two crystallization regimes (olivine only and olivine + plagioclase) based on a distinct kink in MgO variation trends when plagioclase joins the crystallizing assemblage (~7.76 wt. % MgO). Average crystallizing proportions of olivine (MgO > 7.76) or olivine + plagioclase (MgO < 7.76) from linear regressions of these two separate portions of the major oxide trends can be divided into crystal fractions per unit MgO. For each small step in MgO, we calculate the change in incompatible element composition of the melt from fractional crystallization of the relevant phases (olivine ± plagioclase) and mix in a small proportion of melt derived from nonmodal fractional melting of wallrock. Olivine, plagioclase and clinopyroxene proportions in the wallrock (X's in Table 3.8) are set to the CIPW norm of average WVZ basalt from Sinton et al. (2005). We derived the wallrock trace element composition using the dynamic melting model for the Iceland WVZ of Sinton et al. (2005), with ~2 % melting in the garnet field followed by 10 % melting in the spinel field of primitive mantle (Sun and McDonough, 1989). Lacking further constraints on the crustal composition beneath Lambahraun, we choose this composition as representing an average crustal composition under the WVZ. This is a simplification of what is certain to be a heterogeneous crust whose composition changes with depth, quite possibly in non-systematic ways. To simulate the effects of melt migration, we "refresh" the wallrock, so that the initial composition for each AFC step is the original, unmelted crustal composition. Using the melt-solid partition coefficients given in Table 3.8, we calculate the compositional evolution of selected trace elements (Sc, V, Y, Zr, Nb, La, Ce, Sm, Eu, Dy, Yb and Lu) assuming the melting mode (*p*'s in Table 3.8) is dominated by clinopyroxene. Results are plotted in Figs. 3.7 and 3.8.

Due to the trade-off between extent of anatectic melting (F_m) and the mixing proportion (M = ratio of anatectic melt to primary magma), there is a range of conditions over which the model can approximate the observed data. Best-fit model runs have relatively low mixing proportions (M ~ 0.08-0.16 % of partial melt added in each step) and a fairly broad range of permissible F_m values (<0.1-5 % partial melting of wallrock at each step), resulting in a total contribution of 3-5 % anatectic melt over the observed range of sample MgO (9.6 – 6.6 wt. % MgO). We assume melting to be dominated by clinopyroxene, as required by the ~5 % addition of clinopyroxene indicated by major element linear regression. Although the values we used (*p*'s in Table 3.8) are somewhat arbitrary, the model is relatively insensitive to the melting mode, and a wide range of mineral contributions to the melt can produce the observed chemistry. The model we

Table 3.8 MAFC model partition coefficients and melting parameters.

Partition Coefficients				***Starting Compositions***	
mineral	**ol**	**plag**	**cpx**	C_0	C_{wr}
Sc	0.33	0.025	0.8	38	30
V	0.3	0.01	1.6	318	300
Y	0.023	0.027	0.467	23	28
Zr	0.004	0.0128	0.1234	80	83
Nb	0.001	0.04725	0.0077	8.8	4
				(IT-181)	
La	0.000007	0.08	0.0536	6.26	4
Ce	0.00001	0.1	0.0858	15.9	12
Nd	0.00007	0.1	0.1873	11.3	11
Sm	0.0007	0.0845	0.291	3.29	2.8
Eu	0.00095	0.2	0.33	1.33	1.1
Dy	0.004	0.06	0.45	4.22	4
Er	0.009	0.02	0.50	2.44	1.9
Yb	0.02	0.02	0.60	2.22	2.5
Melting Parameters					
X_{wr} **(%)**	7.8	57.7	34.4		
p **(%)**	5	5	90		

Proportions of crystallizing phases taken from major element linear regression. Partition coefficients from compilation of Keleman et al. (2003), Dunn and Sen (1994), Green (1994), Jones (1995), McKenzie and O'Nions (1991, 1995). Crustal mode (X_{wr}) determined from the CIPW norm calculation of average WVZ basalt (Sinton et al., 2005).

present in Figs. 3.7 and 3.8 contains olivine, plagioclase and clinopyroxene proportions as determined above. At such low degrees of partial melting, the model is far more sensitive to the chosen partition coefficients than the *X*'s so, although we have assumed a single wallrock composition for this exercise, a wide range of bulk crustal compositions could give similar results. Olivine can range from 5-30 %, plagioclase from 30-65 %, and clinopyroxene from 25-60 %, and still reasonably approximate the observed data within the uncertainties of the model. Because the model predictions are so sensitive to partition coefficient values (particularly for the more incompatible elements) and these are not all well-known, this is our greatest source of uncertainty.

It is important to note that our MAFC model is not thermodynamically constrained, nor does it take into account the amount of heat actually available for melting or the chemical potentials of the phases involved. Coupling thermodynamic constraints with the geochemical evolution of the individual phases, i.e., incorporating heat conduction from the migrating melt into its surroundings, the latent heat of crystallization, and pressure-dependent phase equilibria, are worth investigating, although beyond the scope of this paper. The simplified model presented here shows that the observed geochemical trends can be reproduced with reasonable extents of melting and fractionation and a suitable wallrock composition, recognizing that the magnitude of the geochemical effects of this process will ultimately depend on a range of energy constraints not presently considered.

3.5 Discussion

3.5.1 Crustal controls on MAFC processes

Factors that might control the extent of reaction of melt with the crust through which it migrates during ascent include the geometry of melt migration (i.e., whether in channels or along grain boundaries), the rate of melt supply and the melt-rock ratio at different levels in the crust. Evidence from oceanic gabbros suggests melt migration in the lower crust occurs as reactive porous flow through a crystal mush (e.g., Natland and Dick, 1996; Coogan et al., 2000; MacLeod and Yaouancq, 2000). Migration rate and the melt-rock ratio are dependent on the porosity and permeability of the mush (Hunter, 1996). The extent of reaction of melt with its surroundings might also be expected to depend on the amount of crust the melt passes through prior to eruption. Crustal thickness in the WVZ is generally in the range of 20-25 km (Bjarnason et al., 1993; Allen et al., 2002). Evidence for melt-wallrock interactions can be preserved in both the textures and compositions of gabbroic rocks as well as in the chemical signatures of erupted lavas, and crustal interaction has been called on to explain gabbro xenoliths from picritic lavas that show evidence for partial melting and mineral resorption (Larsen, 1979; Hansteen, 1991; Gurenko and Sobolev, 2006), and trace element and isotopic enrichments in Icelandic lavas (Muehlenbachs et al., 1974; Óskarsson et al., 1982; Condomines et al., 1983; Hémond et al., 1988; Nicholson et al., 1991, Maclennan, 2008b, Halldórsson et al., 2008a). Evidence from oceanic gabbro suites and ophiolites indicates melt-rock reaction may be a ubiquitous process in oceanic crust that is not unusually thick, and may be an important contributor to the geochemical evolution of MORB

(Meyer et al., 1989; Natland and Dick, 1996; Coogan et al., 2000; Bédard et al., 2000; Kvassnes and Dick, 2000; Dick et al., 2002; Kvassnes, 2004; Kvassnes and Grove, 2008; Lissenberg and Dick, 2008).

Although a MAFC process involving wallrock assimilation successfully explains many of the chemical attributes of Lambahraun, the question remains as to where this assimilation is actually occurring. As higher pressures tend to favor clinopyroxene as a solid phase, increasing its stability field at the expense of olivine, it seems unlikely that this process can take place at great depth. Thermodynamic modeling of phase relations using MELTS (Ghiorso and Sack, 1995; Smith and Asimow, 2005) indicates clinopyroxene is likely to be on the solidus at pressures < 4 kb for this basaltic melt composition. Under these conditions, olivine and plagioclase crystallization could occur simultaneously with partial melting of wallrock clinopyroxene provided heat transfer to the wallrock is sufficient to cause anatexis. As noted previously, the MAFC model is relatively insensitive to the melting mode, so we are unable to constrain the extent to which olivine and plagioclase may also be partially melted. Crystallization of olivine and plagioclase may effectively obscure any compositional contribution that melting of these phases might have, so while they may also be involved, the only distinguishable signature in the erupted basalts is the contribution from clinopyroxene.

One appealing attribute of the MAFC process is that it couples extent of fractionation and wallrock assimilation, with the most evolved (lowest MgO) rocks having the most crustal contamination. The spatial distribution (Fig. 3.4) observed in Lambahraun, in which lavas with higher incompatible elements tend to be located close to the vent while more distal lavas are less enriched, has also been observed in other

Icelandic lava shields (Maclennan et al., 2003b; Sinton et al., 2005). However, this distribution also indicates a time dependency that is less intuitive: the last lavas erupted are also the most modified by a crustal contaminant. One possible explanation is that the eruption rate (melt extraction rate) decreases over time, so that the later lavas spend more time in the crust and thus have more time to evolve and interact with the surrounding wallrock. Additionally, the location of the assimilation process may change over time. Prolonged exposure to melt progressively heats up wallrock until it reaches its solidus temperature and starts melting. With a continuous but not necessarily constant melt flux, the location of the solidus migrates upwards through the crust over time so that later melts interact with wallrock higher in the transport column (Fig. 3.10). In this scenario, the latest melts would last equilibrate higher in the crust, with correspondingly lower temperature and lower MgO (e.g., Rubin and Sinton, 2007) than early melts that equilibrated at greater depths. The extent to which this scenario is reasonable will require careful consideration of the rates involved in the various processes, including heat exchange, melt velocity, mineral dissolution, and possibly diffusion.

Most existing evidence from oceanic gabbros indicates precipitation of clinopyroxene during melt-wallrock interaction, with dissolution of olivine and plagioclase (e.g., Meyer et al., 1989; Natland and Dick, 1996; Coogan et al., 2000; Kvassnes and Dick, 2000; Lissenberg and Dick, 2008), i.e., the opposite of the process we propose here. These studies examined the final stage in evolution of oceanic gabbros: the freezing of late-stage melts with precipitation of clinopyroxene, with or without simultaneous dissolution of olivine and plagioclase. However, when there has been a

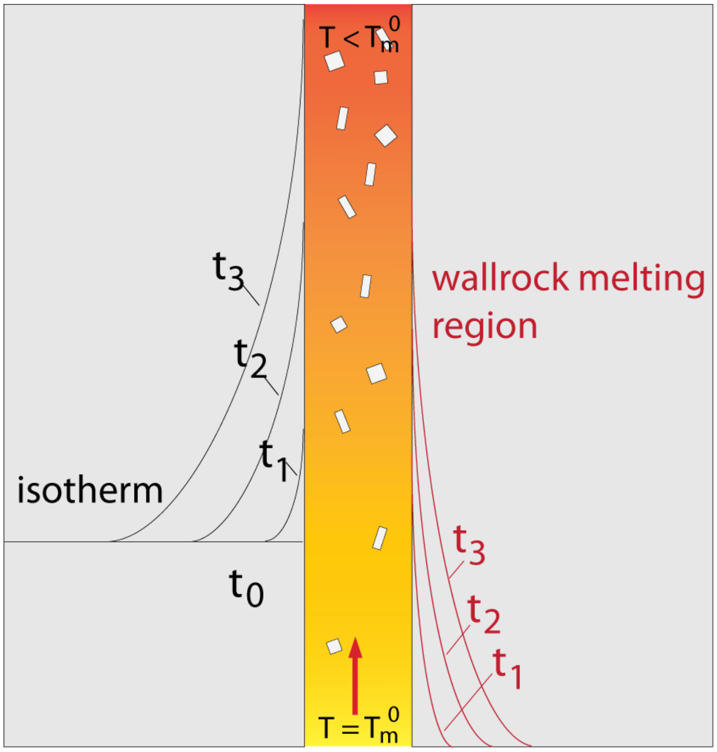

Figure 3.10 Schematic representation of the MAFC process that couples extent of crustal assimilation and crystal fractionation during a period of continuous magma supply; t_1, t_2, t_3 represent progressively later times. Gray-shaded region is wallrock and the central region is a schematic representation of a melt pathway with fractionating solids that is hotter at the base ($T = T_m^0$) than at the top ($T < T_m^0$). Lines on left side of melt pathway show evolution of a hypothetical isotherm; lines on right side show schematically how the wallrock solidus varies with time. With progressive supply of hot magma, the region of wallrock affected by partial melting expands upward and slightly outward with time. At later times, wallrock higher in the melt pathway will reach its solidus temperature. In this way, later lavas may have last equilibrated at lower magma temperatures and interacted with the most crust along its path.

long time between eruptions and the crust has solidified, influx of magma into the system during new magmatic episodes might reverse this process, preferentially melting the wallrock clinopyroxene and precipitating magmatically-derived olivine ± plagioclase.

3.5.2 Lava shields and fissure eruptions in Iceland

Thjófahraun's geochemical variations and mineralogical progression with time are broadly consistent with evolution in a shallow magma chamber. Early lavas contain small amounts of olivine with little to no plagioclase. As the eruption continues over some months to years, the magma carries a greater proportion of plagioclase, consistent with a single body of magma crystallizing at low pressure. The last lavas erupted are plagioclase-phyric ‘a‘ā flows with generally lower MgO (Fig. 3.5). Assuming this eruption taps a batch of resident magma, the minimum volume of reservoir melt is >1 km^3. Probably there was much more: estimates of the intrusive vs. extrusive volumes at Krafla in Iceland (Tryggvason, 1984, 1986; Sigurdsson, 1987), as well as geologic observations at Hess Deep (Stewart et al., 2005) and along the SEPR (Bergmanis et al., 2007), indicate less than half of the magma that exists in shallow magma chambers ever reaches the surface during rifting events. In simple models of a magma chamber filling and pressurizing prior to eruption, the erupted volume is a minimum constraint on the magma overpressure – that is, the amount of excess magma necessary to initiate diking to the surface – not the total volume of melt resident in the chamber. By some estimates, typical crustal reservoir volumes may be as high as 30 times the volume of erupted magma (Blake, 1981; Head et al., 1996). Once diking has reached the surface, magma can erupt fairly quickly, resulting in higher eruption rates, as indicated by lava morphology of the Thjófahraun flow field.

The nature of chemical heterogeneity in Lambahraun suggests that the erupted magmas may never have resided in a large, well-mixed magma chamber. Clinopyroxene barometry and major element chemistry indicates that some magma chambers in Iceland may be as deep as the lower crust or even upper mantle (Maclennan et al., 2001, 2003a,b). In the case of Lambahraun, if there is melt storage near the surface, it must be limited in extent and host little magma mixing. We envision crustal melt storage under Lambahraun as an interconnected network of many smaller melt bodies (pores to small melt lenses and sills), which primarily serve as pathways for melt migration rather than long-term storage (Fig. 3.11). In this scenario, the eruption rate may be dependent on the rates at which melt can be extracted from the mantle and migrate upwards through the crust. This is fundamentally different from a fissure eruption like Thjófahraun that is fed from a shallow chamber, in which the eruption proceeds relatively quickly once enough overpressure exists to initiate diking to the surface, erupting the excess magma and relieving the pressure in the chamber.

Although we have no direct evidence for a deep magma chamber beneath Lambahraun as has been posited for some other eruptive units in Icelandic (Maclennan et al., 2001, 2003a,b), if there were melt storage near the crust-mantle boundary, an eruption from such a depth could result in a much greater volume of extrusive lava than from a shallow crustal reservoir. The overpressure required to reach the surface from near the crust-mantle boundary is greater, such that more eruptible magma must accumulate prior to diking in order to reach the surface and result in an eruption. Lava shield eruptions

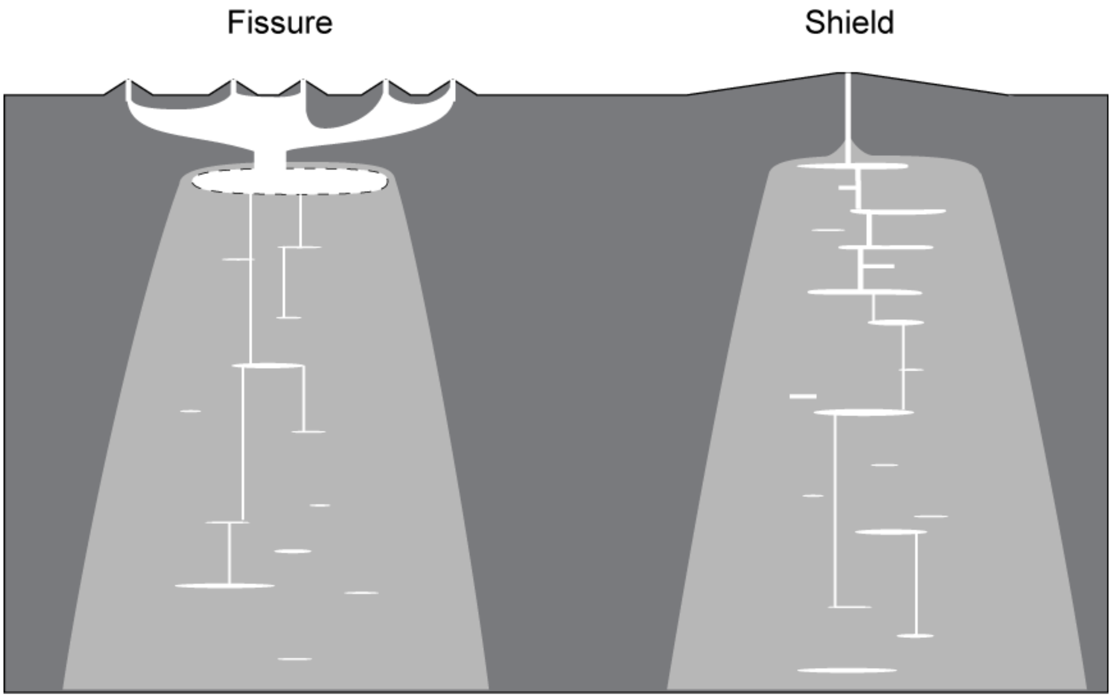

Figure 3.11 Schematic representation of plumbing systems for Icelandic fissure and lava shield eruptions; sections drawn parallel to the rift zone axis. Evidence suggests that fissure eruptions are fed by shallow, moderately well-mixed magma chambers. In contrast, chemical variations in some lava shields are inconsistent with the presence of well-mixed reservoirs. Instead, we envision crustal melt storage under Lambahraun as an interconnected network of many smaller melt bodies (pores to small melt lenses and sills), which primarily serve as pathways for melt migration rather than long-term storage. Drawing not to scale.

might begin as fissure-fed lava flows in the initial stages of the eruption when the driving pressure is high, gradually closing down to a few discrete centers of eruption, and eventually a single source vent (Rossi, 1996). It is this last stage in the eruption chronology, with its relatively low effusion rates but steady supply of magma that builds the classical lava shield morphology. This continued supply of magma through the crust and relatively low melt velocities could provide ideal conditions for melt-wallrock interaction.

Lambahraun is not the only postglacial lava shield in the WVZ to show signs of crustal interaction. Although most other WVZ units are not as completely analyzed, a number of other shields exhibit the same geochemical signature of increasing CaO and incompatible element compositions with decreasing MgO, most notably Thingvallahraun, Hallmundarhaun and Leggjabrjótur (see Fig. 3.12; chemical data from Sinton et al., 2005). Although detailed study of the chemical and mineralogical variation in these units has not been undertaken, we consider them likely candidates for this process. All of these shields have large erupted volumes (6.3-10.8 km^3). Notably, we have not found the geochemical signature of crustal interaction in any of the fissure eruptions, although some lack sufficient data to fully describe geochemical evolution paths.

Icelandic fissure eruptions tend to occur with higher average effusion rates than the longer-lived shield eruptions, building rows of spatter cones and producing a higher proportion of ‘a‘ā units. It is possible that melt transport is too fast (or too short-lived) to heat the wallrock sufficiently to induce significant melting during fissure eruptions. In this scenario, crustal interaction might occur only in longer-lived, relatively low-effusion rate eruptive style of the large lava shields in the WVZ. However, because fissure

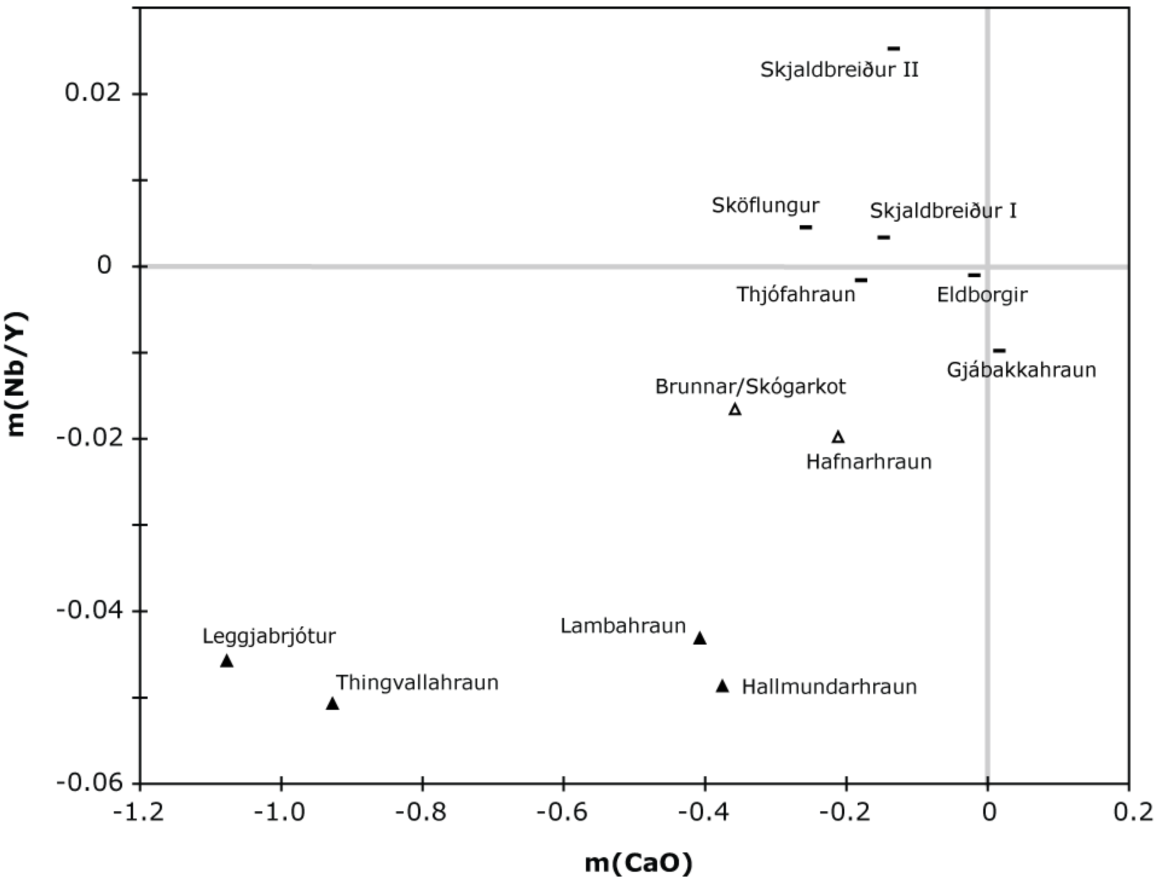

Figure 3.12 *m*(Nb/Y) vs. *m*(CaO) for units in the Western Volcanic Zone with at least 10 whole-rock sample analyses, where *m* denotes the slope of regression lines plotted against the total range of MgO for each unit. Strongly negative slopes in Nb/Y (and other similar incompatible element ratios, not shown) vs. MgO generally correlate with steeper CaO vs. MgO variation for some large lava shields in the Western Volcanic Zone (solid triangles). These are the chemical signatures of the MAFC process identified for the Lambahraun lava shield. See text for discussion.

eruptions are probably fed by moderate-sized crustal reservoirs, it is equally likely that any chemical signature of early crustal interaction was at least partially obscured during subsequent storage and mixing in shallow magma chambers. This hypothesis can explain some of the scatter in the Thjófahraun data, as incomplete or partial mixing may preserve some of the geochemical heterogeneity, which is then over-printed by the signature of subsequent crystallization in the magma chamber. Taken together, our study supports the suggestion that Icelandic fissure eruptions represent short-lived, high-effusion eruptions that tap shallow melt reservoirs, while lava shields may lack shallow reservoirs and avoid the mixing that occurs in them.

Evidence suggests that crustal assimilation may be widespread in the Western Volcanic Zone, and could be more prevalent than the current data allow us to see. While the thick crust in Iceland might enhance crustal interaction processes, similar processes have been suggested to play a role in other mid-ocean ridge settings even where the crust is not unusually thick (Meyer et al., 1989; Natland and Dick, 1996; Coogan et al., 2000; Bédard et al., 2000; Kvassnes and Dick, 2000; Dick et al., 2002; Kvassnes, 2004; Kvassnes and Grove, 2008; Lissenberg and Dick, 2008) as well as at other hotspots (e.g., Pietruszka et al., 2009). We also emphasize that the process of crustal interaction can significantly alter major element concentrations and trace element ratios, parameters that are commonly used to infer melting conditions in many MORB studies. Although the MAFC process described in this paper is closely tied to extent of differentiation as reflected in MgO contents, we also note that early crustal interaction and the chemical modifications it produces can be obscured by mixing in shallow magma chambers if shallow melt aggregation precedes eruption. These results suggest that inferences on melting conditions and source compositions may only be reliable for the least differentiated lava compositions from individual eruption sequences.

3.6 Conclusions

Thjófahraun and other fissure eruptions in Iceland represent short-lived, high effusion rate eruptions from an extant crustal reservoir. Early phases of Thjófahraun's eruption are dominated by olivine-phyric pāhoehoe lava with sample chemistry covering the full range of Thjófahraun's compositional variation, while later flow units transition to small-volume, plagioclase-phyric ‘a‘ā flows that tend to be more uniformly differentiated. Mineralogical and compositional variations are consistent with evolution in a shallow magma chamber.

The 7.3 km^3 Lambahraun lava shield is composed of dense pāhoehoe lava, indicating a relatively low effusion rate over a long-lived eruption. Spatial distribution of lava compositions suggests that the erupting magma became progressively more differentiated and enriched in incompatible elements with time during the eruption. Evidence for plagioclase accumulation is present in outcrops, thin section, and in the chemistry of some samples. Whole-rock compositional variations from Lambahraun are inconsistent with simple evolution in a shallow magma chamber, exhibiting increasing CaO and Nb/Zr with decreasing MgO content and incompatible element enrichments greater than predicted by crystal fractionation alone. The correlation of this enrichment with increasing differentiation and time during the eruption lead us to favor a process of concurrent wallrock assimilation and crystallization during melt migration through the crust, and we develop a MAFC model to explore the chemical effects of this process.

The most evolved Lambahraun compositions are consistent with a total addition of 3-5 % anatectic melt derived from less than 5 % melting of the crust to the Lambahraun magmatic system. Similar geochemical characteristics exist in several other WVZ lava shields, but not in the available data from fissure eruptions. Crustal interaction might be more likely in long-lived, voluminous shield eruptions, where slow effusion could be related to low melt propagation velocities through thick crust.

Acknowledgements

We wish to thank Melissa Rotella and JoAnn Sinton for assistance in the field and Karl Grönvold for his help and insight at many stages of this project, including extraordinary transportation services. Many thanks to Eric Hellebrand for his assistance with the microprobe and XRF analyses, Chuck Fraley for ICP-MS data collection, and JoAnn Sinton for thin section preparation. We are also grateful to Rósa Ólafsdóttir for providing digitized topographic contours and a digital elevation model of the WVZ. This manuscript was greatly improved by thoughtful reviews by Laurence Coogan and John Maclennan. This research was supported by National Science Foundation grant OCE05-24922.

CHAPTER 4

THERMAL MODEL OF FRACTIONAL CRYSTALLIZATION AND CRUSTAL ASSIMILATION DURING MAGMA MIGRATION

4.1 Abstract

We model the thermal effects of steady, continuous magma flow through a mafic crust in order to examine the conditions under which crustal assimilation during magma ascent might occur. We use a finite difference approximation in two-dimensions in which heat is advected along the crustal conduit by magma flow and conducted away from the conduit into the surrounding host rock. Magma cools and crystallizes during its ascent to the surface, its eventual erupted crystal fraction being dependent on the conduit geometry and magma velocity. This crystallization produces latent heat, which in turn is an important heat source term that contributes to partial melting of the surrounding wallrock. The overall contribution of anatectic melt to erupted lava compositions depends on magma transport rates, conduit geometry, initial geothermal profile of the host rock, and the time over which magma supply to the system is sustained. We find anatectic melting is likely a significant process in eruptions with relatively low magma velocities but long, sustained eruption durations (years to decades). Under these conditions, melt-wallrock interaction during magma ascent through mafic crust can have important geochemical consequences for the erupted lavas as the incorporation of low-degree partial melts leads to enrichments in highly incompatible trace elements. These results are in keeping with geochemical observations at large-volume lava shields in the

Western Volcanic Zone of Iceland, which produce low-effusion rate pāhoehoe lavas during long-lived eruptions sustained over decades, with increasing degrees of incompatible element enrichments with increasing magma differentiation through time.

4.2 Introduction

The reaction of magma with its surroundings during storage and migration to the surface is an often-neglected process that might be important in the geochemical evolution of basaltic magmas. Evidence for melt-wallrock interactions at mid-ocean ridges comes primarily from lower crustal rocks, where coexisting minerals are commonly not in chemical or textural equilibrium (e.g., Elthon, 1987; Meyer et al., 1989; Elthon et al, 1992; Natland and Dick, 1996; Bédard et al., 2000; Coogan et al., 2000; Dick et al., 2002). In Iceland, gabbroic xenoliths in basalt show evidence for partial melting and mineral resorption (Larsen, 1979; Hansteen, 1991; Gurenko and Sobolev, 2006). In addition, some lava sequences in Iceland and other hotspots show trace element and isotopic enrichments that have been interpreted as reflecting crustal assimilation (Muehlenbachs et al., 1974; Óskarsson et al., 1982; Condomines et al., 1983; Hémond et al., 1988; Nicholson et al., 1991; Maclennan, 2008; Halldórsson et al., 2008; Pietruszka et al., 2009; Eason and Sinton, 2009).

The reaction of melt with its surroundings is likely common in hot crystal mush environments associated with magma chambers (Marsh, 1995, 1998) or in the lower crust, where evidence suggests melt migration occurs as reactive porous flow through a crystal mush (e.g., Sinton and Detrick, 1992; Coogan et al., 2000; Lissenberg and Dick, 2008). Recent melting experiments suggest oceanic gabbros in the lower crust should melt readily when exposed to hot ascending magmas (Kvassnes and Grove, 2008). Melt-wallrock interaction is most pronounced and most easily identified when the host wallrock has a significantly different composition than the intruding magmas. However, at mid-ocean ridges, the magmas and the crust through which they ascend should be broadly similar in composition, and the geochemical signature of wallrock assimilation may be difficult to distinguish from the effects of variations in source melting. In addition, well-mixed axial magma chambers can reduce chemical heterogeneity, making the subtle petrologic indicators of this process even more elusive (Rubin et al., 2009). Given the common practice of inverting the chemical composition of lavas to constrain their source composition, melting history and differentiation path, it is important to assess the potential influence of crustal assimilation on the system.

Simple phase equilibria treatments of the problem illustrate the potential for melt-wallrock interaction and its possible effects on the resulting eruptive products (Bowen, 1922a, 1922b, 1928; Keleman, 1990). Modern thermodynamic treatments of the problem generally focus on wallrock assimilation in the context of magma chambers, where the latent heat of crystallization is an important driving source for melting the chamber walls (Allègre and Minster, 1978; Taylor et al., 1979; Taylor, 1980; Grove and Kinzler, 1986). Some models (e.g., DePaolo, 1981; Aitcheson and Forrest, 1994) have examined the compositional effects of assimilation and fractional crystallization (AFC) on the resulting magmas, while others have incorporated thermal constraints in an attempt to develop thermodynamically consistent models (Reiners et al., 1995; Edwards and Russell, 1998; Spera and Bohrson, 2001).

Although the majority of work on the geochemical consequences of wallrock assimilation has focused on magma chambers, numerical models have shown that magma flowing through conduits in the crust can result in thermal erosion of the wallrock (Huppert and Sparks, 1989; Bruce and Huppert, 1990). However, the extent to which wallrock meltback during magma ascent might influence the geochemistry of erupted lavas is still largely unknown.

4.2.1 Lambahraun lava shield

Eason and Sinton (2009) argued that the chemical evolution of the Lambahraun lava shield in the Western Volcanic Zone (WVZ) of Iceland reflects interaction during melt migration through the crust. Erupted basalts at Lambahraun range from 6.6-9.7 wt. % MgO; field relations suggest an evolution of lava compositions to lower MgO contents with time during the eruption, which, based on the preponderance of low effusion-rate pāhoehoe lava, likely lasted several decades. As lava MgO decreases, CaO and highly incompatible trace elements such as Nb, Zr, La and Ce exhibit enrichments greater than predicted by simple crystal fractionation (Fig. 4.1). Geochemical modeling indicates that Lambahraun major and trace element variations can be explained by small but progressively increasing amounts of assimilation (up to 3-5 % of total magma volume accounted for by anatectic melt) of a low degree (< 0.1-5 %) partial melt of an average WVZ basaltic whole-rock composition (Eason and Sinton, 2009). The proportion of assimilant to primary magma increases with increasing crystal fractionation, suggesting

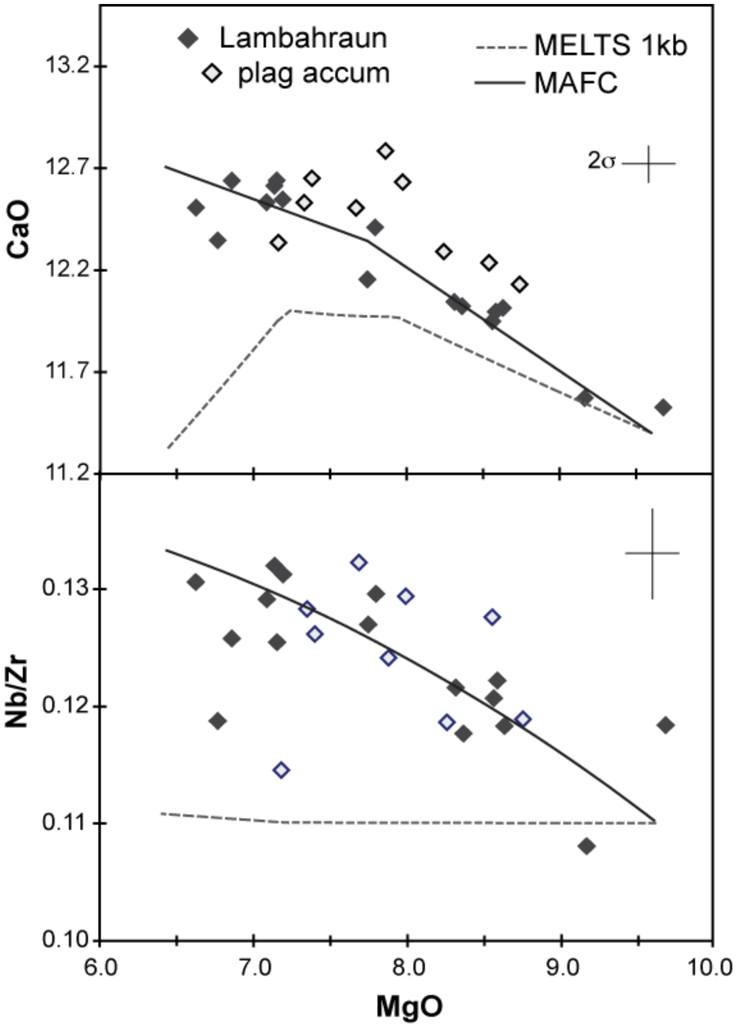

Figure 4.1 Variation of CaO and Nb/Zr for lava samples from the Lambahraun lava shield, modified from Eason and Sinton (2009). Open symbols are samples whose compositions have been corrected for the effect of plagioclase accumulation (see Chapter 3 for description). Crosses show 2σ uncertainty in the plotted data. Dashed line is 1 kb fractionation trend predicted by MELTS for Lambahraun (see Chapter 3 for details of calculation). Solid line is the MAFC model calculation from Chapter 3 that simulates crustal interaction during melt migration by "refreshing" the wallrock composition in each step.

the two may occur concurrently as in AFC. However, AFC models of a magma chamber do not reproduce the observed Lambahraun incompatible element variations because progressive melting of a single wallrock leads to a decreasing influence of these elements (e.g., Nb, Y, Zr) (Eason and Sinton, 2009). Lambahraun whole-rock data instead show a continued enrichment in incompatible elements over time relative to that predicted by simple crystal fractionation, with the greatest increases in the most highly incompatible elements. Because the element enrichments are proportional to $K_d^{cpx\text{-}liq}$, Lambahraun evolution requires continual addition of a clinopyroxene-dominated anatectic melt rather than whole-scale digestion of wallrock minerals (Eason and Sinton, 2009). Several other large (> 6 km^3), long-lived lava shields in the WVZ exhibit similar geochemical signatures (Eason and Sinton, 2009), indicating anatectic melting may be a common feature of these high-volume, long duration eruptions.

One way to increase the contribution of the most highly incompatible elements without greatly affecting more compatible element concentrations is to “refresh” the wallrock composition. This could be done either in a convecting magma chamber where pieces of the partially melted, solid residue of the surrounding wallrock are eroded and removed over time, allowing magma access to fresh, unmelted wallrock, or in a scenario in which the melt is migrating through new host material (such as ascent through a conduit, or during porous melt flow). Observations of gabbros provide abundant evidence for the latter case, although little is known about the thermal conditions under which this may take place, or what the geochemical effects might be on the resulting magmas. A purely geochemical model for assimilation and fractional crystallization during magma migration (MAFC) developed in Eason and Sinton (2009) indicates this process can explain observed compositional variations in Lambahraun, but the thermal feasibility of this process remains to be evaluated.

The existing Lambahraun data provide information on total magma flux, eruption duration, and temporally-correlated compositional variations that place constraints on the degree of crystal fractionation and anatectic melt contribution over time. Lambahraun lava shield consists of ~7.3 km^3 of dense pāhoehoe lava, which likely formed at relatively low average effusion rates (5-10 m^3/sec, from Rowland and Walker, 1990; Rossi, 1996), giving an estimated eruption duration of several decades. In this paper, we develop a thermal model to explore the conditions under which crustal assimilation may play an important role in the formation of lava shields, with implications for magma flow rates, eruption durations and the compositions of erupted basalts.

4.3 Model setup

We use a thermal model in order to examine the first-order effects of magma migration through mafic crust and the thermal consequences of heat exchange between the magma and its surrounding wallrock. Our model assumes instantaneous emplacement of magma with temperature T_m at time $t = 0$ in a linear conduit with width w and height h (Fig. 4.2). Heat is transported in the magma by advection along the direction of flow and conduction both in and across the direction of flow and in the surrounding wallrock. The thermal evolution of this system is governed by the advection-diffusion equation with additional terms for the enthalpy associated with crystallization and fusion,

$$\frac{\partial T}{\partial t} = \kappa \nabla^2 T - \mathbf{u} \cdot \nabla T + \frac{L_c}{c_{p.m}} \Psi - \frac{L_f}{c_{p,a}} \frac{\partial \xi}{\partial t} \ , \tag{4.1}$$

where κ is the thermal diffusivity, **u** is the magma velocity, L_c and L_f are the enthalpies of crystallization and fusion, $c_{p.m}$ and $c_{p,a}$ are the average isobaric heat capacities of the magma and wallrock, and ξ is the extent of partial melting in the wallrock. The rate of crystallization, Ψ, is the material time derivative of X, the extent of crystallization, which is assumed to vary linearly below the liquidus, T_{liq},

$$\Psi = \frac{DX}{Dt} = \frac{D}{Dt}\left[\frac{T_{liq} - T}{L_c / c_{p,m}}\right]. \tag{4.2}$$

We assume a linear depth-dependent liquidus temperature derived from MELTS (Ghiorso and Sack, 1995; Smith and Asimow, 2005) modeling of a high-MgO Lambahraun lava composition. With T in °C and depth z in km,

$$T_{liq} = 3.25z + 1220\,°\text{C}. \tag{4.3}$$

Table 4.1 Model parameters

Parameter	Description	Value	Units
κ	thermal diffusivity	10^{-6}	$m^2\ s^{-1}$
L_c	latent heat of crystallization	600	$kJ\ kg^{-1}$
$c_{p.m}$	average isobaric heat capacity of magma	1000	$J\ kg^{-1}\ °C^{-1}$
ρ	density	2900	$kg\ m^3$
$\partial T_{geo} / \partial z$	geothermal gradient	40	$°C\ km^{-1}$
L_f	latent heat of fusion (wallrock)	600	$kJ\ kg^{-1}$
$c_{p,a}$	average isobaric heat capacity (wallrock)	100	$J\ kg^{-1}\ °C^{-1}$

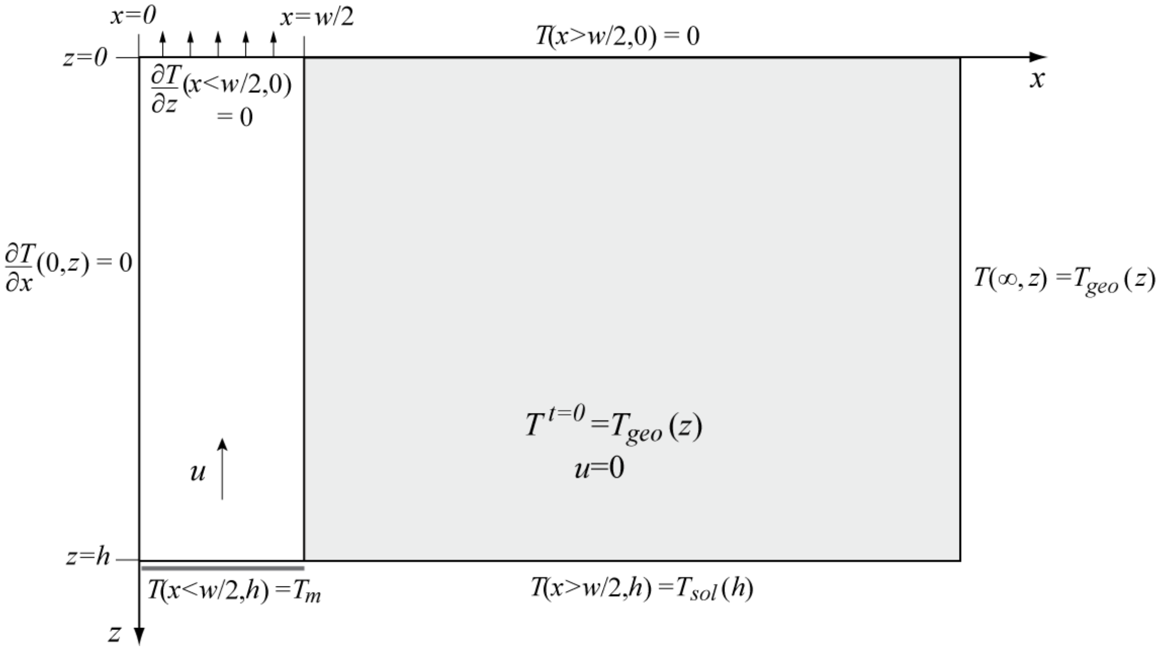

Figure 4.2 Schematic diagram of the model setup. Magma conduit (unshaded region) has dimensions w by h in a planar halfspace. Magma has a vertical velocity of u with an initial temperature of T_m. Wallrock (shaded region) is set initially to a geothermal temperature profile of 40°C/km.

The initial wallrock temperature is set by a geothermal gradient ($\partial T_{geo} / \partial z$) of 40°C/km. Although geothermal gradients in Iceland can range to much higher values, permeability within the neovolcanic zones, such as the WVZ, is high and local gradients are strongly affected by ground water flow and difficult to characterize (Arnórsson et al., 2008). The last prior eruption in the area immediately surrounding Lambahraun was >1000 yrs before the lava shield eruption, and we have therefore chosen a conservative estimate for the temperature profile in the upper crust.

For the small values of *dt* (the model time step) during which a batch of magma resides at any given depth, wallrock melting is inherently a disequilibrium process. Experimental melting rates for gabbro are on the order of ~0.01 mm/hr for temperatures of ~1240°C (Kvassnes and Grove, 2008). Equilibrium partial melt fractions are therefore inappropriate for the small values of *dt* required for model stability (on the order of 10-100 s for most run parameters). Instead, we view predicted equilibrium melt fractions as a snapshot of the total potential melting capacity of the wallrock at a particular moment in time. How much of that melting actually occurs on timescales over which it can be effectively assimilated into a particular batch of magma depends on how long that magma batch remains in contact with the wallrock (i.e., inversely related to *u*).

To calculate how much melting occurs on short timescales, we assume a melting rate that depends on T and the mineral phases involved, as well as a melting surface geometry. The surface area available to melt in turn depends on mineral grain size and shape, which are likely to be quite variable, and the packing efficiency, which has implications both for the mineral contacts and the porosity of the rock. One must also assume an extraction efficiency, which depends on the degree to which melt films are compacted and transported into the conduit (Philpotts and Asher, 1993; Philpotts and Dickinson, 2000).

Grain size in oceanic gabbros varies widely, from < 1 mm up to pegmatitic veins with m-scale grains, but most are in the mm-cm range (e.g., Dick et al., 1991). Without assuming a specific grain morphology or packing geometry, material with a 1 mm grain size has on the order of 10^4 melting surface area per cubic m of volume; similarly, surface area per cubic m consisting of 1 cm grains is ~ 10^3 m^2/m^3. We therefore estimate the mass of anatectic melting (M_A) that occurs in the wallrock with order of magnitude variation in grain size on small timescales as

$$\frac{\partial M_A}{\partial t} = \rho \frac{\partial V_A}{\partial t} = \rho\left(\mu S \frac{\partial V_w}{\partial t}\right), \tag{4.4}$$

where V_A is the volume of anatectic melt, V_w is the volume of wallrock with $T \geq T_{sol}(z)$, S is the surface area per unit volume, ρ is the material density and μ is the melting rate, which we assume to be constant at 0.01 mm/hr for oceanic gabbros (Kvassnes and Grove, 2008). For runs presented in this paper, we assume a grain size of 1 cm.

Because melting is not an equilibrium process, we have simplified the problem by using a constant melting rate that is not dependent on temperature, yet the total extent of partial melting ξ is still bound by the equilibrium partial melting fraction F, which we assume to be linear with T.

$$\xi = \sum_t \frac{M_A}{M_w} \leq F, \tag{4.5}$$

where

$$F = \frac{T - T_{sol}}{L_f / c_{p,a}}. \tag{4.6}$$

For numerical simplicity, we also assume a melt extraction efficiency of one, so that all anatectic melt produced is instantaneously extracted. For the wallrock solidus, we use an average solidus profile with depth for basalts,

$$T_{sol} = 3.25z + 1050°\text{C}. \tag{4.7}$$

Because we are interested in the composition of the erupted magma that has passed through this system, we track the average erupted crystallinity ($\overline{X}_C$) as a function of time by averaging the extents of crystallization at the top of the conduit across its width. The total amount of anatectic melt added to a given packet of magma during its ascent is calculated by summing the mass of anatectic melt (M_A) stripped from the wallrock (assuming 100 % melt extraction) for each vertical step dz of the magma's ascent, such that the total proportion of anatectic melt to the total erupted magma at the top of the conduit (X_A) is

$$X_A(t) = \frac{M_A(t)}{M_m} = \frac{M_A(t)}{\rho w dz}, \tag{4.8}$$

We solve equations (4.1)-(4.7) in two steps. The first step solves for heat conduction using a standard Eulerian finite difference method. With respect to locally Cartesian coordinates z (vertical and parallel to flow) and x (horizontal and perpendicular to flow) (Fig. 4.2), equation (4.1) in a planar halfspace and with zero velocity reduces to

$$\frac{\partial T}{\partial t} = \kappa \left(\frac{\partial^2 T}{\partial x^2} + \frac{\partial^2 T}{\partial z^2} \right). \tag{4.9}$$

We solve this two-dimensional parabolic partial differential equation using forward differencing in time with accuracy $O(\Delta t)$ and central differencing in space with accuracy $O(\Delta x^2 + \Delta z^2)$. The corresponding finite difference equation is

$$T_{ij}^{n+1} = T_{ij}^{n} + \kappa \Delta t \left(\frac{T_{i+1,j}^{n} - 2T_{ij}^{n} + T_{i-1,j}^{n}}{\Delta z^2} + \frac{T_{i,j+1}^{n} - 2T_{ij}^{n} + T_{i,j-1}^{n}}{\Delta x^2} \right). \tag{4.10}$$

Calculations are performed in cross section on a two-dimensional grid with a maximum horizontal spacing of 0.05 m, with boundary conditions (see also Fig. 4.2)

$$T(x = \infty, z) = T_{geotherm}(z) \tag{4.11a}$$

$$\frac{\partial T}{\partial x}(x = 0, z) = 0 \tag{4.11b}$$

$$\frac{\partial T}{\partial z}(x < w/2, z = 0) = 0 \quad , \tag{4.11c}$$

$$T(x < w/2, z = h) = T_m \tag{4.11d}$$

$$T(x > w/2, z = 0) = 0 \tag{4.11e}$$

$$T(x > w/2, z = h) = T_{sol}(h) \tag{4.11f}$$

where $w/2$ is the width of the conduit in the halfspace. We choose the total height of the melt pathway h to be 28.6 km, where the chosen geothermal gradient intersects the solidus.

The second step of our solution to (4.1-4.7) solves the advective and latent heat terms. For simplicity, we ignore the effects of shear flow and assume a constant velocity profile along the height and across the width of the conduit. Advection is treated by shifting temperatures upward by the appropriate Δz traveled by the magma in each time step Δt. In order to prevent numerical diffusion, the grid spacing is controlled such that this shift is a discrete number of grid points. Crystals are also assumed to move with the magma, a simplification that does not allow for crystal fractionation. Components of the code were verified against solutions for the instantaneous heating of a semi-infinite half-space and the Stefan problem, which takes into account latent heat (Turcotte and Schubert, 1982).

We do not consider the initial formation of the conduit, which would require a description of the solid mechanics of dike propagation (e.g., Spence and Sharp, 1985; Lister, 1990). This process is likely to be fast relative to the longer eruptive timescales we are investigating. Similarly, we do not consider the driving force of the eruption (i.e., magmatic overpressure), which has been addressed in numerous other numerical models of conduit flow (e.g., Blake, 1981; Parfitt and Head, 1993; Buck et al., 2006). We assume sufficient magmatic supply to sustain the eruption over long timescales.

The assumed constant velocity profile across the width of the conduit is an obvious simplification of real flow behavior, which should be slower at the edges of the conduit than the middle due to the effects of shear flow. While other numerical models have explored the effects of shear flow on conduit behavior, particularly with regard to fissure blocking (e.g., Delaney and Pollard, 1982; Bruce and Huppert, 1990), we simplify the problem with a constant velocity profile across the conduit. In order to test the

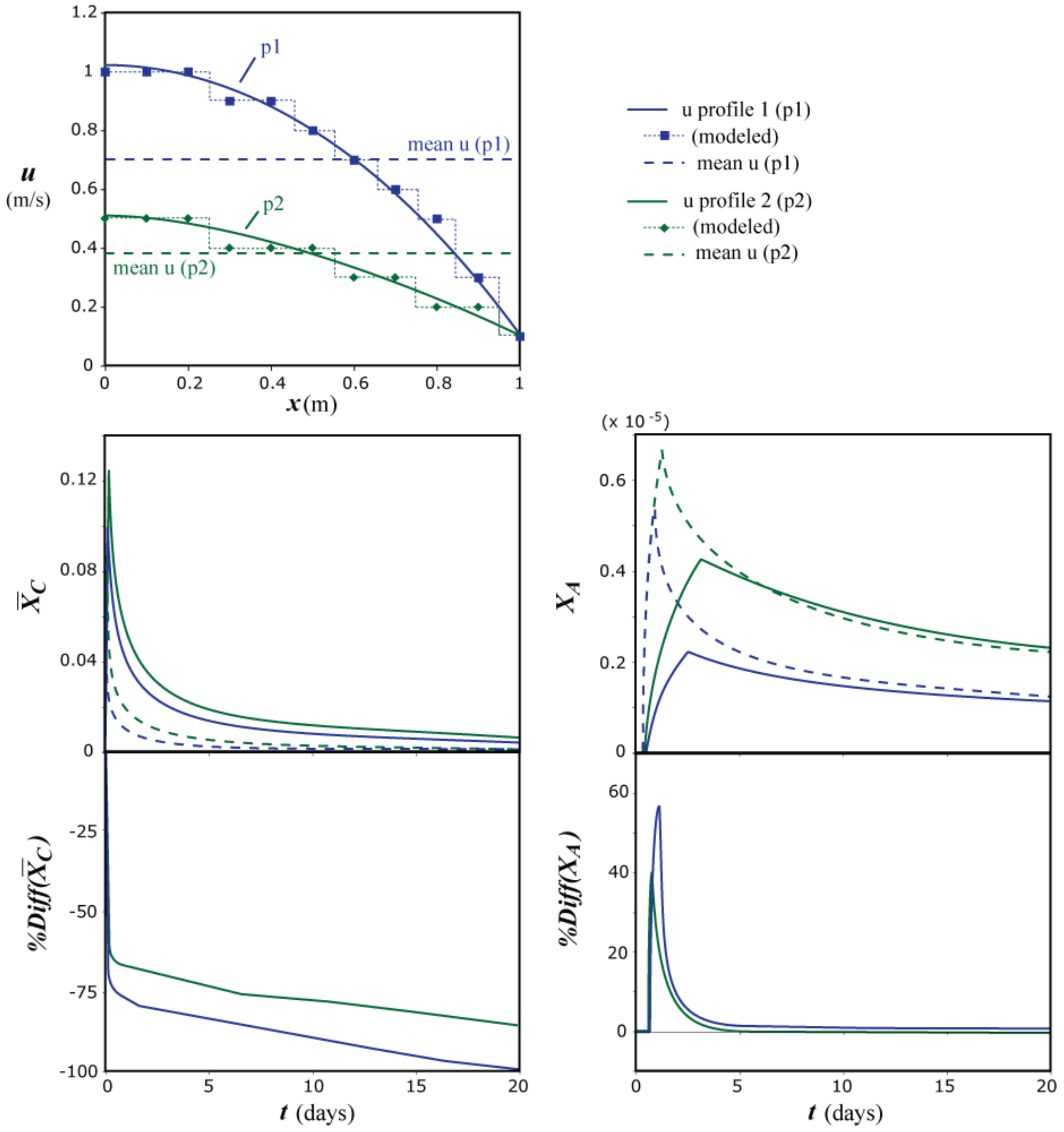

Figure 4.3 Examples comparing parabolic velocity profiles against constant velocity profile assumption for a 1 m x 3 km conduit. The mean velocity of a given parabolic profile yields comparable values of X_A (< 5% difference at $t >> h/u$ for most test runs), while the average crystallization for the constant velocity profile tends to be significantly lower (see text for discussion).

potential effects of this assumption, we have run the model with different discretizations of parabolic velocity profiles (example runs shown in Fig. 4.3). The results of this comparison indicate that the anatectic melt contribution (X_A) for the constant-velocity profiles is similar to that of the mean speed of the parabolic velocity profiles at large t, whereas the average erupted crystallinity ($\overline{X}_C$) tends to be significantly lower for the constant mean velocity profile than for the parabolic profile. Although latent heat produced by crystallization plays a role in determining X_A, the lower overall extent of crystallization in model runs with parabolic velocity profiles apparently has little long-term effect on the magnitude of X_A relative to constant velocity runs, probably because crystallization is even more preferentially concentrated close to the conduit wall where the flow is slower in parabolic velocity runs.

4.4 Results and discussion

In Fig. 4.4, we plot example snapshots of the system's evolution in time. In the initial stages of the model evolution ($t < h/u$), the temperature in most of the conduit is controlled primarily by heat conduction (Fig. 4.4b), the loss of heat to the wallrock occurring much more rapidly than heat advection. At later times (Fig. 4.4c, d, $t > h/u$), as the temperature differential between the wallrock and the magma decreases, advection begins to play a larger role, and the continued introduction of heat into the bottom of the system (recharging the magma in the conduit) results in gradual heating of the entire conduit, with consequences for both the crystallinity of the eruptive magmas and the temperature of the wallrock. As magma and heat continue to flow through the conduit,

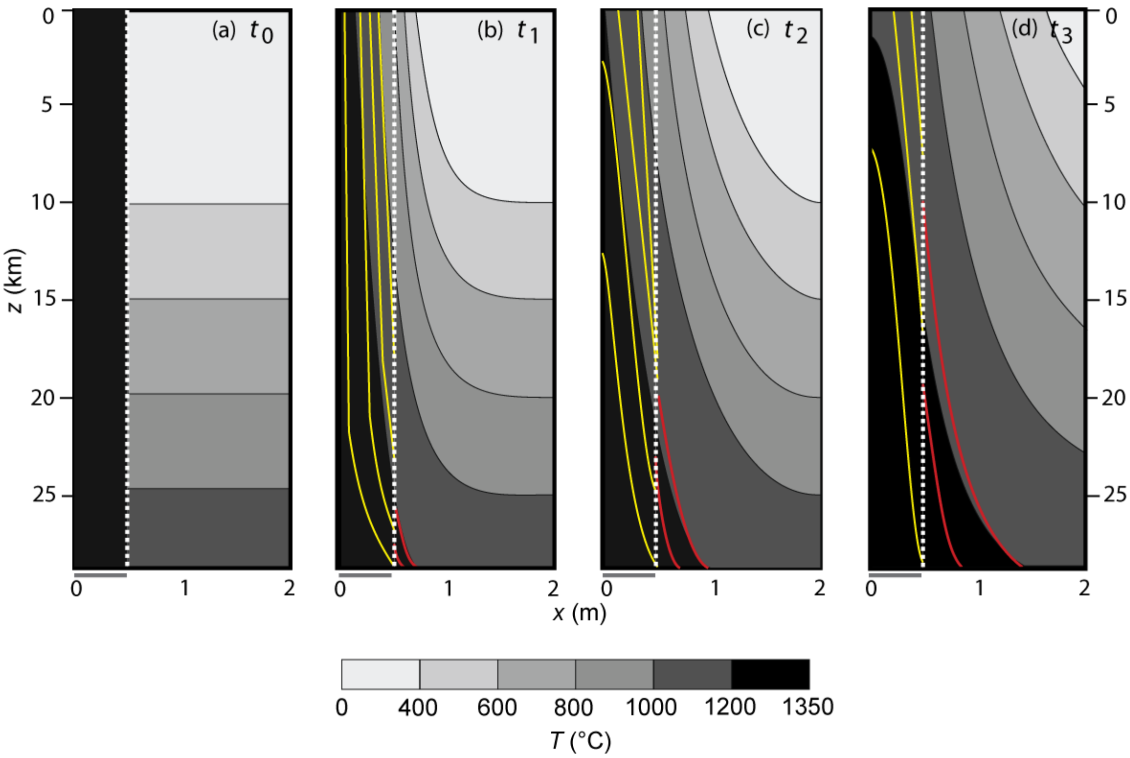

Figure 4.4 Evolution of conduit melting model. Example shown has a velocity of u = 0.1 m/s. Shading denotes temperatures. Yellow lines in the interior of the conduit are contours of crystal content (contoured at 0.01, 0.05, 0.10, and 0.20), red lines in the wallrock denote extents of partial melting (F, contoured at 0.01, 0.02). (a) Initial conditions of the model; magma is instantaneously emplaced with an initial temperature of T_m at time $t = 0$. (b) For times $t < h/u$, the temperature profile of the conduit is controlled primarily by heat conduction. (c)-(d) For times $t > h/u$, the temperature differential between the wallrock and the magma decreases and advection begins to play a dominant role. The melting region continues to expand with time as heat is advected into the system.

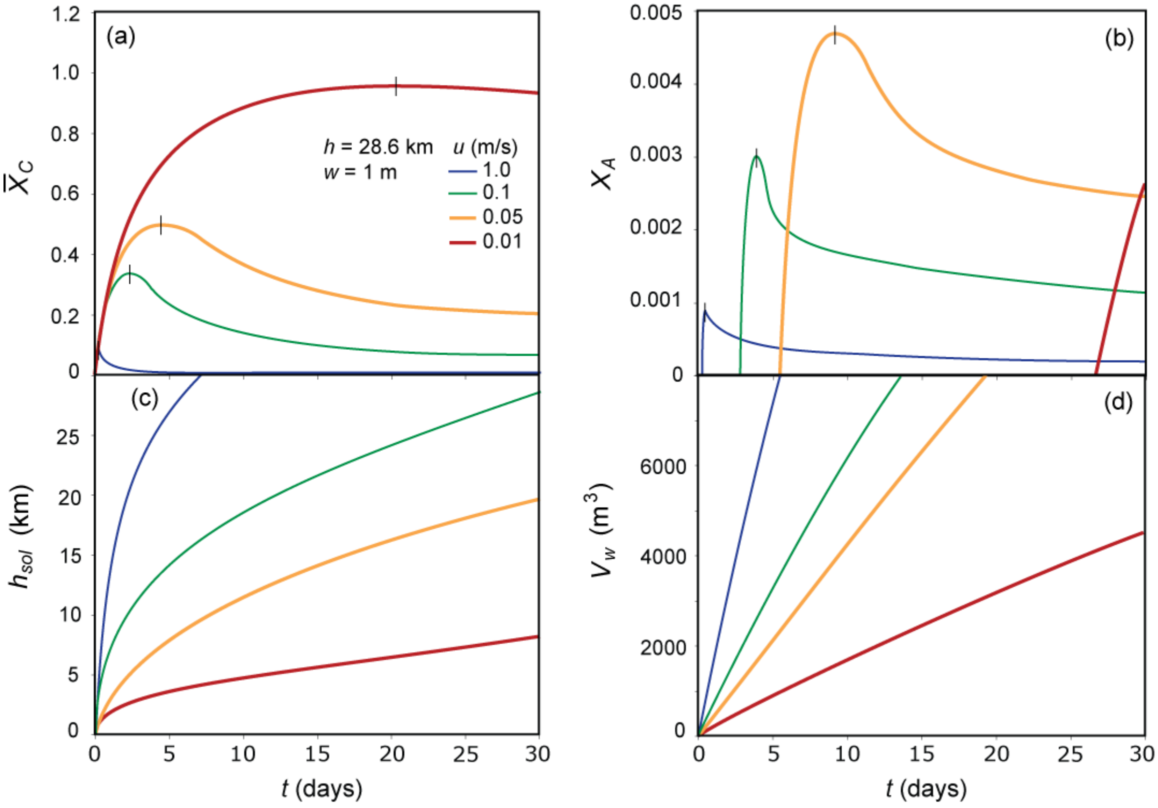

Figure 4.5 Plots of average erupted crystallinity ($\overline{X}_C$), anatectic melt proportion ($X_A = M_A/M_0$), and the height (h) and volume (V_w) of wallrock with $T>T_{sol}$ for various magma velocities.

the depth in the crust where melting occurs, i.e., the region of wallrock above its solidus temperature, gradually migrates higher up in the conduit.

We plot model results for various constant magma velocities in Fig. 4.5. Slower magma velocities result in higher average erupted crystallinities ($\overline{X}_C$), with all model runs showing a maximum crystallinity after the first batch of input magma has had time to traverse the entire conduit height. For initial times $t < h/u$, the solutions are dominated by magma that was heated by the rapid initial conduction and the average crystallinity increases (Fig. 4.5a). At later times ($t > h/u$), model eruptive products increasingly reflect continued heat input to the magma conduit due to flow, and decrease in overall crystallinity for a given constant magma velocity. These later magmas also begin to show the influence of anatectic melting. X_A, the proportion of anatectic melt to primary magma (M_A/M_0), increases rapidly at first and slows as the crystallinity drops and levels off (Fig. 4.5b). The initial time steps of our model are unrealistic and produce transient results. As such, we are not concerned with the high crystallinities present in the initial stage of some of these model runs or whether magma with such high crystallinities is eruptible, but rather are interested in the long-term evolution of the system where $t >> h/u$.

Initial anatectic melt proportions are maximized in runs with higher magma velocities, as higher ascent rates transport heat more efficiently through the system and the surrounding wallrock heats more quickly (Fig. 4.5b). However, high velocity runs reach a peak anatectic melt contribution early, as continued heat input leads to (1) a limit on the amount of anatectic melting as constrained by F, and (2) decreasing extents of crystallization and thus decreasing contributions of latent heat, an important source of heat near the conduit wall. While lower velocity runs do not produce as much wallrock melting initially, they eventually reach higher maximum anatectic melt proportions, as individual packets of magma have more time to interact with the surrounding wallrock and accumulate anatectic melts when the magma rise rate is low.

Some additional model parameters can have important effects on the magnitude of X_A. A narrower conduit width produces both higher average crystallinities and higher X_A since the ratio of input magma to wallrock is lower. Similarly, for a given magma conduit geometry and flow rate, a steeper local geothermal gradient results in a higher X_A. This warmer crustal temperature profile could be either pre-existing (as from a prior eruption or magma intrusion in the area) or created over time by a long sustained eruption. Grain size, which can vary an order of magnitude or more in crustal rocks, also plays an important role in determining how much instantaneous melting can occur, and thus the potential X_A of any particular parcel of magma. Magmas traveling through a finer-grained crust will have potentially higher values of X_A (ignoring possible grain size effects on the efficiency of melt extraction), since gabbroic rocks with a lower average grain size have a greater amount of total surface area to melt.

4.4.1 Application to the Lambahraun lava shield

The region of wallrock partial melting expands upwards along the edge of the conduit as well as outwards into the wallrock over time (Fig. 4.4). As illustrated in Fig. 4.4, the solidus migrates upwards in time such that fresh, unmelted wallrock is progressively involved in the melting process, fulfilling the observational requirement that the wallrock be “refreshed” and therefore remain a source of highly incompatible trace elements (i.e., that they not be significantly stripped out from their source over time). After the solidus reaches the top of the conduit, the region of partial melting still continues to expand outward, continually involving new pristine wallrock. Additionally, melting occurs at very low degrees of partial melting throughout this process (< 5 %), another constraint from geochemical modeling of Lambahraun lava compositions.

Another important feature of Lambahraun's geochemical modeling results is the positive correlation between the extent of crystal fractionation and the proportion of anatectic melt, which both roughly increase over time throughout the eruption. While all model runs with constant melt fluxes exhibit a decrease in average erupted crystallinity (potential extent of fractionation) with time, there are a couple of geologically reasonable conditions that could lead to a positive correlation between differentiation and wallrock melting. Crystallization could occur elsewhere in the system outside of the ascent pathway modeled here, as in a magma storage area. Alternatively, runs with decreasing magma velocities over time can show an increase in erupted crystallinity (as magmas take progressively longer to reach the surface and therefore cool more) while still delivering enough heat to the wallrock to cause a slow but steady increase in X_A.

Under the conditions of our model, some wallrock melting is almost unavoidable for a very wide range of magma ascent rates. However, for higher magma velocities over short time scales, X_A peaks at sufficiently low amounts (< 2 %) that it is unlikely to have any measurable effect on the erupted lava compositions (Fig. 4.6). Very high magma fluxes could result in significant conduit meltback over short timescales, but this process results in a low proportion of crustal melt to the high magma volume ascending through the conduit. For the chemical effects of wallrock interaction to be detectable (i.e., large

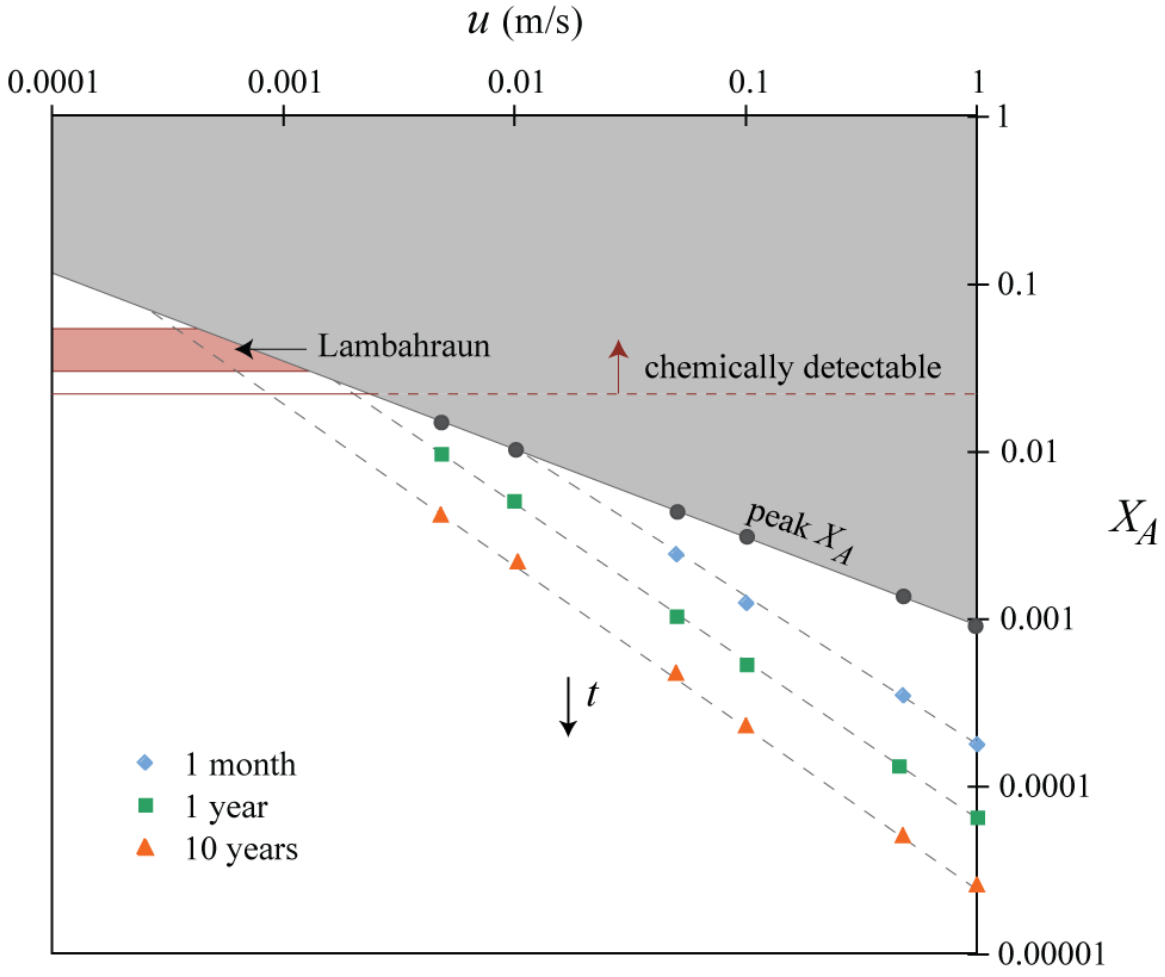

Figure 4.6 Plot of X_A vs. u at different points in time during the systems' evolution. Shaded field is above the maximum X_A values reached for a given velocity and thus not viable under our model. Red field represents the anatectic melt fractions required for Lambahraun according to geochemical modeling in Eason and Sinton (2009); lower red line shows the lower limit at which X_A is great enough for the geochemical effects to be analytically detectable in erupted basalt compositions. Model runs with low magma ascent rates (on the order of 0.1-1 mm/s) can reach significant values of X_A (3-10%) on timescales of years to decades.

X_A), the optimum conditions are long, sustained eruptions of lower velocity magmas, such as is commonly inferred for large Icelandic lava shields, including Lambahraun (Fig. 4.6).

Although we have not run calculations over model timescales equivalent to Lambahraun's eruptive duration due to the inherent computational expense, we can extrapolate to longer timescales based on our current findings. As shown in Fig. 4.6, model runs with low magma ascent rates (on the order of 0.1-1 mm/s) can reach significant values of X_A (3-10%) on timescales of years to decades. Assuming magma flows in a planar conduit with a width of 1 m and a length of 5 km (which is on the order of fissure lengths observed in the WVZ), an average rise rate of 1 mm/s would produce surface lava at a rate of ~ 5 m^3/sec, comparable to low effusion rate pāhoehoe lava (Rowland and Walker, 1990). Given this average eruption rate, it would take approximately 46 years to produce Lambahraun's 7.3 km^3 of basalt.

Magma ascent rates on the order of 0.1-1 mm/s are less than the average Poiseuille flow rate for an open cylindrical conduit like the one modeled here (on the order of 10-1000 mm/s). However, as an idealized case, the Poiseuille flow rate should be considered an upper limit on the magma velocity, and the discrepancy between the modeled values and the Poiseuille flow rate decreases for smaller conduit widths (< 0.5 m diameter). Magma ascent rates on the order of ~ 1 mm/s have been determined by mineralogical and petrological evidence at a variety of locations (e.g., Nakamura, 1995; McCanta et al, 2007; Rutherford, 2008). The predicted ascent rates are also significantly less than the velocities required for fracture propagation in the lithosphere (on the order of 1 m/s) (Heimpel and Olson, 1994). However, as stated previously, this model is not meant to deal with crack propagation issues – magma velocities at the start of the eruption are likely much higher as required for fracturing of the lithosphere. Additionally, the eruption likely starts as a fissure eruption and later collapses down to a single source vent, as observed for other similar, long duration eruptions (Rossi, 1996). This early fissure stage represents a relatively short time period (days to months) compared to the total eruption duration.

One assumption in our model that is likely to play a significant role in controlling how much anatectic melting can occur is the pre-existing geothermal gradient. We have chosen a value of 40°C/km as an average, background-level gradient for the WVZ. However, geothermal gradients as high as 175°C/km (Arnórsson et al., 2008) can exist locally in Iceland. A steeper geothermal profile would lead to more melting as well as an ability to erupt magmas with lower ascent velocities. Even in the absence of a pre-existing high geothermal gradient, a long, sustained eruption like the ones that produce the large volume lava shields eventually create their own locally steep dT/dz. This result raises the possibility that the surface lavas exhibiting the characteristic chemical signature of crustal melting might be relatively late eruptive products of Lambahraun. Much of the volume of the lava shield, the majority of which is inaccessible to sampling, might not exhibit this effect because their eruption preceded thermal conditioning of the crust necessary for melting to occur.

4.4.2 Implications for mid-ocean ridge and ocean island magmatism

Eventually, extended transport of heat into the surrounding host rock should result in the development of a crystal mush, as is commonly inferred for the lower crust at mid-ocean ridges (e.g., Sinton and Detrick, 1992; Coogan et al., 2000; Lissenberg & Dick, 2008). In this case, melt would ascend through a permeable mush of super-solidus material. An environment such as this would lend itself readily to melt-wallrock reactive processes, with increasing potential for anatectic melting as one moves from scenarios with multiple, smaller melt pathways to porous flow. Such reactive processes are outside the scope of the current model, but should lead to even further chemical alteration of the primary magma composition. While the single, planar conduit we have modeled here is likely an oversimplification of complex melt pathways at depths in the lower crust, it illustrates that even in this non-ideal geometry, which limits the surface area of wallrock exposed to magma, the heat transferred by magma to its crustal surroundings can produce sufficient anatectic melting to be discernable in the compositions of basalts erupted over long time-scales.

Low degrees of wallrock partial melting is an important process at a variety of locations, as indicated by the growing evidence from studies of gabbro suites (Larsen, 1979; Elthon, 1987; Meyer et al., 1989; Hansteen, 1991; Elthon et al, 1992; Natland and Dick, 1996; Bédard et al., 2000; Coogan et al., 2000; Dick et al., 2002; Gurenko & Sobolev, 2006) and erupted lavas (Muehlenbachs et al., 1974; Óskarsson et al., 1982; Condomines et al., 1983; Hémond et al., 1988; Nicholson et al., 1991; Maclennan, 2008; Halldórsson et al., 2008; Pietruszka et al., 2009; Eason and Sinton, 2009). One could expect to find a similar crustal assimilation process occurring at other locations with long-lived, sustained eruptions (e.g., as is common in Hawaiian shield volcanoes). Unfortunately, the geochemical signature of this process is difficult to distinguish in major element compositions of erupted lavas because it can be masked by fractionation and/or mixing (Eason and Sinton, 2009).

Variations in incompatible trace element ratios are typically interpreted as being due to mantle melting processes (either variations in extent of partial melting or source composition), which can indeed produce nearly identical effects on trace element compositions in erupted basalts. However, several features of Lambahraun lavas can be used to define criteria for distinguishing among these competing processes. The critical geochemical signature of Lambahraun lavas is the sympathetic enrichment in both CaO and highly incompatible elements coupled with increasing crystal fractionation. The relationship between CaO and incompatible elements is not expected from progressive melting of peridotite source mantle, i.e., with progressive melting of clinopyroxene-bearing peridotite, CaO should increase while incompatible elements decrease. Another clue is the coupling of incompatible element and CaO (over)enrichment with extent of magma differentiation, along with the eruptive history of the volcano, as deduced from field relations and spatial distribution of lava compositions at Lambahraun. Taken together, these relations are inconsistent with progressive recharge of variable mantle-derived magmas (Eason and Sinton, 2009). Thus, the combined use of field, major element and trace element evidence are critical in distinguishing between mantle-derived and crustal interaction processes presented here.

4.5 Summary

We have derived a thermal numerical model in order to examine the consequences of heat exchange between migrating magma and its surrounding wallrock. The extent to which magma crystallizes due to conductive heat loss during low-velocity ascent through melt pathways is dependent on the conduit geometry and magma velocity. In the absence of additional magma chamber fractionation processes, lower velocities and narrower conduits lead to higher average crystallinities in the erupted basalts. Latent heat of crystallization helps drive anatectic melting of the surrounding wallrock.

While high magma ascent rates promote initially rapid crustal melting in our model, primarily owing to our assumed initial conditions, anatectic melting soon reaches a maximum despite continued supply of magma, resulting in a low overall contribution to the erupted magma; such conditions therefore will lead to negligible compositional effects on the erupted basalt composition. Instead, we find that anatectic melting will have a greater effect on the composition of basalts produced during eruptions with relatively low magma ascent velocities but long eruption durations, where the magma (and thus heat) supply is sustained for years to decades. In these latter systems, continued heat exchange between the ascending magma and the surrounding host rock can lead to the incorporation of sufficient proportions (~ 5 %) of low-degree partial melts, with measurable effects on the compositions of erupted lavas on the order of those observed at Lambahraun and other large-volume lava shields in the WVZ. We envision these long-lived, low-effusion rate eruptions as occurring through increasingly reactive, mush-like melt pathways, with eruption rates partly controlled by magma supply rates from the upper mantle.

Melt-wallrock reaction, where present, has important geochemical consequences for the erupted lavas, because it can affect both major and trace element compositions of ascending melts. Depending on the extent of chemical heterogeneity of the crust through which the magma ascends, it potentially could also affect isotopic compositions of erupted lavas. As noted by Eason and Sinton (2009), early evidence of crustal interaction will be virtually undetectable if magmas aggregate and become homogenized in magma reservoirs prior to eruption. In such cases, using the chemical characteristics of MORB to make inferences about mantle melting and source composition could have misleading results.

Acknowledgements

We would like to thank Robert Dunn, Garrett Ito, Julia Hammer and Malin Klawonn for their patient guidance and helpful discussions. This research was supported by National Science Foundation grant OCE05-24922.

CHAPTER 5

CONCLUSIONS

5.1 Summary and broader implications

5.1.1 High-Al N-MORB

The research presented in Chapter 2 of this dissertation has important implications for the melting and crystallization conditions of slow spreading ridges and the ends of ridge segments, where high-Al, low-Si MORB preferentially occur. These are areas where steady-state magma chambers, and the warmer temperature profile they generate in the shallow crust, are unlikely to be present (Sinton and Detrick, 1992; Rubin and Sinton, 2007). Conductive cooling to the surface also has a greater effect on the mantle temperature profile in these regions than at fast-spreading ridges due to slower upwelling. Consequently, melting might stop at significantly deeper levels beneath slow-spreading ridges and fracture zones than at fast-spreading ridges, where the conductive thermal gradient has less of an effect against the adiabat (Bottinga and Allègre, 1978; Reid and Jackson, 1981; Niu and Hékinian, 1997). Conductive cooling in these regions may be more likely to result in high-pressure crystallization, causing clinopyroxene and olivine to fractionate in the upper mantle. These results are consistent with other recent models correlating mantle crystallization with slow spreading mid-ocean ridges and areas of ridge terminations such as fracture zones, overlapping spreading centers and devals (Dmitriev, 1998; Michael and Cornell, 1998; Herzberg, 2004).

Since this study was published, another high-Al sample with similar geochemical characteristics was identified farther east along the GSC at the overlapping spreading center at 93°20’W (Rotella, et al., 2009). In addition, Lissenberg and Dick (2008) proposed that the chemical and mineralogical signatures of this process can be produced by non-equilibrium, near-solidus reactions in the crust, rather than in the upper mantle. Those authors cited textural evidence in oceanic gabbros, but no supporting theory or quantitative modeling.

5.1.2 Eruptive style and crustal interaction in the WVZ

Chapter 3 concludes with some insights into the eruptive behavior of Thjófahraun and Lambahraun, with implications for the more general understanding of basaltic lava shields and fissure eruptions elsewhere in the world. Thjófahraun and other fissure eruptions in Iceland dominantly represent short-lived, high effusion rate eruptions that most likely are fed from existing shallow crustal reservoirs. Mineralogical, compositional, and temporal variations for the Thjófahraun eruption are consistent with progressive cooling and crystallization in a shallow magma chamber. Larger-volume lava shields, mainly erupt dense pāhoehoe lava, at least in the later stages of eruption, suggesting low average effusion rates over a much longer period of time (on the order of decades). Spatial and temporal variations in lava composition for Lambahraun and a few of other large WVZ shields indicate progressive enrichment in incompatible elements in addition to increasing differentiation with time. Whole-rock geochemistry and petrography also indicates plagioclase accumulation played a role in this volcano’s more complex magmatic evolution.

Compositional variations from Lambahraun are inconsistent with simple evolution in a shallow magma chamber, with increasing CaO and incompatible element enrichments greater than predicted by crystal fractionation alone. Based on geochemical modeling, this study concludes that concurrent wallrock assimilation and crystallization during melt migration through the crust can explain the major and trace element correlations for this eruption, with up to 5 % of the total erupted magma derived from low-degree anatectic melts in the later stages of the eruption. We propose that crustal interaction is promoted by low magma ascent rates over long periods, consistent with the evidence for long-lived, low-effusion shield eruptions. If correct, the slow effusion rates that characterize the bulk of these shield eruptions could be related to slow magma ascent through thick crust.

This relationship between slow, sustained magma supply at lava shields and crustal interaction during magma ascent is supported by results from the thermal modeling described in Chapter 4. While high magma ascent rates transfer heat to the wallrock more efficiently and result in more anatectic melting along the conduit initially, the relative contribution of anatectic melt to ascending magma quickly reaches a maximum despite continued supply of heat to the system. These conditions, which approximate higher effusion rate fissure eruptions, do not lead to any measurable geochemical effect on the resulting lavas, as the proportion of anatectic to primary melt is too small to be significant. However, low magma ascent velocities sustained over a long period of time can result in much higher proportions of anatectic melts, up to total contributions of 5 % or more anatectic melt for eruptions lasting decades. In such systems with prolonged heat supply to the crust, magma ascent pathways should increasingly resemble melt-rich crystal mush environments, which are ideal for the kind of concurrent assimilation and crystallization process we see evidence for in Lambahraun.

5.2 Future work

Crustal interaction has important consequences for geochemical interpretations of erupted lavas. Melt-wallrock reaction can affect both major and trace element compositions of ascending melts. This interaction can be particularly cryptic in mid-ocean ridge settings where the composition of the crust and the ascending magma is likely to be very similar. Additionally, aggregation and mixing in shallow magma chambers can further obscure the geochemical evidence for this process. Despite growing literature on the evidence for melt-wallrock interactions in MORB, particularly from studies of lower crustal gabbros, their chemical compositions are often used to infer underlying mantle compositions and melting conditions. Unless crustal interaction for such magmas can be quantified, such inferences could be misleading.

Although the thermal model presented in Chapter 4 indicates the proposed MAFC process is feasible, more work is needed to be able to quantify this effect to better than the order-of-magnitude estimate the current model provides. Ideally, a more robust treatment of the advection-diffusion equation could be combined with a thermodynamic model of the crystallization and assimilation processes to better constrain the energy available for wallrock melting and quantify the resulting magma chemistry. At present, a thermodynamic model that minimizes Gibb’s free energy in calculating crystallization and melting phases and proportions, like MELTS (Ghiorso and Sack, 1995), is too computationally intensive to calculate at every grid node of a 2-d thermal model of a magma conduit. However, incorporation of this kind of thermodynamic constraint would provide a powerful tool for calculating the effect on the resulting erupted products as well as the geochemical consequences for the crustal rocks.

The internal crustal section of mid-ocean ridges remains underrepresented in our current understanding of the overall system. Because of the sampling difficulties, there are still insufficient observations to assess the relative frequency and importance of crustal interaction or make any inferences about systematic characteristics of this process. However, it is apparent that erupted lavas that have by-passed well-mixed crustal reservoir are most likely to preserve evidence for crustal interaction prior to eruption (Rubin et al., 2009). Thus, important information on this process is likely to be gained especially from studies of lavas close to ridge offsets, those from slow and intermediate spreading ridges, and ridges with exceptionally thick crust. More extensive direct sampling of crustal sections also is needed to begin to constrain crustal assimilation, and to provide additional natural data to help understand some of the smaller-scale, disequilibrium processes at work in this system, such as melting and melt extraction rates. Better understanding of processes occurring in the mid- to lower crust beneath mid-ocean ridges will play an important role in future interpretations of MORB geochemistry and resulting inferences about mantle processes.

REFERENCES

Aitcheson, S.J., Forest, A.H., 1994. Quantification of crustal contamination in open magmatic systems. J. Petrol. 35: 461-488.

Allègre, C.J., Minster, J.F., 1978. Quantitative models of trace element behavior in magmatic processes. Earth Planet. Sci. Lett. 38: 1-25.

Allen, R.M., Nolet, G., Morgan, W.J., Vogfjörd, K., Nettles, M., Ekström, G., Bergsson, B.H., Erlendsson, P., Foulger, G.R., Jakobsdóttir, S., Julian, B.R., Pritchard, M., Ragnarsson, S., Stefánsson, R., 2002. Plume-driven plumbing and crustal formation in Iceland. J. Geophys. Res. 107: 10.1029/2001JB000584.

Arnórsson, S., Axelsson, G., Sæmundsson, K., 2008. Geothermal systems in Iceland. Jökull 58: 269-302.

Asimow, P., Ghiorso, M., 1998. Algorithmic modifications extending MELTS to calculate subsolidus phase relations. Amer. Mineral. 83: 1127-1132.

Asimow, P., Dixon, J., Langmuir, C., 2004. A hydrous melting and fractionation model for mid-ocean ridge basalts: Application to the Mid-Atlantic Ridge near the Azores. Geochem. Geophys. Geosyst. 5: 10.1029/2003GC000568.

Asimow, P., Hirschmann, M., Stolper, E., 2001. Calculation of peridotite partial melting from thermodynamic models of minerals and melts, IV. Adiabatic decompression and the composition and mean properties of mid-ocean ridge basalts. J. Petrol. 42: 963-998.

Autio, L., Rhodes, J., 1983. Costa Rica Rift Zone basalts: geochemical and experimental data from a possible example of multistage melting. Initial Reports DSDP 69: 729-745.

Beard, J., Lofgren, G., 1992. An experiment-based model for the petrogenesis of high-alumina basalts. Science 258: 112-115.

Bédard, J.H., Hebert, R., Berclaz, A., Varfalvy, V., 2000. Syntexis and the genesis of lower oceanic crust. In: Y. Dilek, E.M. Moores, D. Elthon, A. Nicolas (Editors), Ophiolites and Oceanic Crust: New Insights from Field Studies and the Ocean Drilling Program. Special Paper, Geol. Soc. Am. 349: 105-119.

Bergmanis, E.C., Sinton, J., Rubin, K.H., 2007. Recent eruptive history and magma reservoir dynamics on the southern East Pacific Rise at 17°30'S. Geochem. Geophys. Geosyst. 8: doi:10.1029/2007GC001742.

Bjarnason, I.T., Menke, W., Flóvenz, Ó.G., 1993. Tomographic image of the mid-Atlantic plate boundary in southwest Iceland. J. Geophys. Res. 98: 6607-6622.

Björnsson, A., 1985. Dynamics of crustal rifting in NE Iceland. J. Geophys. Res. 90: 10151-10162.

Blake, S., 1981. Volcanism and the dynamics of open magma chambers. Nature 289: 783-785.

Bostrom, R., 1971. Westward displacement of the lithosphere. Nature 234: 356-538.

Bottinga, Y., Allègre, C., 1978. Partial melting under spreading ridges. Phil. Trans. R. Soc. Lond. 288: 501-525.

Bowen, N.L., 1922a. The reaction principle in petrogenesis. J. Geology 30: 177-198.

Bowen, N.L., 1922b. The behavior of inclusions in igneous magmas. J. Geology 30: 513-570.

Bowen, N.L., 1928. The Evolution of the Igneous Rocks. Princeton, NJ: Princeton University Press, 334 pp.

Bruce, P.M., Huppert, H.E., 1990. Solidification and melting along dykes by the laminar flow of basaltic magma. In: M.P. Ryan (Editor), Magma Transport and Storage. John Wiley & Sons Inc, West Sussex, England, pp. 87-101.

Buck, W.R., Einarsson, P., Brandsdóttir, B., 2006. Tectonic stress and magma chamber size as controls on dike propagation: Constraints from the 1975-1984 Krafla rifting episode. J. Geophys. Res. 111: doi:10.1029/2005JB003879.

Canales, J., Ito, G., Detrick, R., Sinton, J., 2002. Crustal thickness along the Galápagos Spreading Center and the compensation of the Galápagos hotspot swell. Earth Planet. Sci. Lett. 203: 311-327.

Chappell, B., 1992. Trace element analysis of rocks by X-ray spectrometry. Adv. X-ray Anal. 34: 263-276.

Condomines, M.K., Grönvold, K., Hooker, P.J., Muehlenbachs, K., O'Nions, R.K., Óskarsson, N., Oxburgh, E.R., 1983. He, O, Sr and Nd isotope relationships in Icelandic volcanics. Earth Planet Sci. Lett. 66: 125-136.

Coogan, L.A., Saunders, A.D., Kempton, P.D., Norry, M.J., 2000. Evidence from oceanic gabbros for porous melt migration within a crystal mush beneath the Mid-Atlantic Ridge. Geochem. Geophys. Geosyst. 1: doi:10.1029/2000GC000072.

Cushman, B., Sinton, J., Ito, G., Dixon, J., 2004. Glass compositions, plume-ridge interaction, and hydrous melting along the Galápagos Spreading Center, 90.5°W to 98°W. Geochem. Geophys. Geosyst. 5: 10.1029/2004GC000709.

Danyushevsky, L., Perfit, M., Eggins, S., Falloon, T., 2003. Crustal origin for coupled ‘ultra-depleted’ and ‘plagioclase’ signatures in MORB olivine-hosted melt inclusions: evidence from the Siqueiros Transform Fault, East Pacific Rise. Contrib. Mineral. Petrol. 144: 619-637.

Delaney, P.T., Pollard, D.D., 1982. Solidification of basaltic magma during flow in a dike. Am. J. Sci. 282: 856-885.

DeMets, C., Gordon, R., Argus, D., Stein, S., 1994. Effect of recent revisions to the geomagnetic time reversal scale on estimates of current plate motions. Geophys. Res. Lett. 21: 2191-2194.

DePaolo, D.J., 1981. Trace element and isotopic effects of combined wallrock assimilation and fractional crystallization. Earth Planet. Sci. Lett. 53: 189-202.

Detrick, R., Sinton, J., Ito, G., Canales, J., Behn, G., Blacic, T., Cushman, B., Dixon, J., Graham, D., Mahoney, J., 2002. Correlated geophysical, geochemical and volcanological manifestations of plume-ridge interaction along the Galápagos Spreading Center. Geophys. Geochem. Geosyst. 3: 10.1029/2002GC000350.

Dick, H.J.B., Meyer, P.S., Bloomer, S., Kirby, S., Stakes, D., Mawer, C., 1991. Lithostratigraphic evolution of an in-situ section of oceanic layer 3. In Von Herzen, R.P., Robinson, P.T., et al., Proc. ODP, Sci. Results, 118: College Station, TX (Ocean Drilling Program), 439-540.

Dick, H.J.B., Ozawa, K., Meyer, P.S., Niu, Y., Robinson, P.T., Constantin, M., Hebert, R., Maeda, J., Natland, J.H., Hirth, G., Mackie, S., 2002. Primary silicate mineral chemistry of a 1.5-km section of very slow spreading lower ocean crust: ODP Hole 735B, Southwest Indian Ridge. In: J.H. Natland, H.J.B. Dick, D.J. Miler, R. Von Herzen (Editors), Proceedings of the Ocean Drilling Program. Sci. Results, 176. Ocean Drilling Program, College Station, TX, pp. 1-60.

Dmitriev, L., 1998. Chemical variability of mid-ocean ridge basalts as a function of the geodynamic setting of their formation. Petrology 6: 314-334.

Doglioni, C., Carminati, E., Bonatti, E., 2003. Rift asymmetry and continental uplift, Tectonics 22: 10.1029/2002TC001459.

Dungan, M., Rhodes, J., 1978. Residual glasses and melt inclusions in basalts from DSDP Legs 45 and 46: evidence for magma mixing. Contrib. Mineral. Petrol. 67: 417-431.

Dunn, T., Sen, C., 1994. Mineral/matrix partition coefficients for orthopyroxene, plagioclase, and olivine in basaltic to andesitic systems: a combined analytical and experimental study. Geochim. Cosmochim. Acta. 58: 717-734.

Eason, D., Sinton, J., 2006. Origin of high-Al N-MORB by fractional crystallization in the upper mantle beneath the Galápagos Spreading Center. Earth and Planet. Sci. Lett. 252: 423-436.

Eason, D., Sinton, J., 2009. Lava shields and fissure eruptions in the Western Volcanic Zone, Iceland: evidence for magma chambers and crustal interaction. J. Volc. Geotherm. Res. 186: 331-348.

Edwards, B.R., Russell, J.K., 1998. Time scale of magmatic processes: new insights from dynamic models for magmatic assimilation. Geology 26: 1103-1106.

Elthon, D., 1987. Petrology of gabbroic rocks from the mid-Cayman rise spreading center. J. Geophys. Res. 92: 658-682.

Elthon, D., Casey, J., Komor, S., 1982. Mantle chemistry of ultramafic cumulates from the North Arm Mountain Massif of the Bay of Islands ophiolite: Evidence for high-pressure crystal fractionation of oceanic basalts. J. Geophys. Res. 87: 8717-8734.

Elthon, D., Ross, D., Meen, J., 1995. Compositional variations of basaltic glasses from the Mid-Cayman Rise spreading center. J. Geophys. Res. 100: 12497-12512.

Embley, R.W., Chadwick, Jr., W.W., Perfit, M.R., Smith, M.C., Delaney, J.R., 2000. Recent eruptions on the CoAxial segment of the Juan de Fuca Ridge: Implications for mid-ocean ridge accretion processes. J. Geophys. Res. 105: 16501-16526.

Fisk, M., Bence, A., Schilling, J.-G., 1982. Major element chemistry of Galápagos rift zone magmas and their phenocrysts. Earth Planet. Sci. Lett. 61: 171-189.

Flower, M., 1980. Accumulation of calcic plagioclase in ocean ridge tholeiite: an indication of spreading rate? Nature 287: 530-532.

Francis, D., 1980. The pyroxene paradox in MORB glasses – a signature of picritic parental magmas? Nature 319: 586-588.

Ghiorso, M., Sack, R., 1995. Chemical mass-transfer in magmatic processes IV. A revised and internally consistent thermodynamic model for the interpolation and extrapolation of liquid-solid equilibria in magmatic systems at elevated temperatures and pressures. Contrib. Mineral. Petrol. 199: 197-212.

Ghiorso, M., Hirschmann, M., Reiners, P., Kress, V., 2002. The pMELTS: a revision of MELTS for improved calculation of phase relations and major element partitioning related to partial melting of the mantle to 3 GPa. Geochem. Geophys. Geosyst. 3: 10.1029/2001GC000217.

Green, T.H., 1994. Experimental studies of trace-element partitioning applicable to igneous petrogenesis: Sedona 16 years later. Chem. Geol. 117: 1-36.

Grove, T.L., Kinzler, R.J., 1986. Petrogenesis of andesites. Ann. Rev. Earth Planet. Sci. 14: 417-454.

Grove, T., Kinzler, R., Bryan, W., 1992. Fractionation of mid-ocean ridge basalts. In: Mantle Flow and Melt Generation at Mid-Ocean Ridges, J. Phipps-Morgan, D. Blackman, J. Sinton (Editors), Geophys. Monogr. Ser. 71, pp. 281-310, AGU, Washington, DC.

Gurenko, A.A., Sobolev, A.V., 2006. Crust-primitive magma interaction beneath neovolcanic rift zone of Iceland recorded in gabbro xenoliths from Midfell, SW Iceland. Contrib. Mineral. Petrol. 151: doi:10.1007/S0041000600792.

Halldórsson, S.A., Óskarsson, N., Grönvold, K., Sigurdsson, G., Sverrisdóttir, G., Steinthorsson, S., 2008a. Isotopic-heterogeneity of the Thjorsa lava – Implications for mantle sources and crustal processes within the Eastern Rift Zone, Iceland. Chemical Geology 255: doi:10.1016/j.geochem.2008.06.050.

Halldórsson, S.A., Sinton, J., Grönvold, K., Sigurdsson, G., Sverrisdóttir, G., 2008b. Isotopic variations in postglacial volcanic products of the Western Rift Zone, Iceland. IAVCEI 2008 General Assembly, Reykjavík, Iceland: Abstract 1-b-P11.

Hansteen, T.H., 1991. Multi-stage evolution of the picritic Maelifell rocks, SW Iceland: constraints from mineralogy and inclusions of glass and fluid in olivine. Contrib. Mineral. Petrol. 109: 225-239.

Head III, J.W., Wilson, L., Smith, D.K., 1996. Mid-ocean ridge eruptive vent morphology and substructure: Evidence for dike widths, eruption rates, and evolution of eruptions and axial volcanic ridges. J. Geophys. Res. 101: 28265-28280.

Heimpel, M., Olson, P., 1994. Buoyancy-driven dike propagation through the lithosphere: Models and experiments. In: M.P. Ryan (editor), Magmatic Systems, Academic Press, 223-240.

Hémond, C., Condomines, M., Fourcade, S., Allègre, C.J., Óskarsson, N., Javoy, M., 1988. Th, Sr and O isotopic geochemistry in recent tholeiites from Iceland: crustal influence on mantle derived magmas. Earth Planet. Sci. Lett. 87: 273-285.

Hémond, C., Arndt, N.T., Lichtenstein, U., Hofmann, A.W., Óskarsson, N., Steinthorsson, S., 1993. The heterogeneous Iceland plume—Nd-S-O isotopes and trace-element constraints. J. Geophys. Res. 98: 15833-15850.

Herzberg, C., 2004. Partial crystallization of mid-ocean ridge basalts in the crust and mantle. J. Petrol. 45: 2389-2405.

Hey, R., Sinton, J., Kleinrock, M., Yonover, R., Macdonald, K., Miller, S., Searle, R., Christie, D., Atwater, T., Sleep, N., Johnson, H., Neal, C., 1992. ALVIN Investigation of an active propagating rift system, Galápagos 95.5°W. Mar. Geophys. Res. 14: 207-226.

Hirschmann, M., Ghiorso, M., Wasylenki, L., Asimow, P., Stolper, E., 1998. Calculation of peridotite partial melting from thermodynamic models of minerals and melts. I. Review of methods and comparison to experiments. J. Petrol. 39: 1091-1115.

Hirschmann, M., Asimow, P., Ghiorso, M., Stolper, E., 1999. Calculation of peridotite partial melting from thermodynamical models of minerals and melts. III. Controls on isobaric melt production and the effect of water on melt production. J. Petrol. 40: 831-851.

Howarth, R.J., 1998. Improved estimators of uncertainty in proportions, point-counting, and pass-fail test results. Am. Journal Sci. 298: 594-607.

Hunter, R.H., 1996. Texture development in cumulate rocks. In: R.G. Cawthorn (editor), Layered Intrusions, 77-101, Elsevier, New York.

Huppert, H.E., Sparks, R.S.J., 1989. Chilled margins in igneous rocks. Earth Planet Sci. Lett. 92: 397-405.

Jaques, A., Green, D., 1979. Determination of liquid compositions in high-pressure melting of peridotite. Amer. Mineral. 64: 1312-1321.

Jones, J.H., 1995. Experimental trace element partitioning. In: T.J. Ahrens (editor), Rock Physics and Phase Relations: a Handbook of Physical Constants, AGU Reference Shelf 3, 73-104. Washington: AGU.

Keleman, P.B., 1990. Reaction between ultramafic rock and fractionating basaltic magma I. Phase relations, the origin of calc-alkaline magma series, and the formation of discordant dunite. J. Petrol. 31: 51-98.

Kelemen, P., Shimizu, N., Salters, V., 1995. Extraction of mid-ocean-ridge basalt from the upwelling mantle by focused flow of melt in dunite channels. Nature 375: 747-753.

Keleman, P.B., Yogodzinski, G.M., Scholl, D.W., 2003. Along-strike variation in the Aleutian Island Arc: genesis of high Mg# andesite and implications for continental crust. In: J. Eiler (editor), Inside the Subduction Factory, AGU Monograph 138, 223-246. Washington: AGU.

Kelemen, P., Hirth, G., Shimizu, N., Spiegelman, M., Dick, H., 1997. A review of melt migration processes in the adiabatically upwelling mantle beneath oceanic spreading ridges. Phil. Trans. Royal. Soc. Lond. 355: 283-318.

Kinzler, R., Grove, T., 1992. Primary magmas of mid-ocean ridge basalts, 2. Applications. J. Geophys. Res. 97: 6907-6926.

Klein, E., Langmuir, C., 1987. Global correlations of ocean ridge basalt chemistry with axial depth and crustal thickness. J. Geophys. Res. 92: 8089-8115.

Kvassnes, A., 2004. The Evolution of Oceanic Gabbros: In-situ and Ancient Examples, Ph.D. Thesis, MIT, Woods Hole Joint Program in Oceanography.

Kvassnes, A., Dick, H.J., 2000. Deviations from dry fractionation trends in gabbros from Atlantis Bank, South West Indian Ocean. EOS. Trans. Amer. Geophys. Union 82.

Kvassnes, A., Grove, T.L., 2008. How partial melts of mafic lower crust affect ascending magmas at oceanic ridges. Contrib. Min. Pet. 156: 49-71.

LaFemina, P.C., Dixon, T.H., Malservisi, R., Arnadottir, T., Sturkell, E., Sigmundsson, F., Einarsson, P., 2005. Geodetic GPS measurements in south Iceland: Strain accumulation and partitioning in a propagating ridge system. J. Geophys. Res. 110: doi:10.1029/2005JB003675.

Larsen, J.G., 1979. Glass-bearing gabbro inclusions in hyaloclastites from Tindfjalljokull, Iceland. Lithos 12: 289-302.

Lehnert, K., Su, Y., Langmuir, C., Sarbas, B., Nohl, U., 2000. A global geochemical database structure for rocks. Geochem. Geophys. Geosyst. 1: 1999GC000026.

Lissenberg, C.J., Dick, H.J.B., 2008. Melt-rock reaction in the lower oceanic crust and its implications for the genesis of mid-ocean ridge basalt. Earth Planet. Sci. Lett. 271: 311-325.

Lister, J.R., 1990. Buoyancy-driven fluid fracture: the effects of material toughness and of low-viscosity precursors. J. Fluid Mech. 210: 263-280.

Maclennan, J., 2008a. Concurrent mixing and cooling of melts under Iceland. J. Petrol. 49:1931-1953.

Maclennan, J., 2008b. Lead isotope variability in olivine-hosted melt inclusions from Iceland. Geochim. Cosmochim. Acta 72: 4159-4176.

Maclennan, J., McKenzie, D., Grönvold, K., Slater, L., 2001. Crustal accretion under northern Iceland. Earth Planet. Sci. Lett. 191: 295-310.

Maclennan, J., McKenzie, D., Grönvold, K., Shimizu, N., Eiler, J.M., Kitchen, N., 2003a. Melt mixing and crystallization under Theistareykir, northeast Iceland. Geochem. Geophys. Geosyst. 4: doi:10.1029/2003GC000558.

Maclennan, J., McKenzie, D., Hilton, F., Grönvold, K., Shimizu, N., 2003b. Geochemical variability in a single flow from northern Iceland, J. Geophys. Res. Lett. 108: doi:10.1029/2000JB000142.

MacLeod, C.J., Yaouancq, G., 2000. A fossil melt lens in the Oman Ophiolite: implications for magma chamber processes at fast spreading ridges. Earth Planet. Sci. Lett. 176: 357-373.

Marsh, B.D., 1995. Solidification fronts and magmatic evolution. Mineral Mag. 60: 5-40.

Marsh, B.D., 1998. On the interpretation of crystal size distribution in magmatic systems. J. Petrol. 39: 553-599.

McCanta, M.C., Rutherford, M.J., Hammer, J.E., 2007. Pre-eruptive and syn-eruptive conditions in the Black Butte California dacite: Insight into crystallization kinetics in a silicic magma system. J. Volcanol. Geotherm. Res. 160: 263-284.

McKenzie, D., O'Nions, R., 1991. Partial melt distributions from inversion of rare-earth element concentrations. J. Petrol. 32: 1021-1091.

McKenzie, D., O'Nions, R., 1995. The source regions of ocean island basalts. J. Petrol. 36: 133-159.

Metrich, N., Sigurdsson, H., Meyer, P.S., Devine, J.D., 1991. The 1783 Lakagigar eruption in Iceland: geochemistry, CO_2 and sulfur degassing. Contrib. Mineral. Petrol. 107: 435-447.

Meurer, W., Sturm, M., Klein, E., Karson, J., 2001. Basalt compositions from the Mid-Atlantic Ridge at the SMARK area (22°30'N to 22°50'N): implications for parental liquid variability at isotopically homogeneous spreading centers. Earth Planet. Sci. Lett. 186: 451-469.

Meyer, P.S., Dick, H.J.B., Thompson, G., 1989. Cumulate gabbros from the Southwest Indian Ridge, 54ºS-7º16'E: implications for magmatic processes at a slow spreading ridge. Contrib. Mineral. Petrol. 103: 44-63.

Michael, P., Cornell, W., 1998. Influence of spreading rate and magma supply on crystallization and assimilation beneath mid-ocean ridges: evidence from chlorine and major element chemistry of mid-ocean ridge basalts. J. Geophys. Res. 103: 18325-18356.

Muehlenbachs, K., Anderson, A.T., Sigvaldason, G.E., 1974. Low-^{18}O basalts from Iceland. Geochim. Cosmochim. Acta 38: 577-588.

Nakamura, M., 1995. Continuous mixing of crystal mush and replenished magma in the ongoing Unzen eruption. Geology 23: 807-810.

Natland, J.H., Dick, H.J.B., 1996. Melt migration through high-level gabbroic cumulates of the East Pacific Rise at Hess Deep: the origin of magma lenses and the deep crustal structure of fast-spreading ridges. In: C. Mevel, K.M. Gillis, J.F. Allan, P.S. Meyer (Editors), Proceedings of the Ocean Drilling Program. Sci. Results, 147, Ocean Drilling Program. College Station, TX, pp. 21-58.

Nichols, A.R.L., Carroll, M.R., Höskuldsson, Á., 2002. Is the Iceland hot spot also wet? Evidence from the water contents of undegassed submarine and subglacial pillow basalts. Earth Planet. Sci. Lett. 202: 77-87.

Nicholson, H., Condomines, M., Fitton, J.G., Fallick, A.E., Grönvold, K., Rogers, G., 1991. Geochemical and isotopic evidence for crustal assimilation beneath Krafla, Iceland. J. Petrol. 32: 1005-1020.

Nielsen, R., Crum, J., Bourgeois, R., Hascall, K., Fisk, L., Christie, D., 1995. Melt inclusions in high-An plagioclase from the Gorda Ridge: an example of the local diversity of MORB parent magmas. Contr. Mineral. Petrol. 122: 34-50.

Niu, Y., 1997. Mantle melting and melt extraction processes beneath ocean ridges: evidence from abyssal peridotites. J. Petrol. 38: 1047-1074.

Niu, Y., Batiza, R., 1991. An empirical method for calculating melt compositions produced beneath mid-ocean ridges: application for axis and off-axis (seamounts) melting. J. Geophys. Res. 96: 21753-21777.

Niu, Y., Hékinian, R., 1997. Spreading rate dependence of the extent of mantle melting beneath ocean ridges. Nature 385: 326-329.

Norrish, K., Hutton, J., 1977. An accurate X-ray spectrographic method for the analysis of a wide range of geological samples. Geochim. Cosmochim. Acta 33: 431-441.

O'Hara, M.J., 1995. Trace element geochemical effects of integrated melt extraction and shaped melting regimes. J. Petrol. 34: 1111-1132.

O'Hara, M.J., 1998. Volcanic plumbing and the space problem – thermal and geochemical consequences of large-scale assimilation in ocean island development. J. Petrol. 39: 1077-1089.

Óskarsson, N., Sigvaldason, G.E., Steinthorsson, S., 1982. A dynamic model of the rift zone petrogenesis and the regional petrology of Iceland. J. Petrol. 23: 28-74.

Panjasawatwong, Y., Danyushevsky, L., Crawford, A., Harris, K., 1995. An experimental study of the effects of melt composition on plagioclase-melt equilibria at 5 and 10 kbar: Implications for the origin of magmatic high-An plagioclase. Contr. Mineral. Petrol. 118: 420-432.

Parfitt, E.A., Head III, J.W., 1993. Buffered and unbuffered dike emplacement on Earth and Venus: implications for magma reservoir size, depth, and rate of magma replenishment. Earth, Moon, Planets 61: 249-281.

Perfit, M.R., Chadwick, Jr., W.W., 1998. Magmatism at mid-ocean ridges: constraints from volcanological and geochemical investigations. In: W.R. Buck, P.T. Delaney, J.A. Karson, Y. Lagabrielle (Editors), Faulting and Magmatism at Mid-Ocean Ridges, Amer. Geophy. Union Monogr., 106, pp. 59-115.

Philpotts, A.R., Asher, P.M., 1993. Wallrock melting and reaction effects along the Higganum diabase dike in Connecticut: contamination of a continental flood basalt feeder. J. Petrol. 34: 1029-1058.

Philpotts, A.R., Dickinson, L.D., 2000. The formation of plagioclase chains during convective transfer in basaltic magma. Nature 406(6791): 59-61.

Pietruszka, A.J., Hauri, E.H., Blichert-Toft, J., 2009. Crustal contamination of mantle-derived magmas within Piton de la Fournaise volcano, Reunion Island. J. Petrol. 50: 661-684.

Reid, I., Jackson, H., 1981. Oceanic spreading rate and crustal thickness. Mar. Geophys. Res. 5: 165-172.

Reiners, P.W., Nelson, B.K., Ghiorso, M.S., 1995. Assimilation of felsic crust by basaltic magma: thermal limits and extents of crustal contamination of mantle-derived magmas. Geology 23: 563-566.

Ricard, R., Doglioni, C., Sabadini, R., 1991. Differential rotation between lithosphere and mantle: A consequence of lateral viscosity variations. J. Geophys. Res. 96: 8407-8415.

Roeder, P.L., Emslie, R.F., 1970. Olivine-liquid equilibrium. Contrib. Min. Petrol. 29: 275-289.

Rossi, M.J., 1996. Morphology and mechanism of eruption of postglacial shield volcanoes in Iceland. Bull. Volcanol. 57: 530-540.

Rotella, M., Sinton, J., Mahoney, J., Chazey, W., 2009. Geochemical evidence for low magma supply and inactive propagation of the Galápagos 93.25°W overlapping spreading center. Geochem. Geophys. Geosys., in press.

Rowland, S.K., Walker, G.P.L., 1990. Pahoehoe and aa in Hawaii: Volumetric flow rate controls the lava structure. Bull. Volcanol. 52: 615-628.

Rubin, K.H., Sinton, J.M., 2007. Inferences on mid-ocean ridge thermal and magmatic structure from MORB compositions. Earth Planet. Sci. Lett. 260: 257-276.

Rubin, K.H., Sinton, J.M., Maclennan, J., Hellebrand, E., 2009. Magmatic filtering of mantle compositions at mid-ocean-ridge volcanoes. Nature Geosci. 2: doi:10.1038/NGEO504.

Rutherford, M.J., 2008. Magma ascent rates. Rev. Min. Geochem. 69: 241-271.

Sæmundsson, K., 1991. Geology of the Krafla system. In: A. Gardarsson, A. Einarsson (Editors), Nattura Myvatns, Hid Islenska Natturufraedifelag, Reykjavik, pp. 25-95 (in Icelandic).

Sæmundsson, K., 1992. Geology of the Thingvallavatn area. Oikos 64: 40-68.

Salters, V., Stracke, A., 2004. Composition of the depleted mantle. Geochem. Geophys. Geosyst. 5: doi:10.1029/2003GC000597.

Schilling, J.-G., Kingsley, R., Devine, J., 1982. Galápagos hot-spot spreading center system I. Spatial petrological and geochemical variations (83°W-101°W). J. Geophys. Res. 87: 5593-5610.

Schilling, J.-G., Zajac, M., Evans, R., Johnston, T., White, W., Devine, J.O., Kingsley, R., 1983. Petrologic and geochemical variations along the Mid-Atlantic Ridge from 29ºN to 73ºN. Am. J. Sci. 283: 510-586.

Shaw, D.M., 1970. Trace element fractionation during anatexis. Geochim. Cosmochim. Acta 34: 237-243.

Shen, Y., Forsyth, D., 1995. Geochemical constraints on initial and final depth of melting beneath mid-ocean ridges. J. Geophys. Res. 100: 2211-2237.

Sigurdsson, H., 1987. Dyke injection in Iceland: A review. In: H.C. Halls and W.F. Fahrig (Editors), Mafic Dyke Swarms, Geol. Assoc. Can. Spec. Pap. 34: 55-64.

Sinton, J., 1978. Equilibration history of the basal Alpine-type peridotite, Red Mountain, New Zealand. Ofioliti 3: 224.

Sinton, J., Detrick, R., 1992. Mid-ocean ridge magma chambers. J. Geophys. Res. 97: 197-216.

Sinton, J., Grönvold, K., Sæmundsson, K., 2005. Postglacial eruptive history of the Western Volcanic Zone, Iceland. Geochem. Geophys. Geosyst. 6: doi:10.1029/2005GC001021.

Sinton, J., Smaglik, S., Mahoney, J., Macdonald, K., 1991. Magmatic processes at superfast spreading mid-ocean ridges: glass compositional variations along the East Pacific Rise, 13°-23°. J. Geophys. Res. 96: 6133-6155.

Sinton, J., Detrick, R., Canales, J., Ito, G., Behn, M., 2003. Morphology and segmentation of the western Galápagos Spreading Center, 90.5°-98°W: Plume-ridge interaction at an intermediate spreading ridge. Geochem. Geophys. Geosyst. 4: 10.1029/2003GC000609.

Sinton, J.M., Bergmanis, E., Rubin, K., Batiza, R., Gregg, T.K.P., Grönvold, K., Macdonald K., White, S., 2002. Volcanic eruptions on mid-ocean ridges: New evidence from the superfast-spreading East Pacific Rise, 17°-19° S. J. Geophys. Res. 107: doi:10.1029/2000JB000090.

Sisson, T., Grove, T., 1993. Experimental investigation of the role of H_2O in calc-alkaline differentiation and subduction zone magmatism. Contrib. Mineral. Petrol. 113: 143-166.

Smith, P., Asimow, P., 2005. Adiabat_1ph: a new public front-end to the MELTS, pMELTS, and pHMELTS models. Geochem. Geophys. Geosyst. 6: doi:10.1029/2004GC000816.

Sobolev, A., Danyushevsky, L., Dmitriev, L., Suschevskaya, N., 1989. High-alumina magnesian tholeiite as the primary basalt magma at Midocean ridge. Geochem. Int. 26: 128-133.

Spera, F., Bohrson, W., 2001. Energy-constrained open-system magmatic processes I: General model and energy-constrained assimilation and fractional crystallization (EC-AFC) formulation. J. Petrol. 42: 999-1018.

Spence, D.A., Sharp, P., 1985. Self-similar solutions for elastohydrodynamic cavity flow. Proc. R. Soc. London, Ser. A 400: 289-313.

Stakes, D., Shervais, J., Hopson, C., 1984. The volcanic-tectonic cycle of the FAMOUS and AMAR valleys, Mid-Atlantic Ridge (36°47'N): Evidence from basalt glass and phenocryst compositional variations for a steady state magma chamber beneath valley midsections, AMAR 3. J. Geophys. Res. 89: 6995-7028.

Stewart, M.A., Karson, J.A., Klein, E.M., 2005. Four-dimensional upper crustal construction at fast-spreading mid-ocean ridges: A perspective from an upper crustal cross-section at the Hess Deep Rift. J. Volcanol. Geotherm. Res. 144: 287-309.

Stracke, A., Zindler, A., Salters, V.J.M., McKenzie, D., Blichert-Toft, J., Albarède, F., Grönvold, K., 2003. Theistareykir revisited. Geochem. Geophys. Geosyst. 4: doi:10.1029/2001GC000201.

Sun, S.S., McDonough, W.F., 1989. Chemical and isotopic systematics of ocean island basalts: Implications for mantle composition and processes. In: A.D. Saunders, M.J. Norry (Editors), Magmatism in the Ocean Basins, Geol. Soc. Spec. Publ. 42: 313-345.

Taylor, H.P., Jr, 1980. The effects of assimilation of country rocks by magmas on $^{18}O/^{16}O$ and $^{87}Sr/^{86}Sr$ systematics in igneous rocks. Earth Planet. Sci. Lett. 47: 243-254.

Taylor, H.P., Jr., Giannetti B., Turi, B., 1979. Oxygen isotope geochemistry of the potassic igneous rocks from the Roccamonfina volcano, Roman comagmatic province, Italy. Earth Planet. Sci. Lett. 46: 81-106.

Thirlwall, M.F., Gee, M.A.M., Taylor, R.N., Murton, B.J., 2004. Mantle components in Iceland and adjacent ridges investigated using double-spike Pb isotope ratios. Geochim. Cosmochim. Acta 68: 361-386.

Thompson, G., Bryan, W., Melson, W., 1980. Geological and geophysical investigations of the mid-Cayman rise spreading center: geochemical variation and petrogenesis of basalt glasses. J. Geology 88: 41-55.

Tormey, D., Grove, T., Bryan, W., 1987. Experimental petrology of normal MORB near the Kane Fracture Zone: 22°-25°N, Mid-Atlantic Ridge. Contrib. Mineral. Petrol. 96: 121-139.

Tryggvason, E., 1984. Widening of the Krafla fissure swarm during the 1975-1981 volcano-tectonic episode. Bull. Volcanol. 47: 47-69.

Tryggvason, E., 1986. Multiple magma reservoirs in a rift zone volcano: Ground deformation and magma transport during the September eruption of Krafla, Iceland. J. Volcanol. Geotherm. Res. 28: 1-44.

Verma, S., Schilling, J.-G, 1982. Galápagos hot spot-spreading center system 2. ^{87}Sr/^{86}Sr and large ion lithophile element variations (85°W-101°W). J. Geophys. Res. 87: 10838-10856.

Verma, S., Schilling, J.-G., Waggoner, D., 1983. Neodymium isotopic evidence for Galápagos hotspot-spreading centre system evolution. Nature 306: 654-657.

White, R., Minshull, T., Bickle, M., Robinson, C., 2001. Melt generation at very slow-spreading oceanic ridges: constraints from geochemical and geophysical data. J. Petrol. 42: 1171-1196.

Workman, R., Hart, S., 2005. Major and trace element composition of the depleted MORB mantle (DMM). Earth Planet. Sci. Lett. 231: 53-72.

Zindler, A., Hart, S.R., Frey, F.A., Jakobsson, S.P., 1979. Nd and Sr isotope ratios and Rare Earth Element abundances in Reykjanes Peninsula basalts: Evidence for mantle heterogeneity beneath Iceland. Earth Planet. Sci. Lett. 45: 249-262.